Upper–Level Waves of Synoptic Scale at Midlatitudes

by

Chantal Rivest

B.Sc., Physique, Université de Montréal (1983)

M.Sc., Meteorology, McGill University (1985)

Submitted to the Department of Earth, Atmospheric, and Planetary Sciences
in partial fulfillment of the requirements for the degree of

Doctor of Philosophy in Meteorology

at the

Massachusetts Institute of Technology

September 1990

Signature of Author _____

Center for Meteorology and Physical Oceanography
Department of Earth, Atmospheric and Planetary Sciences
August 10, 1990

Certified by _____

Kerry A. Emanuel
Professor of Meteorology
Thesis Supervisor

Certified by _____

Brian F. Farrell
Associate Professor of Dynamic Meteorology
Thesis Supervisor

Accepted by _____

Thomas H. Jordan
Chairman, Departmental Committee on Graduate Students

Upper–Level Waves of Synoptic Scale at Midlatitudes

by

Chantal Rivest

Submitted to the Department of Earth, Atmospheric, and Planetary Sciences on August 22, 1990 in partial fulfillment of the requirements for the degree of Doctor of Philosophy in Meteorology

Abstract

Upper–level waves of synoptic scale are important dynamical entities at midlatitudes. They often induce surface cyclogenesis (cf. Peterssen and Smebye, 1971), and their life duration is typically longer than time scales for disruption by the ambient shear (Sanders, 1988). The objectives of the present thesis are to explain the maintenance and genesis of upper–level synoptic–scale waves in the midlatitude flow.

We develop an analytical model of waves on generalized Eady basic states that have uniform tropospheric and stratospheric potential vorticity, but allow for the decay of density with height. The Eady basic state represents the limiting case of infinite stratospheric stability and constant density. We find that the Eady normal mode characteristics hold in the presence of realistic tropopause and stratosphere. In particular, the basic states studied support at the synoptic scale upper–level normal modes. These modes provide simple models for the dynamics of upper–level synoptic–scale waves, as waves supported by the large latitudinal gradients of potential vorticity at the tropopause.

In the presence of infinitesimal positive tropospheric gradients of potential vorticity, the upper–level normal mode solutions no longer exist, as was demonstrated in Green (1960). Disappearance of the normal mode solution when a parameter changes slightly represents a dilemma that we seek to understand. We examine what happens to the upper–level normal modes in the presence of tropospheric gradients of potential vorticity in a series of initial–value experiments. Our results show that the normal modes become slowly decaying quasi–modes. Mathematically the quasi–modes consist of a superposition of singular modes sharply peaked in the phase speed domain, and their decay proceeds as the modes interfere with one another. We repeat these experiments in basic states with a smooth tropopause in the presence of tropospheric and stratospheric gradients, and similar results are obtained. Basic states with positive tropospheric and stratospheric gradients of potential vorticity are found to support upper–level synoptic–scale waves for time scales consistent with observations.

Following Farrell (1989), we then identify a class of near optimal initial conditions for the excitation of upper–level waves. The initial conditions consist of upper–tropospheric disturbances that lean against the shear. They strongly excite upper–level waves not only in the absence of tropospheric potential vorticity gradients, but also in their presence. This result demonstrates that quasi–modes are as likely to emerge from favorably configured initial conditions as real normal modes, although their excitation is followed by a slow decay.

Thesis Supervisor: Dr. Kerry A. Emanuel
Professor of Meteorology

Thesis Supervisor: Dr. Brian F. Farrell
Associate Professor of Dynamic Meteorology

FACTION

On a décidé de faire la nuit
Pour une petite étoile problématique
A-t-on le droit de faire la nuit
Nuit sur le monde et sur notre coeur
Pour une étincelle
Luira-t-elle
Dans le ciel immense du désert

On a décidé de faire la nuit
Pour sa part
De lâcher la nuit sur la terre
Quand on sait ce que c'est
Quelle bête c'est
Quand on a connu quel désert
Elle fait à nos yeux sur son passage

On a décidé de lâcher la nuit sur la terre
Quand on sait ce que c'est
Et de prendre sa faction solitaire
Pour une étoile
encore qui n'est pas sûre
Qui sera peut-être une étoile filante
Ou bien le faux éclair d'une illusion
Dans la caverne que creusent en nous
Nos avides prunelles.

SAINT-DENYS GARNEAU

Acknowledgements

I wish to thank both my advisors, Kerry A. Emanuel and Brian F. Farrell, for their unfailing support and enthusiasm. Initial discussions with Brian led to the determination of the topic, while Kerry provided simple ideas that helped shaping the material of the thesis. I am also grateful to the members of my thesis committee, Frederick Sanders, Randall M. Dole, and Peter H. Stone, for their interest in my research and their careful reading of the original manuscript. Scientific discussions with Christopher A. Davis and R. Alan Plumb were instrumental in the development of chapter 3, and Isaac Held from Princeton University assisted in the calculation of section 4.2.3. I also beneficited from the hospitality and scientific expertise of Richard Rotunno from NCAR.

Among all the students, employees, and professors who create the academic environment at MIT, I wish in particular to thank my long–standing office-mates, James Risbey and Mark D. Handel, Diana Spiegel for her assistance with computers, and Jane McNabb, Joel Sloman, and Tracey Stanelun for their help with administrative details.

During the course of my study at MIT, I enjoyed the friendship and support of Jiin Yun Liang, my swimming partner, the many dinner parties with the family of Carla and Johnny Roberts, the unconventional house of Samuel Blank, and the numerous phone conversations with my sister, Natalie Rivest. I owe a great depth to my parents, Marguerite and Roland Rivest, who always fostered my scientific interests. And finally I am grateful to my husband Benoît for his openness, dynamism, and support.

Contents

List of Figures

List of Tables

Chapter 1

Introduction

1.1 Intent

At midlatitudes in the troposphere and lower stratosphere, the atmospheric circulation consists of a zonal upper–tropospheric jet with horizontal and vertical shears in thermal wind balance with latitudinal temperature gradients. This jet constitutes a reservoir of potential and kinetic energy; it is modulated by quasi–stationary planetary waves and by the moving train of synoptic–scale waves.

Upper–level waves are important at the synoptic scale. They are ubiquitous, and often induce surface cyclogenesis, a mode of development known as "type B" in contrast to "type A" development where no upper–level predecessor is supposed to play an active role (cf. Peterssen and Smebye, 1971).

The intent of this thesis is to develop simple models for the dynamics of

upper–level synoptic–scale waves in order to understand their maintenance in the midlatitude flow, and their genesis. By upper–level waves we mean waves with maximum amplitude in the upper troposphere, and we use the height perturbation on a constant pressure surface as a measure of their amplitude. The expression "synoptic scale" refers here to horizontal scales from two to three thousand kilometers.

Upper–level waves are maintained dynamically against disruption by the ambient shear. Characteristic time scales for disruption by the horizontal and vertical shears at midlatitudes are less than a day. However, the recent study by Sanders (1988) has shown that the life duration of upper–level troughs is typically much longer. In this thesis we explain the maintenance of upper–level waves by finding upper–level wave solutions to basic states representative of the midlatitude flow.

The genesis of upper–level waves is a problem that can be approached in many ways. In this thesis, following Farrell (1989), we study initial conditions that strongly excite upper–level waves.

1.2 Background

1.2.1 Observations

The importance of upper–level air processes at the synoptic scale has long been recognized. Synopticians interested in development of surface cyclones realized

early that they have to be associated with horizontal divergence at upper levels (Brunt, 1930). There followed recognition of the relationship between upper–level patterns of convergence–divergence and trough–ridge (Bjerknes, 1937; Bjerknes and Holmboe, 1944): for synoptic–scale waves, divergence (convergence) is found downstream (upstream) of troughs. In 1971 Peterssen and Smebye observed that a preferred mode of development involves a preexisting upper–level trough, commonly called a "short wave" by synopticians. Figure 1.1, extracted from Palmen and Newton (1969), represents the pattern of convergence–divergence in an upper–level wave.

More recently Sanders (1988) assembled a body of observations of midlatitude upper–level mobile troughs. He considered the 552–decameter contour at the 500–millibar level as indicative of the major band of circumpolar Westerlies, and followed on that contour mobile troughs during the cold season from 1976 to 1986. He noted trough positions every day and dates of first appearance (birth) and last appearance (death). He found an average life duration of 12 days, characteristic eastward phase speed of 15 m/s, and wavelength of 2500 km. In the plane transverse to their direction of propagation troughs appear to be trapped in the jet. In the vertical the disturbances have maximum amplitude at the tropopause with a secondary maximum often seen at the surface. The vertical structure is primarily equivalent barotropic, but some upstream tilt is often present near the surface. Figure 1.2 displays a composite vertical along–stream cross section of upper–level mobile troughs for days subsequent to the day after initiation. Solid lines represent 12–hour height changes and dash lines 12–hour temperature changes. Notice the dipole

structure in the temperature field around the height extrema. The amplitude of the height perturbation is 8 dm and that of the temperature perturbation is 3 ° K.

Recent case studies of extratropical cyclogenesis have confirmed the importance of the upper–level predecessor (Bleck and Mattock, 1984; Uccellini et al., 1986; Davis, 1990). In his study Davis emphasized the Ertel potential vorticity on isentropic surfaces as a useful diagnostic because of its properties of conservation and invertibility (cf. Hoskins et. al., 1985). Figure 1.3 shows an example of an upper–level wave before it induces surface cyclogenesis. Notice in the top panel the lowered tropopause, which we define as the 1.5 PVU contour, in the trough, and the raised tropopause in the ridge. The amplitude of the tropopause deviation is 2.5 km with an accompanying height perturbation of 9 dm, and a propagation rate of about 20 m/s. The bottom panel shows the vertical velocity field: upward motion is found downstream of the trough with an amplitude of 3 cm/s.

It is of interest to examine the flow environment in which upper–level waves propagate. Relevant dynamical quantities are wind and potential temperature, and important derived quantities are static stability and potential vorticity. Previous studies have concentrated on zonally and seasonally averaged data (cf. Fullmer, 1982a, 1982b). In his recent work Davis (1990) has calculated for a case of cyclogenesis the zonal "local" average of dynamical quantities. Averages were computed in a zonal domain determined by the observed wavelength of the wave. We expect this method of averaging to give a better

approximation to the basic flow "felt" by the wave.

An upper–tropospheric jet with zonal winds in excess of 30 m/s, intense vertical and horizontal shears, and a half–width of 1000 km can be seen in the bottom panel of figure 1.4. Notice in the top panel that the static stability in the region of the jet is larger in the lower troposphere than in the upper troposphere, and reaches large values in the stratosphere. The tropopause, which we define as the 1.5 PVU contour, slopes down with latitude. A dynamical quantity of interest is the latitudinal gradient of Ertel potential vorticity along isentropes. Charney and Stern (1962) have shown that it corresponds to the more familiar latitudinal gradient of quasi–geostrophic pseudo–potential vorticity (QPV) in the limit of small isentropic slopes. In the jet region we observe large positive gradients in the neighborhood of the tropopause and considerably smaller positive gradients in the tropospheric interior. A good upper bound for tropospheric gradients is 1 PVU per 10000 km. For an average tropospheric lapse rate of .06 ° K / mb, it corresponds to a QPV gradient comparable to the midlatitude gradient of planetary vorticity, β', (at midlatitudes $\beta' = 1.6 \cdot 10^{-11}$ /ms). Note finally the strong temperature gradients at the surface in the jet region.

1.2.2 Theory

In parallel with the observational studies, theoretical models were developed to explain characteristics of upper–level waves. Following Rossby (1939) and Bjerknes and Holmboe (1944), Peterssen (1956) derived an expression for the

propagation rate of "short waves". He recognized as determining factors the basic state wind profile, the meridional gradient of planetary vorticity, β, and the wavelength of the wave.

With the advent of the theory of baroclinic instability (Charney, 1947; Eady, 1949), theoretical efforts focussed on unstable modes of midlatitude flows. This theory regards extratropical cyclones as unstable modes growing from infinitesimal beginnings in the flow. The Charney basic state has surface temperature gradients and interior potential vorticity gradients, and the instability can be viewed as an interaction between the surface temperature perturbation, the potential vorticity perturbation in the vicinity of the critical level, and their associated circulations. In the Eady basic state there exist temperature gradients at each boundary, and the interior potential vorticity is uniform. We can understand the instability as the interaction of the two surface temperature perturbations and their associated circulations. Both the Charney and Eady unstable modes are characterized by fixed structures that grow in amplitude and propagate in phase.

Simmons and Hoskins (1976) examined basic state flows on a sphere, and found unstable modes resembling the Charney modes. The modes grow at the expense of the potential energy of the basic state. Baroclinic instability associated with the vertical shear is the important mechanism; the barotropic shear mainly determines the latitudinal location and modifies the structure of the modes. In the absence of Ekman damping, the zonal wavelength of maximum instability is 4000 km, the e–folding time scale is on the order of 2

days, and the phase speed is just below 10 m/s. The perturbation fields have maximum amplitude at the ground. In a later work Simmons and Hoskins (1977) found that the effect of a more realistic tropopause is to enhance the signature of the fields at upper levels.

Farrell (1985) suggested that the extratropical atmosphere was not significantly baroclinically unstable because of Ekman pumping at the lower boundary. Following his work a number of authors have studied the baroclinic instability problem in the presence of friction at the lower boundary (Valdes and Hoskins, 1988; Lin and Pierrehumbert,1988). Their results show that the modes with wavelength of 4000 km remain unstable with e–folding time scales not shorter than 3–4 days, even if those with shorter wavelengths are stabilized, for values of the damping parameter characteristic of the oceans.

Following the linear studies, the unstable modes were used as initial conditions to examine the life cycle of baroclinic waves in the nonlinear regime (Simmons and Hoskins, 1978). The simulations show first the growth of a low–level perturbation comparable to a Charney mode. Then a low–level equilibration takes place, resulting in upper–level growth, which is followed by a barotropic decay. Recently, using a model with high resolution, Thorncroft and Hoskins (1990) found that after the larger–scale cyclogenesis, troughs and cutoff cyclones at upper levels are able to interact non–modally with surface frontal zones and to induce strong cyclogenesis.

The baroclinic instability and the life cycle studies offer a series of well–controlled experiments that simulate many dynamical features existing in the

extratropical atmosphere: the low–level and upper–level growth, the formation and motion of frontal zones, the barotropic decay by shearing, and the nonlinear formation of cutoff cyclones and troughs at upper levels. In general the cyclones generated in these studies tend to have too large horizontal scales and too small growth rates, but the addition of moisture may resolve these discrepancies as pointed out in Emanuel et. al (1987). "Type A" development is described in the simulations in the scenario of low–level growth followed by upper–level growth. "Type B" development is also pictured in the high–resolution simulations as secondary cyclogenesis involving troughs or cutoff cyclones at upper levels and surface frontal zones.

To present simple models of "type B" development, a number of authors have examined solutions to carefully chosen initial–value problems, in which perturbation fields are not constrained to behave modally. Farrell (1984) showed that substantial growth can occur above the short–wave cutoff of the Eady basic state, when an upper–level disturbance is located upshear of a low–level one. More recently Rotunno and Fantini (1989) demonstrated that the interference between two neutral Eady waves above the short–wave cutoff can lead to a development similar to "type B".

The theories presented so far give insight into the important dynamical mechanisms involved in midlatitude cyclogenesis. The focuses of the present thesis are the maintenance and genesis of upper–level synoptic–scale waves.

The problem of the maintenance has never been addressed directly in the literature. Rotunno and Fantini (1989) used an upper–level neutral Eady

mode in their initial–value experiments. We believe that these modes are simple and useful models for the dynamics of upper–level waves at midlatitudes. As will be shown in chapter 3, the rigid lid that seems unrealistic in the Eady basic state corresponds to the limit of infinite stratospheric stability, and upper–level wave solutions still exist in the presence of realistic tropopause and stratosphere. The upper–level waves are then tied dynamically to the large potential vorticity gradients present at the tropopause in the jet region (remember figure 1.4). Figure 1.5 displays the zonal–vertical cross section of an upper–level neutral Eady wave solution at the synoptic scale. Note the maximum amplitude at the upper lid, the cold troughs and warm ridges, and the upward (downward) motion taking place downstream (upstream) of troughs. There is a clear resemblance between the tropospheric fields depicted in figure 1.5 and those shown in figures 1.2 and 1.3.

Some answers to the question of the genesis of upper–level waves can be found in the theories mentioned earlier. Upper–level growth occurs after low–level equilibration in the life cycle experiments. This result is in line with recent studies of baroclinic instability, which show that basic state flows with baroclinicity concentrated in the upper troposphere lead to upper–level unstable modes (Snyder and Lindzen, 1988; Whitaker and Barcilon, 1990). In this thesis we take the initial–value approach that allows consideration of non–modal perturbations. Following Farrell (1989), we identify a class of near optimal initial conditions for the excitation of upper–level waves.

1.3 Outline of the thesis

This thesis is organized as follows:

In chapter 2 we present the theoretical framework: the equations, the mathematical problems considered, and their numerical solutions. Chapter 3 contains a discussion of waves on generalized Eady basic states, with an emphasis on upper–level neutral wave solutions. In chapter 4 we explain what happens to upper–level synoptic–scale waves in the presence of positive tropospheric gradients of potential vorticity, thus resolving a dilemma noticed by Green (1960). We study in chapter 5 upper–level wave solutions on basic state flows with a smooth tropopause and a stratosphere, and we also examine their excitation from a class of near optimal initial conditions. Finally we discuss in chapter 6 the general significance of the results presented in this thesis.

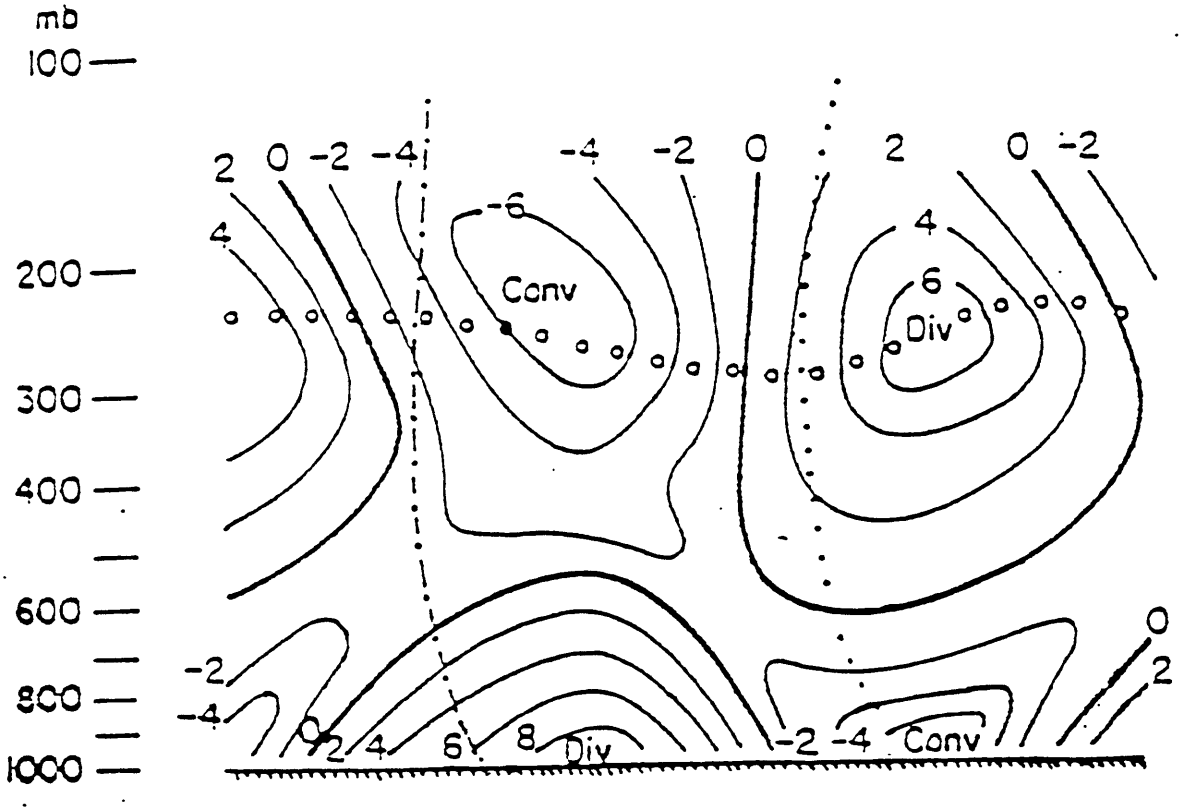

Figure 1.1: Vertical along-stream cross section of the divergence at intervals of $2 \cdot 10^{-5}$ /s in an upper-level wave. The ridge line (dash - dot line) and the trough line (dot line) are indicated. From Palmen and Newton (1969).

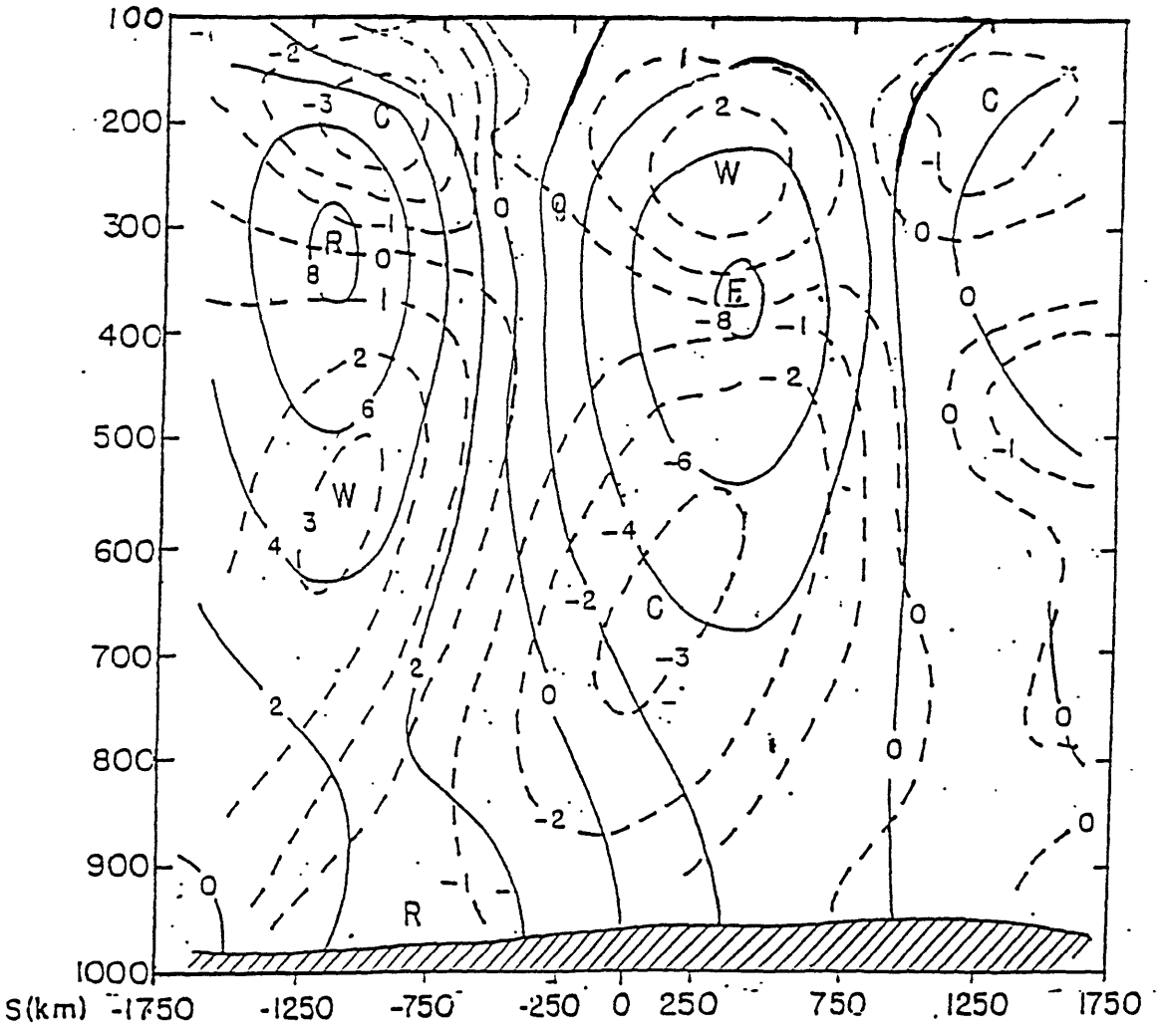

Figure 1.2: Composite vertical along–stream cross section of 12–hour height change (solid lines) at intervals of 2 dm and of 12–hour temperature change of mean temperature between standard levels (dashed lines) at intervals of 1° K for days subsequent to the day after initiation. From Sanders (1988).

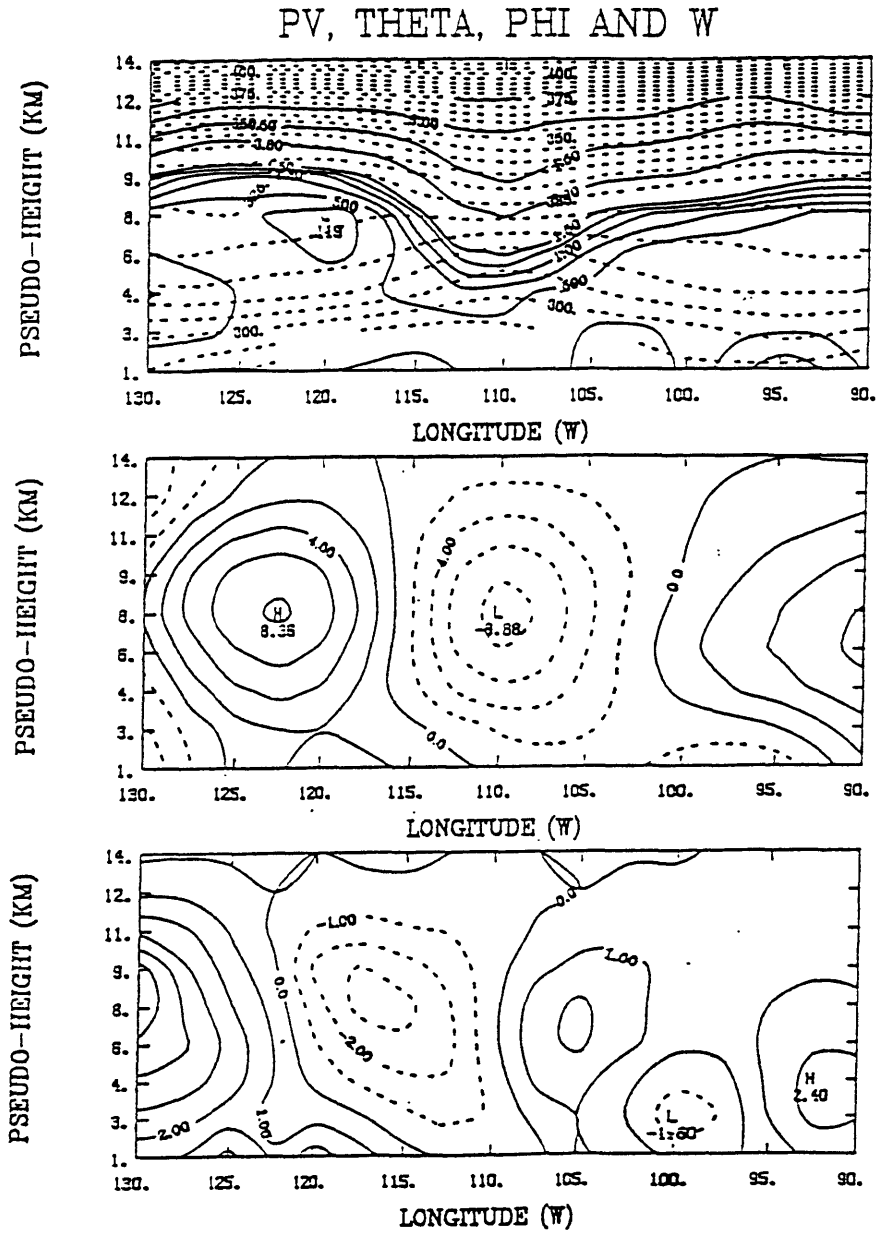

Figure 1.3: Height–longitude cross section of the following fields, November 9 1988, 12 GMT. Top panel: Ertel potential vorticity (solid lines) and potential temperature (dash lines). The contour intervals for the Ertel PV are .1 below .5, .25 for values between .5 and 1.5, and 1.5 for values above 1.5. The units are PVU introduced in Hoskins et. al (1985). The contour interval is 5 ° K for the potential temperature. Middle panel: Height perturbation field at intervals of 2 dm. Bottom panel: Vertical velocity perturbation field at intervals of 1 cm/s. From Davis (1990).

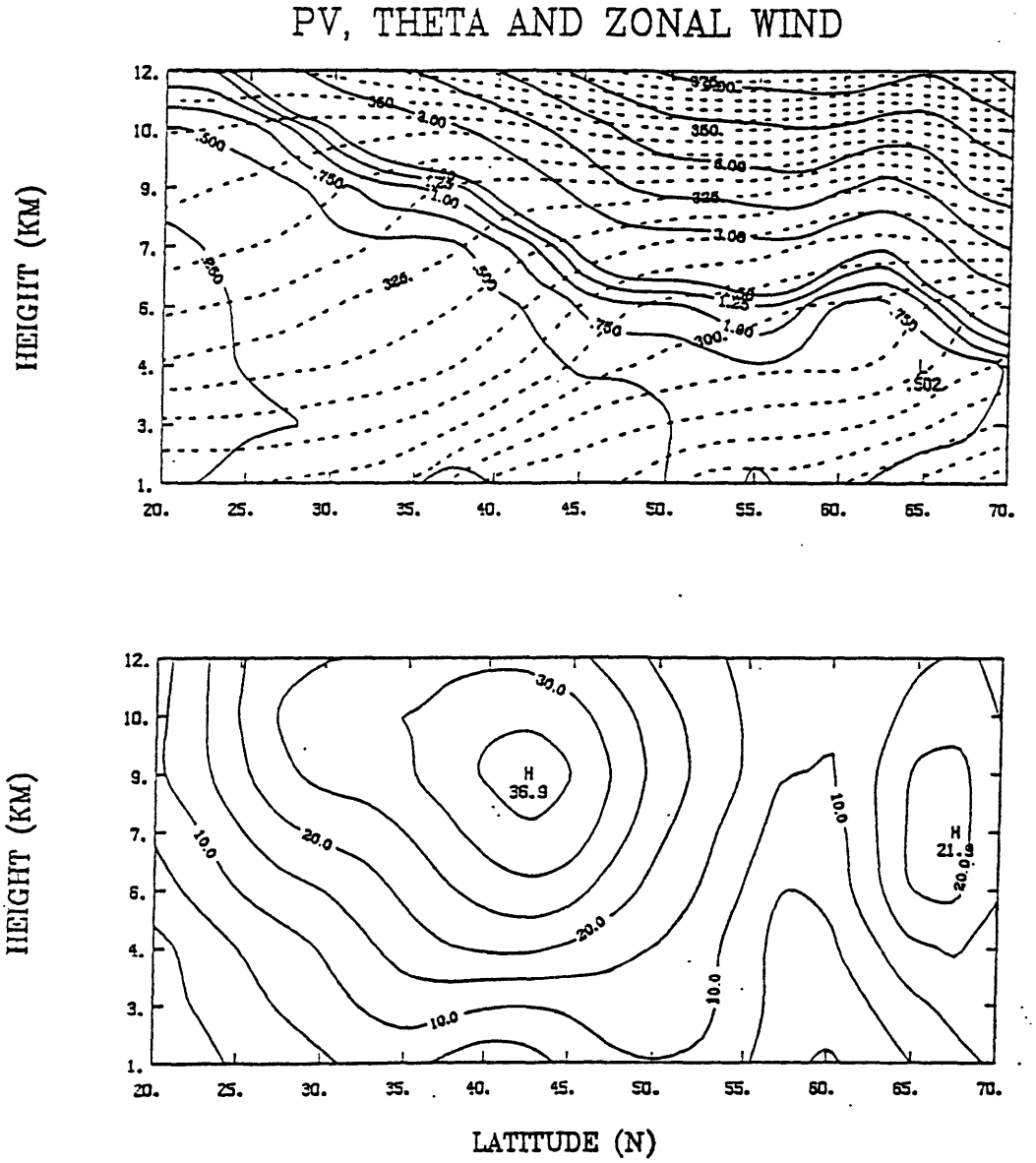

Figure 1.4: Height–latitude cross section of the fields averaged from 120 to 80 deg longitude East, November 9 1988, 12 GMT. Top panel: Ertel potential vorticity (solid lines) and potential temperature (dash lines). The contour intervals for the Ertel PV are .1 below .5, .25 for values between .5 and 1.5, and 1.5 for values above 1.5. The units are PVU introduced in Hoskins et. al (1985). The contour interval is 5 ° K for the potential temperature. Bottom panel: Zonal wind at intervals of 5 m/s from Davis (1990).

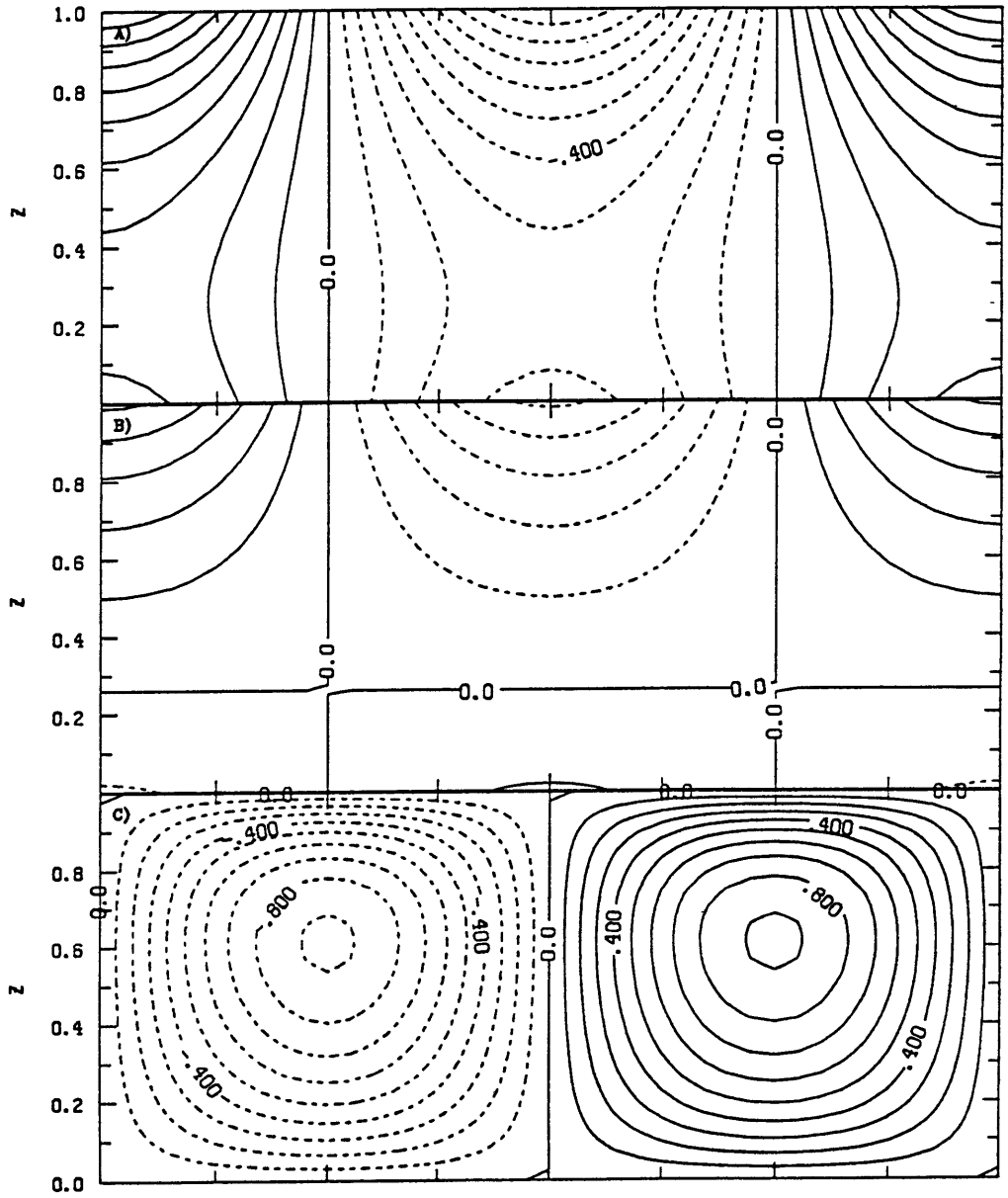

Figure 1.5: Midchannel $x - z$ cross section of the inviscid upper–level neutral Eady wave solution at $k = 2.3$ and $l = 1.4$ for the Boussinesq basic state (S1,$a = 0$, $N_2^2 = \infty$): (a) streamfunction, (b) potential temperature, and (c) vertical velocity. The contour interval is .1 in (a), .5 in (b), and .1 in (c), and the streamfunction amplitude is fixed to unity at the upper lid. The nondimensionalization is as in chapter 2 and parameter values as in chapter 3.

Chapter 2

Theoretical framework

2.1 Equations

We present here the equations used throughout this thesis. The quasi–geostrophic (QG) set of equations is chosen to model the dynamics of upper–level synoptic–scale waves. The QG approximation stems from the primitive equations in the limit of small aspect ratio, that is the ratio of the vertical to the horizontal scale; small Rossby number, that is the ratio of the relative to the planetary vorticity; and large Richardson number, that is the square of the ratio of the static stability to the vertical shear. QG motions are characterized by hydrostatic and geostrophic balances, and therefore by thermal wind balance. The Richardson number constraint also implies small isentropic slopes, and consistency of the QG approximation requires a static stability that varies only vertically. For reference see Pedlosky, 1979, chapter 6, or Charney, 1973, pp 226–236.

At midlatitudes in the region of the jet, the Rossby number can be of order unity, the Richardson number can be small, and moreover the stability typically varies horizontally. Nevertheless, the QG equations provide a useful qualitative model of synoptic–scale dynamics.

2.1.1 Quasi–geostrophic dynamics in a basic state flow

Let us consider perturbations $[q, \psi, u, v, w, \theta]\ (x, y, z, t)$
in a basic state flow $[Q, \Psi, U, \Theta](y, z)$,
where $Q + q$ is the total QG pseudo–potential vorticity (QPV), $\Psi + \psi$ the geostrophic streamfunction, $U + u$ the zonal geostrophic wind, v the meridional geostrophic wind, w the vertical velocity, $\Theta + \theta$ the potential temperature, and where (x, y, z, t) are the zonal, meridional, vertical, and time coordinates. The nondimensional equations for the basic state are:

$$Q_y = \beta - \left[\frac{\partial^2}{\partial y^2} + \frac{1}{\rho}\frac{\partial}{\partial z}\left(\frac{\rho}{N^2}\frac{\partial}{\partial z}\right)\right] U, \tag{2.1}$$

$$U = -\frac{\partial \Psi}{\partial y}, \tag{2.2}$$

$$\Theta = \frac{\partial \Psi}{\partial z}; \tag{2.3}$$

and for the perturbation fields:

$$\left[\frac{\partial}{\partial t} + U\frac{\partial}{\partial x} + J(\psi, \ )\right] q = -Q_y \frac{\partial \psi}{\partial x}, \tag{2.4}$$

$$\left[\frac{\partial}{\partial t} + U\frac{\partial}{\partial x} + J(\psi, \ )\right] \theta = -N^2 w - \Theta_y \frac{\partial \psi}{\partial x}, \tag{2.5}$$

$$\text{where } q = \left[\nabla_H^2 + \frac{1}{\rho}\frac{\partial}{\partial z}\left(\frac{\rho}{N^2}\frac{\partial}{\partial z}\right)\right] \psi, \tag{2.6}$$

$$
\begin{aligned}
u &= -\frac{\partial \psi}{\partial y},\ v = \frac{\partial \psi}{\partial x},\ \theta = \frac{\partial \psi}{\partial z}, \\
J(A,B) &= A_x B_y - A_y B_x, \\
\nabla_H^2 &= \frac{\partial^2}{\partial x^2} + \frac{\partial^2}{\partial y^2},
\end{aligned}
\tag{2.7}
$$

$N^2(z), \rho(z)$ are the reference static stability and density profiles, and β the latitudinal gradient of planetary vorticity. (2.4) expresses the conservation of total QPV following geostrophic motions: the meridional advection of basic state QPV, Q, modifies the eddy QPV ,q, following geostrophic motions. The thermodynamic equation, (2.5), relates changes in eddy potential temperature, θ, following geostrophic motions, to adiabatic warming or cooling, and meridional advection of basic state potential temperature, Θ.

Choosing a vertical scale, H, a horizontal scale, $L \equiv N_0 H/f_0$, a velocity scale, U_0, a reference static stability, potential temperature, and density, respectively N_0, θ_0, ρ_0, and an average planetary vorticity, f_0, it is possible to recover the dimensional variables and parameters (that are primed):

$$
\begin{aligned}
(x', y', z') = L\left(x, y, \frac{H}{L}z\right), &\qquad t' = \frac{L}{U_0}t, \\
N' = N_0 N, &\qquad \rho' = \rho_0 \rho, \\
(Q', q') = R_0 f_0 (Q, q), &\qquad (\Psi', \psi') = U_0 L(\Psi, \psi), \\
(U', u', v') = U_0 (U, u, v), &\qquad (\Theta', \theta') = \theta_0 \frac{f_0 L U_0}{gH}(\Theta, \theta), \\
w' = R_0 \frac{H}{L} U_0 w, &\qquad \beta' = \frac{\beta U_0}{L^2},
\end{aligned}
\tag{2.8}
$$

where R_0 is the Rossby number, $R_0 \equiv U_0/Lf_0$.

In this thesis we are concerned with synoptic–scale motions in the region of

Table 2.1: Dimensional and nondimensional variables [a]

(x', y')	=	900 km	(x, y)
(z')	=	9 km	(z)
(t')	=	.39 day	(t)
$(Z'(z=1))$	=	24 dm	(ψ)
$(P'(z=0))$	=	24 mb	(ψ)
(U', u', v')	=	27 m/s	(U, u, v)
(Θ', θ')	=	8.1 ° K	(Θ, θ)
(w')	=	8.1 cm/s	(w)

[a] Z' is the height at a pressure surface typical of the tropopause, and P' is the pressure at the ground.

the jet. We choose: $f_0 = 10^{-4}$ /s, $g = 10\,\mathrm{m/s^2}$, $N_0 = 10^{-2}$ /s^2, $\beta' = 1.6 \cdot 10^{-11}$ /ms, and $H = 9\,\mathrm{km}$ that is roughly the tropopause height in the middle of the jet. This value of H implies a Rossby radius, $L = 900\,\mathrm{km}$. Also, let us consider $U_0 = \gamma_0 H$, where γ_0 is an average tropospheric shear so that fixing $\gamma_0 = 3\,(\mathrm{m/s})/\mathrm{km}$ yields $U_0 = 27\,\mathrm{m/s}$. For these parameter values the nondimensional beta and the Rossby number are: $\beta = .5$ and $R_0 = .3$. As noted in chapter 1, this value of β corresponds to a reasonable upper bound for the value of QPV tropospheric gradients. Table 2.1 summarizes the correspondence between dimensional and nondimensional variables.

2.1.2 Linear waves in a zonal channel

We consider linear waves confined in a zonal channel, in basic state winds with no meridional dependency. Such basic state flows lead to a mathematical problem for the perturbation fields that is separable in y and z. As was noted in the introduction, actual studies of unstable waves on basic state winds

with meridional dependency have shown remarkable similarities with studies of artificially confined unstable waves (Simmons and Hoskins, 1976; Ioannou and Lindzen, 1986; Lin and Pierrehumbert, 1988; Valdes and Hoskins, 1988). The presence of barotropic shear usually acts to confine the perturbation in the jet axis, and to slightly reduce the instability.

Let us assume a density profile that decays exponentially with height throughout the domain,

$$\rho = \exp[-sz]. \tag{2.9}$$

From (2.1),(2.2), and (2.3), the basic state equations are:

$$\begin{aligned} Q_y &= \beta - \frac{1}{\rho}\frac{d}{dz}\left(\frac{\rho}{N^2}\frac{dU}{dz}\right) \\ &= \beta + \frac{s_N}{N^2}\frac{dU}{dz} - \frac{1}{N^2}\frac{d^2U}{dz^2}, \qquad (2.10) \\ \Psi &= -U(z)\,y, \qquad (2.11) \\ \Theta &= \frac{\partial \Psi}{\partial z}, \qquad (2.12) \\ \text{where } s_N &= s + \frac{1}{N^2}\frac{dN^2}{dz}. \qquad (2.13) \end{aligned}$$

For perturbation fields of the form,

$$\begin{aligned} [q,\psi,v,w,\theta](x,y,z,t) &= Re\left([\tilde{q},\tilde{\psi},\tilde{v},\tilde{w},\tilde{\theta}](z,t)e^{ikx}\right)\sin ly, \\ u(x,y,z,t) &= Re\left(\tilde{u}(z,t)e^{ikx}\right)\cos ly, \qquad (2.14) \end{aligned}$$

where $l = \pi/L_y$, $k = 2\pi/L_x$, L_y is the channel width, and L_x the zonal wavelength, the linear equations are [from (2.4),(2.5),(2.6),(2.7)]:

$$\left[\frac{\partial}{\partial t} + ikU\right]\ \tilde{q} = -ikQ_y\tilde{\psi}, \tag{2.15}$$

$$\left[\frac{\partial}{\partial t} + ikU\right]\frac{\partial \tilde{\psi}}{\partial z} = -N^2\tilde{w} - ik\Theta_y\tilde{\psi}, \tag{2.16}$$

$$\text{where } \tilde{q} = \left[-K^2 - \frac{s_N}{N^2}\frac{\partial}{\partial z} + \frac{1}{N^2}\frac{\partial^2}{\partial z^2}\right]\tilde{\psi}, \tag{2.17}$$

$$\tilde{u} = -il\tilde{\psi},\ \tilde{v} = ik\tilde{\psi},\ \tilde{\theta} = \frac{\partial\tilde{\psi}}{\partial z}, \tag{2.18}$$

and K is the total horizontal wavenumber, $K^2 = k^2 + l^2$.

The equations presented so far need to be completed by suitable boundary conditions in the vertical: at the upper lid, $z = z_u$,

$$w = -\eta_u \nabla_H^2 (\Psi + \psi), \tag{2.19}$$

and at the lower lid, $z = z_l$,

$$w = \eta_l \nabla_H^2 (\Psi + \psi), \tag{2.20}$$

where η_l, η_u are some boundary layer parameters. We discuss in Appendix A values for η_l that are characteristic of the extratropical atmosphere. Substituting $\tilde{w}$ from (2.16) yields:

$$\left[\frac{\partial}{\partial t} + ikU\right]\frac{\partial\tilde{\psi}}{\partial z} + ik\Theta_y\tilde{\psi} - \eta_l N^2 K^2\tilde{\psi} \doteq 0 \text{ at } z = z_l, \tag{2.21}$$

$$\left[\frac{\partial}{\partial t} + ikU\right]\frac{\partial\tilde{\psi}}{\partial z} + ik\Theta_y\tilde{\psi} + \eta_u N^2 K^2\tilde{\psi} = 0 \text{ at } z = z_u. \tag{2.22}$$

In the following chapters we are also going to consider semi–infinite vertical domains, and use approximate boundary conditions. Derivation of these boundary conditions can be found in Appendix B.

This system has the interesting property that the basic state flow and the perturbation can exchange energy. Let us define the total perturbation energy, E_T, as the sum of the potential and kinetic energy,

$$E_T = \int_{z_l}^{z_u}\int_0^{L_y} dy\,dz\,\frac{\rho}{2}\overline{\left[\left(\frac{\partial\psi}{\partial x}\right)^2 + \left(\frac{\partial\psi}{\partial y}\right)^2 + \frac{1}{N^2}\left(\frac{\partial\psi}{\partial z}\right)^2\right]}, \tag{2.23}$$

$$\text{where } \overline{(\ )} = \frac{1}{L_x}\int_0^{L_x} dx(\ ). \tag{2.24}$$

From (2.4) and (2.5) we obtain in the absence of friction:

$$\frac{dE_T}{dt} = -\int_{z_l}^{z_u}\int_0^{L_y} dy\, dz\, \frac{\rho U_z}{N^2}\overline{\frac{\partial\psi}{\partial x}\frac{\partial\psi}{\partial z}}. \tag{2.25}$$

When the perturbation streamfunction tilts upshear with height in average, the right–hand side of (2.25) is positive and the perturbation energy increases with time, whereas when it tilts downshear, the perturbation energy decreases with time. Obviously when the perturbation gains or loses energy, the mean flow accordingly loses or gains energy, but this feedback is not considered in the linear problem.

2.1.3 The normal mode approach

It is possible to find normal mode solutions $[\hat{q}, \hat{\psi}...]$ that are of fixed structure, and that grow and propagate at fixed rate and speed. For the system of equations presented in this section, the discrete normal modes are the only physically acceptable modes that satisfy these conditions.

Let us express

$$\tilde{\psi}(z,t) = \hat{\psi}(z)e^{-ikct},$$

where c is complex, $c = c_r + ic_i$. From (2.15),(2.17), (2.21), and (2.22) (in the case of lower and upper rigid boundary conditions), we get an eigenvalue problem for $\hat{\psi}(z)$ and c:

$$(U-c)\left[\frac{1}{N^2}\frac{d^2}{dz^2} - \frac{s_N}{N^2}\frac{d}{dz} - K^2\right]\hat{\psi} + Q_y\hat{\psi} = 0, \tag{2.26}$$

$$\text{with } (U-c)\frac{d\hat{\psi}}{dz} + \Theta_y\hat{\psi} + i\frac{K^2}{k}\eta_l N^2\hat{\psi} = 0 \text{ at } z = z_l, \tag{2.27}$$

$$(U-c)\frac{d\hat{\psi}}{dz} + \Theta_y\hat{\psi} - i\frac{K^2}{k}\eta_u N^2\hat{\psi} = 0 \text{ at } z = z_u. \tag{2.28}$$

The system of equations (2.26), (2.27), and (2.28) admits two different classes of solutions: the discrete normal modes and the continuous spectrum of singular neutral modes. See for reference, Drazin and Reid, 1981, pp 147–153. Each singular mode has a discontinuous derivative at the height of the domain, z_c, where $(U(z_c) - c)$ vanishes. A single singular mode is then not a physically acceptable solution. A superposition of singular modes may represent an acceptable solution, but its vertical structure generally changes with time as the different modes interfere with one another. The discrete normal modes are hence the only physically acceptable modes of the problem, and are usually referred to as *the normal modes* of the problem.

From equations (2.15) to (2.18), the normal mode solutions for the other perturbation fields are:

$$\hat{q} = -\frac{Q_y}{U-c}\hat{\psi}, \tag{2.29}$$

$$\hat{u} = -l\hat{\psi},\ \hat{v} = ik\hat{\psi},\ \hat{\theta} = \frac{\partial\hat{\psi}}{\partial z}, \tag{2.30}$$

$$\hat{w} = -\frac{ik}{N^2}\left[\Theta_y\hat{\psi} + (U-c)\frac{d\hat{\psi}}{dz}\right]. \tag{2.31}$$

There exist many theorems concerning the properties of normal mode solutions, among which the Charney–Stern theorem is probably the best known (cf. Charney and Stern, 1962). It states that a necessary condition for instability in the inviscid limit is that the meridional QPV gradient with contributions

from the boundaries,

$$Q_y + \frac{\Theta_y}{N^2}\left(\delta(z_l) - \delta(z_u)\right),$$

changes sign over the domain. Note that the absence of normal mode instability does not rule out the possibility of transient growth associated with less constrained perturbations.

2.1.4 The initial–value approach

The interest of the initial–value approach lies in the fact that it goes beyond some limitations of the normal mode approach. It is possible in an initial–value problem to study the evolution of arbitrary initial disturbances, which is not possible with the normal mode solutions that do not form a complete set (cf. Pedlosky, 1964). Also the initial–value approach allows the examination of less constrained perturbations, which do not have fixed structure, growth rate, and phase speed. As mentioned in chapter 1, it was used with success to model "type B" development (Farrell, 1984; Rotunno and Fantini, 1990). In the initial–value approach, (2.15), (2.17), (2.21), and (2.22) are integrated forward in time, for a given initial condition, $\tilde{\psi}_0(z)$.

Let us examine further the properties of the modes that determine the mechanisms present in the initial–value problem. It is possible to rewrite (2.26), (2.27), and (2.28) in a matrix form:

$$[A]\,|\psi_j> = c_j|\psi_j> . \tag{2.32}$$

where $[A]$ is a matrix for a finite–difference scheme at a certain truncation,

N, and becomes a differential operator in the continuous limit; $|\psi_j>$ is the jth eigenvector among the totality of eigenvectors that encompasses both the singular and the discrete ones, and c_j is its associated eigenvalue. We have used here the ket and bra notation where a vector $|\psi_j>$ has a conjugate transpose $<\psi_j|$ (cf. Cohen–Tannoudji et al, 1977).

The matrix $[A]$ is not Hermitian (or self–adjoint in the continuous limit) in the general case with shear. This implies that the modes, $|\psi_j>$, are not orthogonal, and that quantities quadratic in ψ, such as energy, are not necessarily conserved (Held, 1985). This is consistent with (2.25).

Let us look at the Hermitian transpose linear system,

$$[A]^H|\psi_m^a>=d_m|\psi_m^a>,$$

where $[A]^H$ is the Hermitian transpose of $[A]$, and d_m the eigenvalue associated with the mth eigenvector, $|\psi_m^a>$. The Hermitian transpose matrix corresponds in the continuous limit to the adjoint operator. See Ince (1926) for a discussion of differential operators and their adjoint. It is easy to show that

$$d_m = c_m^*,$$

where the * refers to the complex conjugate, and that a special biorthogonality relationship links the modes of the system and its Hermitian transpose,

$$\frac{<\psi_m^a|\psi_j>}{<\psi_j^a|\psi_j>} = \delta_{mj}, \tag{2.33}$$

where δ_{mj} is the function of Kroenecker. This result also holds in the continuous limit.

Once both the modes of the system and of its Hermitian transpose are known, the initial–value problem can easily be solved. The modes $|\psi_j>$ form a complete set, and the solution can be expressed as

$$|\psi(t)>=\sum_{j=1}^{N} a_j|\psi_j> e^{-ikc_jt}. \tag{2.34}$$

For a given initial condition, $|\psi_0>$, the coefficients a_j can be determined with the biorthogonality relationship,

$$a_j = \frac{<\psi_j^a|\psi_0>}{<\psi_j^a|\psi_j>}.$$

Farrell (1982, 1989) used this technique to solve the initial–value problem. The important mechanism in (2.34) is the interference between the nonorthogonal modes. The total energy is then not the sum of the individual modal energies. Effects of this kind are discussed in Lindzen et. al (1982), and Rotunno and Fantini (1989), where the interference takes place between two discrete modes.

2.2 Numerical implementation

We explain in this section the numerical techniques used to solve the mathematical problems encountered in the thesis. Let us introduce a new variable, ϕ,

$$\phi = \frac{e^{-sz/2}}{\sqrt{N^2}}\psi, \tag{2.35}$$

which simplifies the equations in the vertical direction.

2.2.1 The discrete eigenvalue problem

The set of equations solved for the discrete eigenvalue problem consists of the interior equation, (2.26), completed by boundary conditions at the lower boundary, either (2.27) or (B.4), and at the upper boundary, either (2.28) or (B.2). Since in the case of the discrete eigenmodes there is no singularity at the critical level, the equations can be divided by $U - c$. We can then express them in the following manner:

$$\begin{aligned} \frac{d^2\hat{\phi}}{dz^2} + \mathcal{D}\hat{\phi} &= 0, \\ \frac{d\hat{\phi}}{dz} + \mathcal{D}_l\hat{\phi} &= 0 \text{ at } z = z_l, \\ \frac{d\hat{\phi}}{dz} + \mathcal{D}_u\hat{\phi} &= 0 \text{ at } z = z_u, \end{aligned}$$

$$\text{where } \mathcal{D} = \left[\frac{1}{2}\frac{d^2 \ln N^2}{dz^2} - \frac{s_N^2}{4} - N^2\left(K^2 - \frac{Q_y}{U-c}\right)\right],$$

and where $\mathcal{D}_l$ and $\mathcal{D}_u$ depend on the type of boundary conditions used.

This set of differential equations can be written as a matrix equation with the fourth–order discretization scheme described in Appendix C:

$$[\mathcal{L}(c)]|\phi >= 0, \tag{2.36}$$

where $[\mathcal{L}(c)]$ is an $N \times N$ tridiagonal matrix, and $|\phi >$ the eigenvector at a certain truncation N. We solve the matrix problem (2.36) using a shooting method proposed by Kuo (1979). The calculations are performed in double precision, and we verified the accuracy of the scheme with a known analytical solution, the low–level edge wave. Both the errors in the eigenvalue c and in the modified streamfunction $|\phi >$ were found to go as $(\Delta z)^4$.

Diagnostics

From the eigenvalue c and eigenvector $|\phi>$, it is easy to compute the growth rate, $\Omega = kc_i$, and phase speed, c_r;the streamfunction, $|\psi>$, with (2.35); and the QPV, $|q>$, from (2.29). The potential temperature field is calculated with the fourth–order compact scheme (Haltiner and Williams, 1980, p.137):

$$\theta_{k+1} + 4\theta_k + \theta_{k-1} = \frac{3}{\triangle z}(\psi_{k+1} - \psi_{k-1}).$$

The values of θ_1 and θ_N can be calculated from the boundary conditions. We then have a tridiagonal $N-1 \times N-1$ matrix equation that is easily solved by Gaussian elimination. Once both the streamfunction and potential temperature fields are known, it is easy to compute $|w>$ with (2.31).

2.2.2 The full eigenvalue problem

We seek here to calculate the full spectrum of eigenmodes, discrete and continuous. The set of equations solved is the same as for the discrete eigenvalue problem. However, the equations cannot be divided by $U - c$; they take the following form:

$$\begin{aligned}
c\left(\frac{d^2\hat{\phi}}{dz^2} + \mathcal{M}\hat{\phi}\right) &= U(z)\left(\frac{d^2\hat{\phi}}{dz^2} + \mathcal{M}\hat{\phi}\right) + Q_y N^2 \hat{\phi}, \\
c\left(\frac{d\hat{\phi}}{dz} + \mathcal{M}_l\hat{\phi}\right) &= U_l\left(\frac{d\hat{\phi}}{dz} + \mathcal{M}_l\hat{\phi}\right) + \mathcal{N}_l\hat{\phi} \text{ at } z = z_l, \\
c\left(\frac{d\hat{\phi}}{dz} + \mathcal{M}_u\hat{\phi}\right) &= U_u\left(\frac{d\hat{\phi}}{dz} + \mathcal{M}_u\hat{\phi}\right) + \mathcal{N}_u\hat{\phi} \text{ at } z = z_u, \\
\text{where } \mathcal{M} &= \left[\frac{1}{2}\frac{d^2 \ln N^2}{dz^2} - \frac{s_N^2}{4} - N^2K^2\right],
\end{aligned} \tag{2.37}$$

and $\mathcal{M}_l$, $\mathcal{N}_l$, $\mathcal{M}_u$, and $\mathcal{N}_u$ depend on the type of boundary conditions used.

We discretize this set of equations with the scheme described in Appendix C, and we obtain the following matrix equation:

$$[T]|\phi_j >= c_j[S]|\phi_j >,$$

where both $[S]$ and $[T]$ are $N \times N$ tridiagonal matrices, $|\phi_j >$ is the jth eigenvector, and c_j its associated eigenvalue.

We solve the matrix problem by first calculating the inverse of $[S]$, $[S]^{-1}$. We are then left with a typical eigenvalue problem,

$$[F]|\phi_j >= c_j|\phi_j >,$$

where $[F] = [S]^{-1}[T]$. We calculate the adjoint modes $|\phi_j^a >$ with the help of the biorthogonality relationship for ϕ:

$$< \phi_j^a|\phi_k >= \delta_{jk}.$$

Let us define the matrix $[E]$ as the matrix of eigenvectors,

$$[E] = \{|\phi_1 >, ..., |\phi_j >, ..., |\phi_N >\}.$$

Then the rows of its inverse, $[E]^{-1}$, are simply the adjoint eigenvectors, $|\phi_j^a >$.

The numerical calculations are performed in double precision and errors greater than 10^{-10} are not tolerated. IMSL routines LEQT1B and EIGRF are used to calculate respectively inverses of matrices and solutions to the eigenvalue problems.

Diagnostics

The only diagnostics we calculate in the case of the full eigenvalue problem are $|\psi_j>$ and $|\psi_j^a>$. The former is calculated with (2.35), and it is easy to show that the latter corresponds to:

$$|\psi_j^a>=\frac{e^{-sz/2}}{\sqrt{N^2}}|\phi_j^a> .$$

2.2.3 The initial–value problem

The initial–value problem consists of solving (2.15) and (2.17), completed by boundary conditions, (2.21) or (B.12), and (2.22) or (B.10). We express the equations in terms of ϕ and p, where

$$p = \sqrt{N^2}e^{-sz/2}q. \tag{2.38}$$

The equations take the following form:

$$\frac{\partial \tilde{p}}{\partial t} = -ikU\,\tilde{p} - ikN^2Q_y\,\tilde{\phi}, \tag{2.39}$$

$$\frac{\partial}{\partial t}\left(\frac{\partial \tilde{\phi}}{\partial z} + \mathcal{M}_l\tilde{\phi}\right) = -ik\left[U_l\left(\frac{\partial \tilde{\phi}}{\partial z} + \mathcal{M}_l\tilde{\phi}\right) + \mathcal{N}_l\tilde{\phi}\right] \text{ at } z = z_l, \tag{2.40}$$

$$\frac{\partial}{\partial t}\left(\frac{\partial \tilde{\phi}}{\partial z} + \mathcal{M}_u\tilde{\phi}\right) = -ik\left[U_u\left(\frac{\partial \tilde{\phi}}{\partial z} + \mathcal{M}_u\tilde{\phi}\right) + \mathcal{N}_u\tilde{\phi}\right] \text{ at } z = z_u, \tag{2.41}$$

$$\text{where } \tilde{p} = \frac{\partial^2 \tilde{\phi}}{\partial z^2} + \mathcal{M}\tilde{\phi}, \tag{2.42}$$

$\mathcal{M}$ is as defined in (2.37), and $\mathcal{M}_l$, $\mathcal{N}_l$, $\mathcal{M}_u$, and $\mathcal{N}_u$ depend on the type of boundary conditions used.

We start the time integration with the initial conditions $|p_0>$, $|\phi_0>$, $\left(\frac{\partial\tilde{\phi}}{\partial z}+\mathcal{M}_l\tilde{\phi}\right)^{z=z_l,t=0}$, and $\left(\frac{\partial\tilde{\phi}}{\partial z}+\mathcal{M}_u\tilde{\phi}\right)^{z=z_u,t=0}$. (2.39), (2.40), and (2.41) are integrated forward in time with the Euler modified scheme (Method B in Young, 1968). This scheme slightly amplifies in time the amplitude of a neutral wave, and overestimates its propagation speed. The vertical scheme described in Appendix C is used to solve (2.42) for $|\phi>$. The total scheme is then second–order accurate in time and fourth–order accurate in the vertical direction. Calculations are performed in double precision, and we verified the orders of accuracy with a known analytical solution, the low– level edge wave.

Diagnostics

At each time step of the integration, $|\phi>$, $|p>$, and the boundary terms are known. From them it is easy to calculate $|\psi>$ with (2.35), and $|q>$ with (2.38). The potential temperature field, $|\theta>$, is computed with the same method that was used in the case of the discrete mode (remember section 2.2.1).

We calculate the vertical velocity field by solving a modified w–equation. Let us define a new variable,

$$\tilde{\omega} = e^{sz/2}\,\tilde{w},$$

which obeys the following relation:

$$\frac{\partial^2\tilde{\omega}}{\partial z^2}+\mathcal{V}\tilde{\omega}=\mathcal{W}, \tag{2.43}$$

$$\text{where } \mathcal{V} = -N^2K^2 - s^2/4, \text{ and } \mathcal{W} = ike^{-sz/2}\left(\beta\tilde{\theta} - 2K^2U_z\tilde{\psi}\right).$$

Once $|\psi>$ and $|\theta>$ are computed, the right–hand side of the equation is defined. The values of $\tilde{\omega}$ at each boundary are needed to close the problem.

In the case of rigid boundary conditions the values at the boundaries are simple functions of $|\psi>$ from (2.19) and (2.20). In the case of approximate boundary conditions for semi–infinite domain it is more difficult. Remember that the vertical velocity field can be expressed as

$$\tilde{w} = \frac{-1}{N^2}\left[\frac{\partial\tilde{\theta}}{\partial t} + ik\left(U\tilde{\theta} - U_z\tilde{\psi}\right)\right].$$

Once $|\theta>$ and $|\psi>$ are calculated, only the first term of the right–hand side remains unknown at the boundaries.

We evaluate this term in the following manner. The Euler modified time scheme is a two–step process, and the values of boundary potential temperature fields from the middle of the time step can be calculated. We can then approximate the boundary terms $\frac{\partial\tilde{\theta}}{\partial t}$ with a first–order backward Euler time scheme, and this allows us to get $\tilde{\omega}$ at each boundary.

The modified w–equation (2.43) is then discretized with the scheme described in Appendix C. Once the values at the boundaries are known, we are left with an $N-1 \times N-1$ tridiagonal matrix problem that is easily solved by Gaussian elimination.

In the initial–value simulations we also calculate two scalar diagnostics, the total perturbation energy, E_T, and the phase speed at a given height, $c|^{z_g}$. E_T

is defined in (2.23). After integrating in the x and y directions and changing the variables, (2.23) becomes:

$$E_T = \frac{L_y}{8} \int_{z_l}^{z_u} dz \left[K^2 N^2 |\tilde{\phi}|^2 + \left| \frac{\partial \tilde{\phi}}{\partial z} + s_N \tilde{\phi} \right|^2 \right].$$

This integral is evaluated with the second–order accurate trapezoidal rule. We calculate the phase speed at a given height, z_g, using the values of the phase of $\tilde{\phi}(z_g)$ at the present time step and at the previous one. A first–order backward Euler time scheme then allows us to evaluate $c|^{z_g}$.

Chapter 3

Waves on generalized Eady basic states

3.1 Introduction

This chapter examines the normal mode characteristics of the generalized Eady basic states that have uniform tropospheric and stratospheric quasi–geostrophic pseudo–potential vorticity (QPV), but allow for the decay of density with height. Such basic states contain salient features of the extratropical atmosphere: a vertical wind shear and its associated temperature gradient, and a QPV distribution with gradients concentrated at the tropopause. However, they still lead to tractable and elegant normal mode solutions.

The interest of flows with piecewise uniform QPV (or vorticity in the barotropic case) has long been recognized (Maslowe, 1981). In each region of constant QPV analytical solutions to the normal mode equation (2.26) can be found. Then, appropriate matching conditions at interfaces between regions

lead to normal mode dispersion relations in closed form.

The basic state QPV gradients, Q_y, of generalized Eady basic states are concentrated at the tropopause and ground, where the temperature gradient is equivalent to a thin sheet of infinite Q_y (Bretherton, 1966). Hence the perturbation QPV, $\hat{q}$, is also concentrated at the ground and tropopause [remember (2.29)]. In the potential vorticity perspective put forward in Hoskins et al. (1985), the actors present in the normal mode problem are the eddy perturbation QPV, $\hat{q}$, at the ground and tropopause and their associated circulations that advect the nonzero Q_y present along the two surfaces.

Since the original work of Eady (1949), the Eady problem has become a standard model of baroclinic instability (Pedlosky, 1979; Gill, 1982). Its basic state is a special case of those examined here: the stratospheric stability is infinite, and the shear and density are constant. In the limit of vanishing horizontal scales the two boundary QPV perturbations are independent and the normal mode solutions consist of two edge waves, one at each boundary. At large enough horizontal scales the normal mode wave grows or decays exponentially with time because of the interaction and locking of the two QPV perturbations.

Since 1949, different authors have investigated changes in the Eady normal mode characteristics introduced by a number of physical effects. Eady (1949) himself discussed the effects of a flexible tropopause and of a density decaying with height, while Williams (1974) looked at Eady basic states with height–varying shear and stability. The inclusion of these effects did not markedly

change the wave solutions. Subsequently, Williams and Robinson (1974) studied the effect of adding Ekman friction at the boundaries. The presence of friction at the lower boundary only reduces the instability at large horizontal scales, but destabilizes the upper–level waves and removes the short–wave cutoff.

In this chapter we study waves on generalized Eady basic states because this approach leads to simple upper–level wave solutions of interesting heuristic value. The basic states considered here are more general than the Eady one. First, the rigid lid is replaced by a finite rather than infinite jump in static stability, i.e. a flexible tropopause. Second, the tropospheric stability or shear varies with height and third, the effect of boundary layer friction is considered. In general our normal mode solutions have the same qualitative character as those of the Eady basic state, and the effect of friction is as depicted in Williams and Robinson (1974). Our presentation includes a comprehensive discussion of the upper–level normal modes. Contrary to the general belief (Green, 1960), they have counterparts in linear models with interior positive tropospheric QPV gradients, as will be shown in Chapter 4. It also contains a clear presentation of the effects of a flexible tropopause. Even if mentioned in Eady (1949) and Gill (1983), it is not widely recognized that the Eady normal mode characteristics do not hold only for an unrealistic rigid lid, but also for a realistic tropopause.

In section 3.2 we formulate and solve the problem mathematically. Section 3.3 contains a discussion of the individual edge wave solutions. Section 3.4 and

3.5 display the character of the inviscid and viscid normal modes, and finally we discuss in section 3.6 the significance of our results.

3.2 Formulation

3.2.1 Basic states

Let us assume no meridional gradient of planetary vorticity, $\beta = 0$. In each region we suppose uniform QPV and it follows from (2.10) that

$$\frac{1}{\rho}\frac{d}{dz}\left(\frac{\rho U_{iz}}{N^2}\right) = 0, \text{ for } i = 1, 2, \tag{3.1}$$

where the subscript 1, 2 refers respectively to the troposphere and the stratosphere.

In the stratosphere we pose constant zonal wind and stability,

$$U_2 = \text{ constant}, N_2^2 = \text{ constant}, \text{ for } z > 1.$$

In the troposphere let us express

$$U_{1z}(z) = \exp\left[a(z - \frac{1}{2})\right], \tag{3.2}$$

$$U_1(z) = \frac{1}{a}\left(\exp\left[a(z - \frac{1}{2})\right] - \exp\left[-\frac{a}{2}\right]\right), \tag{3.3}$$

$$\text{and } N_1^2(z) = \exp\left[-b(z-1)\right], \text{ for } z < 1, \tag{3.4}$$

and the constraint of uniform QPV becomes:

$$s - a - b = 0. \tag{3.5}$$

Figure 3.1 displays vertical profiles of $U(z)$ and $N^2(z)$ for different parameter values.

At the tropopause we can write from (2.10):

$$\int_{1-}^{1+} Q_y dz = -\frac{U_z}{N^2}\Big|_{1-}^{1+} = \frac{U_{1z}(1)}{N_1^2(1)}$$

$$\text{and hence : } Q_y = \frac{U_{1z}}{N_1^2}\delta(z-1) = -\frac{\Theta_{1y}}{N_1^2}\delta(z-1).$$

Following Bretherton (1966), we have at the ground:

$$Q_y = -\frac{U_{1z}}{N_1^2}\delta(z) = \frac{\Theta_{1y}}{N_1^2}\delta(z).$$

When the shear is positive in the troposphere, the Q_y distribution of our generalized basic states is identical to that of the Eady one with sheets of positive and negative infinite Q_y at the tropopause and ground. The necessary condition for instability stated in the Charney–Stern theorem is fulfilled. Then, we can calculate the eddy QPV from (2.29):

$$\hat{q}(0) = -\frac{\Theta_{1y}}{N_1^2}\frac{\hat{\psi}}{(U-c)}\delta(z),\ \hat{q}(1) = \frac{\Theta_{1y}}{N_1^2}\frac{\hat{\psi}}{(U-c)}\delta(z-1).$$

Since c generally has a value typical of interior tropospheric wind, positive (negative) $\hat{q}$'s are colocated with negative (positive) $\hat{\psi}$'s.

It is possible to calculate the tropopause height variation with latitude. Let us consider the tropopause as a frontal interface where winds and temperatures are continuous but not their gradients. From Palmen and Newton, 1969, page 170, the slope of the frontal surface must then satisfy:

$$\left(\frac{dz}{dy}\right) = -R_0\varsigma = -R_0\frac{U_{1z}}{(N_2^2 - N_1^2)},\ \text{at } z = 1. \tag{3.6}$$

The decrease of the tropopause height with latitude corresponds to a Rossby number correction. In the limit of infinite stratospheric stability, $N_2^2 \to \infty$, the slope vanishes. Figure 3.2 shows the meridional distribution of isentropes for a particular basic state.

3.2.2 Perturbation equations

In each region the equation for the eddy streamfunction is from (2.26) :

$$\left[\frac{d^2}{dz^2} - a\frac{d}{dz} - \exp\left[-b(z-1)\right]K^2\right]\hat{\psi}_1 = 0, \tag{3.7}$$

$$\left[\frac{d^2}{dz^2} - s\frac{d}{dz} - N_2^2K^2\right]\hat{\psi}_2 = 0. \tag{3.8}$$

It follows from (2.27) that we have as boundary condition at the ground

$$(U_1 - c)\frac{d\hat{\psi}_1}{dz} - U_{1z}\hat{\psi}_1 + i\frac{K^2}{k}\eta_l N_1^2\hat{\psi}_1 = 0 \text{ at } z = 0, \tag{3.9}$$

while as an upper boundary condition we impose

$$\hat{\psi}_2 \text{ bounded as } z \to \infty. \tag{3.10}$$

These equations are completed by matching conditions at the tropopause. Let us introduce a new perturbation field,

$$h'(x', y', t') = R_0 H h(x, y, t),$$

that represents the tropopause deformation associated with the wave. It is a Rossby number correction to the basic state tropopause height, and as in chapter 2 primes refer to dimensional quantities. We consider the tropopause

as a material surface that separates low tropospheric from high stratospheric potential vorticity air. Fluid parcels at the interface stay there; then, the matching conditions are (from Gill, 1982, page 86):

$$\frac{D}{Dt}\left[z + R_0\left(\varsigma y - h\right)\right] = 0, \psi_1 = \psi_2, \text{ at } z = 1 + R_0(h - \varsigma y), \tag{3.11}$$

where D/Dt is the Lagrangian derivative. After linearizing about the basic state, taking the limit $R_0 \to 0$, and considering normal mode solutions, the matching conditions become:

$$\hat{\psi}_1(1) = \hat{\psi}_2(1), \tag{3.12}$$

$$\hat{w}_1(1) = \hat{w}_2(1), \tag{3.13}$$

or, from (2.31):

$$\frac{N_1^2}{N_2^2}(U - c)\frac{d\hat{\psi}_2}{dz} = (U - c)\frac{d\hat{\psi}_1}{dz} - U_{1z}\hat{\psi}_1, \text{ at } z = 1.$$

3.2.3 Perturbation tropopause motion

From (3.11) it is possible to express $\hat{h}$ as:

$$\hat{h} = \frac{(\hat{w} + \varsigma\hat{v})}{ik(U - c)} \text{ at } z = 1, \tag{3.14}$$

or using (2.31), as:

$$\hat{h} = \frac{\varsigma}{(U - c)}\hat{\psi}_2 - \frac{1}{N_2^2}\frac{d\hat{\psi}_2}{dz}, \text{ at } z = 1. \tag{3.15}$$

In the rigid lid limit, $N_2^2 \to \infty$, the perturbation tropopause deformation vanishes since $\hat{w}(1) = \varsigma = 0$. For the waves considered in this chapter, $U(1) - c > 0$

and the streamfunction decays with height in the stratosphere. Therefore, $\hat{h}$ and $\hat{\psi}_2$ are generally correlated, with depressions (anticyclones) having low (high) tropopauses. When the wave is unstable, there is an added phase shift and the tropopause perturbation is located upstream of the streamfunction perturbation. In the context of the linear QG equations this deformation does not feed back on the wave characteristics.

3.2.4 Solutions

We introduce two classes of analytical solutions, S1 and S2, to the system of equations (3.7), (3.8), (3.9),(3.10), (3.12), and (3.13). The S1 solutions have basic states with $a = s$ in (3.2) and $b = 0$ in (3.4): in the troposphere the wind shear increases exponentially with height and the stability remains constant. The basic states of S2 solutions are characterized by $a = 0$ and $b = s$: the tropospheric stability decreases exponentially with height while the shear remains constant. Such stability profiles are representative of the extratropical atmosphere where moist processes lead to temperature lapse rates smaller at lower levels than aloft, as was noted in chapter 1 (remember figure 1.4).

For both S1 and S2 solutions we have in the stratosphere from (3.8) and (3.10) :

$$\hat{\psi}_2(z) = A_2 \exp\left[\left(\frac{s}{2} - \mu_2\right)(z-1)\right],$$
$$\text{where } \mu_2^2 = \alpha_2^2 + \frac{s^2}{4}, \alpha_2^2 = N_2^2 K^2.$$

For S1 solutions we can express the solution in the troposphere as [from

(3.7)]:

$$\begin{aligned}\hat{\psi}_1(z) &= \exp\left(\frac{sz}{2}\right)\left[A_{1c}\cosh(\mu_1 z) + A_{1s}\sinh(\mu_1 z)\right], \\ \text{where } \mu_1^2 &= \alpha_1^2 + \frac{s^2}{4}, \alpha_1^2 = K^2.\end{aligned}$$

For S2 solutions we have:

$$\begin{aligned}\hat{\psi}_1(z) &= A_{1I} I_0\left[\xi(z)\right] + A_{1K} K_0\left[\xi(z)\right], \\ \text{where } \xi(z) &= \frac{2\alpha_{1s}}{s}\exp\left[-\frac{sz}{2}\right], \\ \alpha_{1s}^2 &= \exp(s)K^2,\end{aligned}$$

and I_0, K_0 are modified Bessel functions of the second kind.

Substituting these solutions into the matching and boundary conditions (3.12), (3.13) , and (3.9) leads to a quadratic expression for c:

$$\mathcal{A}c^2 + \mathcal{B}c + \mathcal{C} = 0.$$

For S1 solutions:

$$\begin{aligned}\mathcal{A} &= \mu_1 F_1 - \frac{sG_1}{2} \\ \mathcal{B} &= -\left[U(1)\left(\mu_1 F_1 - \frac{sG_1}{2}\right) + U_{1z}(1)\left(\frac{sS_1}{2} - \mu_1 C_1\right) + G_1\left(U_{1z}(0) - i\frac{\eta_l \alpha_1^2}{k}\right)\right] \\ \mathcal{C} &= \left(U_1(1)G_1 - U_{1z}(1)S_1\right)\left(U_{1z}(0) - i\frac{\eta_l \alpha_1^2}{k}\right),\end{aligned}$$

$$\begin{aligned}\text{where } F_1 &= \left(\mu_2 - \frac{s}{2}\right)\frac{C_1}{N_2^2} + \frac{sC_1}{2} + \mu_1 S_1, \\ G_1 &= \left(\mu_2 - \frac{s}{2}\right)\frac{S_1}{N_2^2} + \frac{sS_1}{2} + \mu_1 C_1,\end{aligned}$$

$$C_1 = \cosh \mu_1, S_1 = \sinh \mu_1.$$

For S2 solutions :

$$\begin{aligned}
\mathcal{A} &= \alpha_{1s}\left[I_{10}V_1 + K_{10}W_1\right] \\
\mathcal{B} &= -\Big[\alpha_{1s}\left(I_{10}V_1 + K_{10}W_1\right) - \alpha_{1s}\left(I_{10}K_{01} + K_{10}I_{01}\right) \\
&\qquad + \left(1 - i\frac{\eta_l \alpha_{1s}^2}{k}\right)\left(I_{00}V_1 - K_{00}W_1\right)\Big] \\
C &= \left(1 - i\frac{\eta_l \alpha_{1s}^2}{k}\right)\left[\left(I_{00}V_1 - K_{00}W_1\right) + \left(K_{00}I_{01} - K_{01}I_{00}\right)\right],
\end{aligned}$$

$$\begin{aligned}
\text{where } V_1 &= \frac{K_{01}}{N_2^2}\left(\mu_2 - \frac{s}{2}\right) + \alpha_{1s}\exp\left[\frac{-s}{2}\right]K_{11}, \\
W_1 &= \frac{I_{01}}{N_2^2}\left(\mu_2 - \frac{s}{2}\right) - \alpha_{1s}\exp\left[\frac{-s}{2}\right]I_{11},
\end{aligned}$$

$$I_{i0} = I_i\left[\xi(0)\right], K_{i0} = K_i\left[\xi(0)\right],$$

$$I_{i1} = I_i\left[\xi(1)\right], K_{it} = K_i\left[\xi(1)\right].$$

This expression for c also determines $\hat{\psi}_1(z)$ through the boundary and matching conditions. The other perturbation fields can be calculated using the formulas presented in section 2.1.3.

3.2.5 Parameter values

We consider in this chapter a channel with $l = 1.4$, i.e. of nondimensional and dimensional widths $L_y = 2.8$ and $L_y' = 2000$ km(from table 2.1). This implies a tropospheric potential temperature change across the channel of

$\triangle\Theta = \Theta_y L_y = 2.8$ (dimensionally $\triangle\Theta' = 18°$ K). The basic state zonal wind maximizes at the tropopause where it is unity (27 m/s). We fix the upper tropospheric stability to unity $N_1^2(1) = 1$ (10^{-4} /s^2) while in most cases $N_2^2 = 4$. When we consider density inhomogeneity in section 3.4, $s = 1$, which corresponds to a density scale height of 9 km. The boundary layer parameter η_l takes values typical of oceanic, flat landmass and mountainous landmass terrains, $\eta_l = 0.04, 0.08, 0.12$, as discussed in Appendix A.

3.3 The inviscid edge wave solutions

We discuss in this section the edge wave solutions that arise in the limit of small horizontal scales. Even if they strictly apply in that limit only, they are interesting because of their simplicity and because their dynamics characterizes a wide range of scales.

In the limit of small horizontal length scales the vertical depth of the perturbation becomes much less than the tropopause height and than the density scale height. Then, the perturbation QPV q's at the ground and tropopause do not "feel" each other via their associated circulation and we have two edge wave solutions, one at each boundary. Mathematically we take the limits

$$s, a, b \to 0 \text{ and } K^2 = k^2 + l^2 >>> 1.$$

Then, after taking the additional inviscid limit, $\eta_l \to 0$, we get for the edge wave at the ground:

$$\hat{\psi}_1(z) = \exp(-Kz), \quad c = \frac{U_{1z}(0)}{K}.$$

A comprehensive discussion of this solution is given in Gill, 1982, pp 550–555.

It is an interesting case of a wave that remains neutral in the presence of available potential energy in the basic state flow. The phase lines of eddy fields are vertical, therefore the wave does not transport heat meridionally and does not grow. It is called a boundary or edge wave since it decays away from the ground. The wave translates with speed c, i.e. with the basic state wind one Rossby height (or an e–folding scale $H_R = 1/K$) above the surface. Low (high) pressure perturbations are colocated with warm (cold) temperature perturbations. The vertical velocity field is 90° ahead of the streamfunction field with upward (downward) motions ahead of low (high) pressure perturbations.

The upper–level edge wave solution is not discussed thoroughly in Gill's book even if mentioned shortly. Taking the same limits as previously, we get an interfacial edge wave solution at the tropopause with:

$$\hat{\psi}_1(z) = \exp K(z-1), \quad \hat{\psi}_2(z) = \exp -N_2 K(z-1),$$

$$c = 1 - \frac{U_{1z}(1)}{K(1+N_2^{-1})}.$$

From (3.15) and (3.6), it is possible to calculate the amplitude of the perturbation tropopause deviation:

$$|\hat{h}| = K\left(\frac{1}{N_2^2 - 1} + \frac{1}{N_2}\right).$$

As shown in figure 3.3, when the stability increases in the stratosphere, the phase speed and the amplitude of the tropopause motion decrease. At $k = 2.3$,

$c = .75$ and $|\hat{h}| = 2.2$ for $N_2^2 = 4$. Using table 2.1, these numbers correspond to a zonal wavelength of 2500 km, to a steering level located at 6.7 km with basic state wind speed of 20 m/s, and to a tropopause deviation of 1.2 km for a perturbation height of 5 dm.

Figure 3.4 displays characteristics of the wave solution at $k = 2.3$. They are very similar to those of the lower–level edge wave. Above the tropopause the relative phase and vertical profiles of most perturbation fields such as streamfunction, temperature, and vertical velocity are the same. Low (high) pressure perturbations have associated warm (cold) temperature perturbations. Below the tropopause the relative phase of the perturbation potential temperature is different, with cold (warm) air embedded in cyclones (anticyclones). In figure 3.4 the vertical velocity does not vanish at the ground since in the limit taken at the beginning of this section, the ground and the tropopause are considered to be much further apart than the depth of the wave. The solution then describes a wave that propagates in presence only of QPV gradient at the tropopause. For an upper–level wave of amplitude .2 at the tropopause (dimensionally 5 dm), the amplitude of the temperature perturbation is of .85 (7 ° K) in the stratosphere and of .55 (4.5 ° K) in the troposphere. The maximum meridional wind speed is then .46 (12 m/s) and the vertical wind speed attains .3 (2 cm/s).

Notice that at the tropopause the potential temperature perturbation is discontinuous. This peculiarity can be explained by looking at the vertical profiles of particle trajectories and of isentropes. For the upper–level edge

wave solution the vertical and meridional velocities are in phase, therefore it is possible to write the particle trajectories in the $y-z$ plane as

$$\left(\frac{\delta z}{\delta y}\right) = R_0 \frac{w}{v},$$

and the isentropic slope is

$$\left(\frac{\delta z}{\delta y}\right)_\theta = -R_0 \frac{\Theta_y}{N^2}.$$

As shown in figure 3.5, the slope of the basic state isentropes changes abruptly at the tropopause. Following the trajectories in the figure, above the tropopause, particles previously warmer than their surroundings find themselves colder than their surroundings. Another way to explain the discontinuous temperature profiles is to examine the thermodynamic equation, (2.5). Above the tropopause the dominant process is adiabatic warming or cooling, whereas below it is advection of basic state potential temperature.

3.4 The total inviscid solutions

Let us now keep the interaction between the two boundary QPV perturbations that was absent in the previous section, and look at the total inviscid solutions. At large enough scales the phase of perturbation fields is no longer vertical and the normal modes can release the available energy of the basic state.

Figures 3.6 to 3.8 display propagation and instability characteristics of the normal modes, and the structure of most unstable modes for four different basic states. Let us first examine the effects of a realistic tropopause on solutions

and concentrate on basic states with constant density. The solid and small dash lines represent respectively the rigid lid limit (the Eady basic state) and a realistic tropopause. As shown in figure 3.6(a) that displays the growth rate ($\Omega = kc_i$), the passage from a lid to a tropopause moves the normal mode instability toward larger scales and decreases the maximum growth rate. The maximum growth rate is reduced by a factor of 1.4, from .2 to .14 (that correspond to e–folding times of 2.0 and 2.7 days), and moves from $k = 1.3$ to $k = 1$, ($L'_x = 4300$ and 5700 km). Also the phase speeds of unstable modes and of neutral upper–level modes generally increase when the tropopause becomes more flexible [see figure 3.6(b)]. The tropopause motion vanishes in the rigid lid limit but is present with a realistic tropopause. As shown in figure 3.7(b), the perturbation tropopause motion moves slightly upstream of the streamfunction wave when the wave grows. The structure of the most unstable mode is also altered with a realistic tropopause: the perturbation streamfunction is less developed at upper level, and the phase lines are more vertical [look at figures 3.8(a) and (b)].

Let us now look at the effects of density stratification that is accompanied by vertical variations of wind U and stability N^2 in the basic states studied here. For that purpose we focus our attention on solutions with basic states that have a realistic tropopause but different profiles of tropospheric stability, wind, and density. The effect of density and shear variations in the S1 solutions tends to decrease the phase speeds of unstable modes and of upper–level neutral modes [compare the long dash and the small dash lines in figure 3.6(b)]. It also causes most unstable modes to be more developed at upper

levels [see figure 3.8(a)]. S2 solutions display only marginal instability at very large horizontal scales [see long dash - short dash line in figure 3.8(a)]; the presence of increased stability close to the ground efficiently stabilizes the flow to normal mode instability.

Figures 3.9 and 3.10 display characteristics of the upper–level normal mode at $k = 2.3$ for the Boussinesq basic state and for the basic state with increased low–level stability. It is interesting to compare figure 3.9 with figure 3.4, which represents the upper–level edge wave solution at the same scale (in the absence of the lower boundary). At upper levels most characteristics of the two solutions, such as the amplitude and phase of different fields, are remarkably similar. The dynamics of the normal mode solution at this scale must then be very similar to that of the edge wave. The presence of the ground however creates secondary extrema in the streamfunction field. As seen in figure 3.9(a), the amplitude at the ground is about one fourth of that at the tropopause. So, for a perturbation amplitude of .2 (5 dm) at the tropopause, a surface pressure perturbation of 1.5 mb is expected. The fields depicted in figure 3.10 are less developed at lower levels than those shown in figure 3.9, because of the increased basic state stability.

3.5 The effect of boundary layer friction

Let us examine here the effect of friction at the lower boundary. Figure 3.11 shows the growth and decay rates of normal modes for four values of the friction

parameter η_l. The presence of friction reduces the instability at large scales, damps very strongly the lower–level wave solutions, and slightly destabilizes the upper–level wave solutions. For $\eta_l = .12$, a value typical of mountainous terrains, the growth rate of the upper–level wave is .005 at $k = 2.3$, which corresponds to a an e–folding time of 80 days; for the lower–level wave, the decay rate is .33, which corresponds to an e-folding time of 1.2 day.

Let us try to understand how the friction at the lower boundary acts on lower–level and upper–level waves. In the formulation presented in section 2.1.2, friction induces convergence and divergence in areas of low and high pressures. Within the QG system this creates adiabatic cooling and warming in low and high pressure areas. Then, the friction tends to destroy lower–level waves that have warm depressions, and slightly destabilizes upper–level ones that have cold depressions. It is interesting to note that this destabilization of upper–level waves does not need the presence of a temperature gradient (or equivalently Q_y) at the ground. Also, it is quite possible that ageostrophic mechanisms, such as latent heat release, may act to reverse the effect of friction at lower levels, since convergence would then induce heating and destabilize the lower–level wave.

Figure 3.12 displays characteristics of the upper–level wave solution at $k = 2.3$ for a friction parameter typical of mountainous landmass. Comparing figures 3.12 and 3.9, we notice that the fields at upper levels are mainly unchanged. At lower levels, there exists upshear tilt in the streamfunction field, while the temperature and vertical velocity fields show downstream tilt.

3.6 Discussion

In this chapter we have shown that the Eady normal mode characteristics hold for realistic tropopause and stratosphere. Let us remember the physical significance of normal mode solutions. The normal modes are the only linear modes of fixed structure; they represent a manner by which perturbation energy within a basic state flow can either be maintained, in the case of neutral modes, or increased, in the case of unstable modes. Note that individual normal modes that have vertical phase lines are also nonlinear solutions of the QG system since both $J(\psi, q)$ and $J(\psi, \theta)$ vanish [remember (2.4) and (2.5)]. This suggests the robustness of neutral normal modes above the short–wave cutoff, and their validity as models for synoptic–scale waves.

It is interesting to compare the structure of upper–level normal modes presented in this chapter with that of observations of midlatitude upper–level waves. Remember chapter 1 where figures 1.2 and 1.3 display characteristics of upper–level waves, extracted from Sanders (1988) and Davis (1990). The upper–level wave solutions depicted in this chapter share many characteristics with the observations: the maximum streamfunction amplitude at the tropopause and the secondary maximum at the ground, the dipole structure in the temperature field, the magnitude of the phase speed, and the relative phase and amplitude of the different perturbation fields. Even the magnitude of the tropopause deformation is comparable. From section 3.3 a height perturbation of 10 dm is associated with a tropopause deviation of 2.4 km, and this compares rather well with observations displayed in figure 1.3, where a

deviation of 2.5 km accompanies a height perturbation of 9 dm. Furthermore the effect of friction at the lower boundary does not damp but slightly destabilizes upper–level wave solutions, and can also explain the low–level upstream tilt present in the observations.

Like the extratropical atmosphere the generalized basic states examined here have profiles of QPV with gradients concentrated at the ground and tropopause, and they lead to elegant normal mode solutions. We think that both the neutral lower–level and upper–level modes are of dynamical significance, and we will show in the next chapter that upper–level modes have counterparts in models with positive tropospheric QPV gradients. The upper–level normal modes share much of the characteristics of observations of upper–level waves in the jet. They provide a simple model for their dynamics, as waves basically supported by the gradient of QPV at the tropopause.

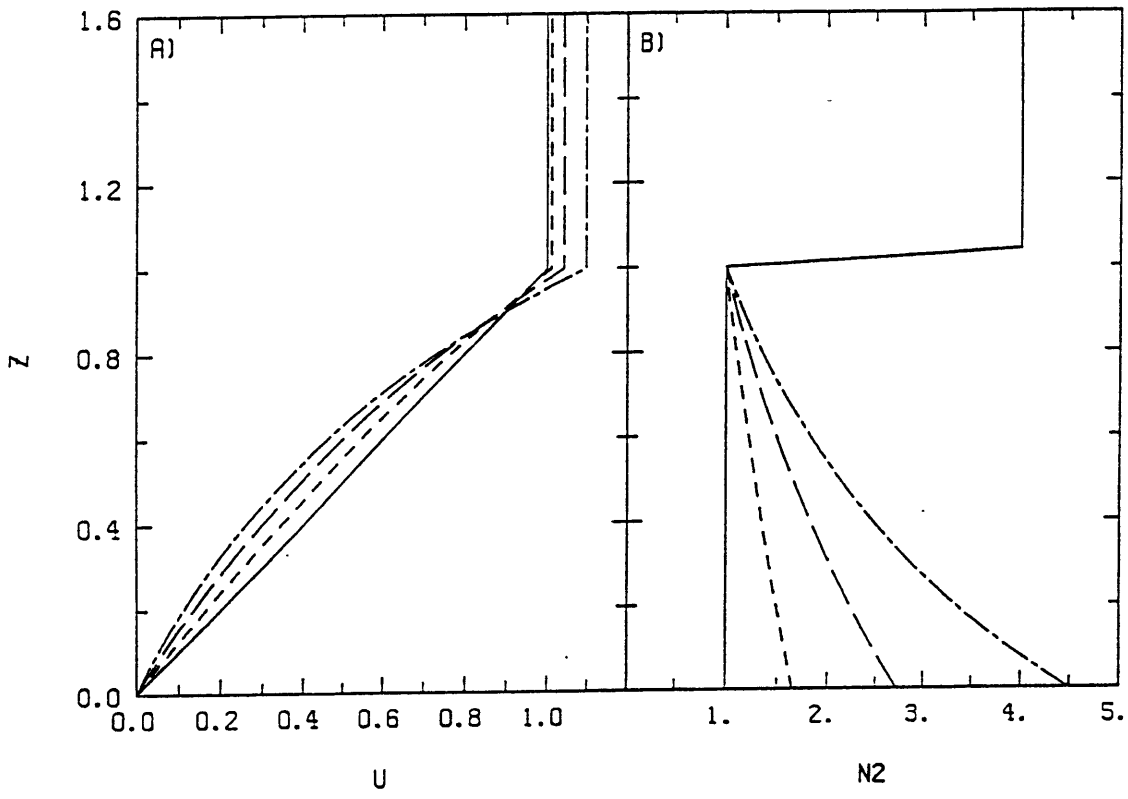

Figure 3.1: The vertical profiles of basic state (a) wind $U(z)$ and (b) static stability $N^2(z)$ with $N_2^2 = 4$ for different values of a and b [$a, b = 0$ (solid line), $a, b = .5$ (short dash line), $a, b = 1$ (long dash line) and $a, b = 1.5$ (long dash - short dash line)].

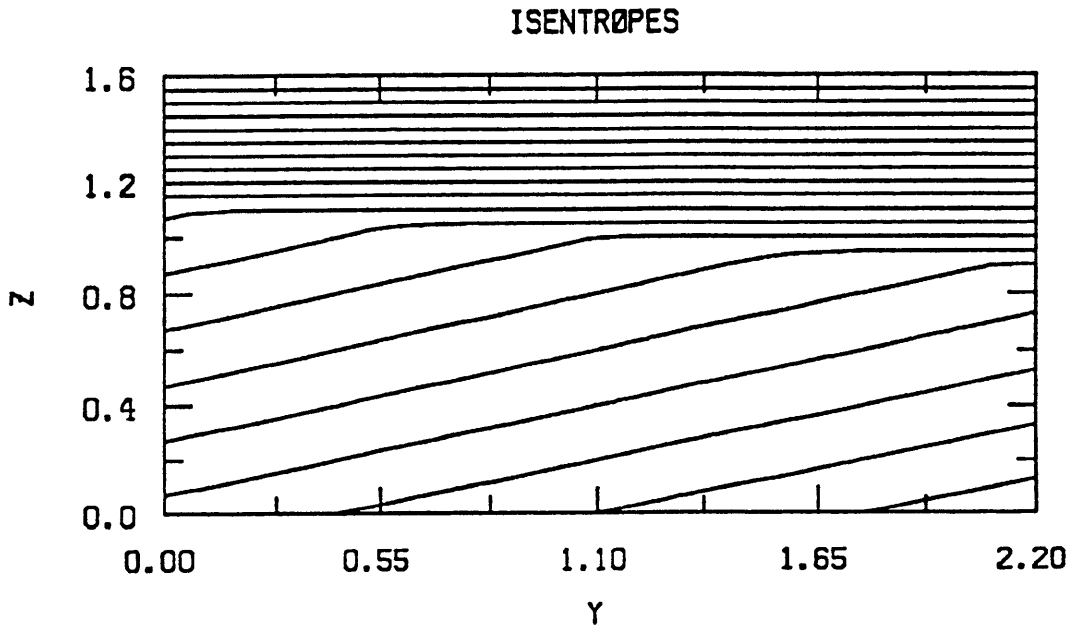

Figure 3.2: Meridional-height cross section of basic state isentropes with $s = a = b = 0$ and $N_2^2 = 4$. The basic state has uniform shear and static stability in the troposphere.

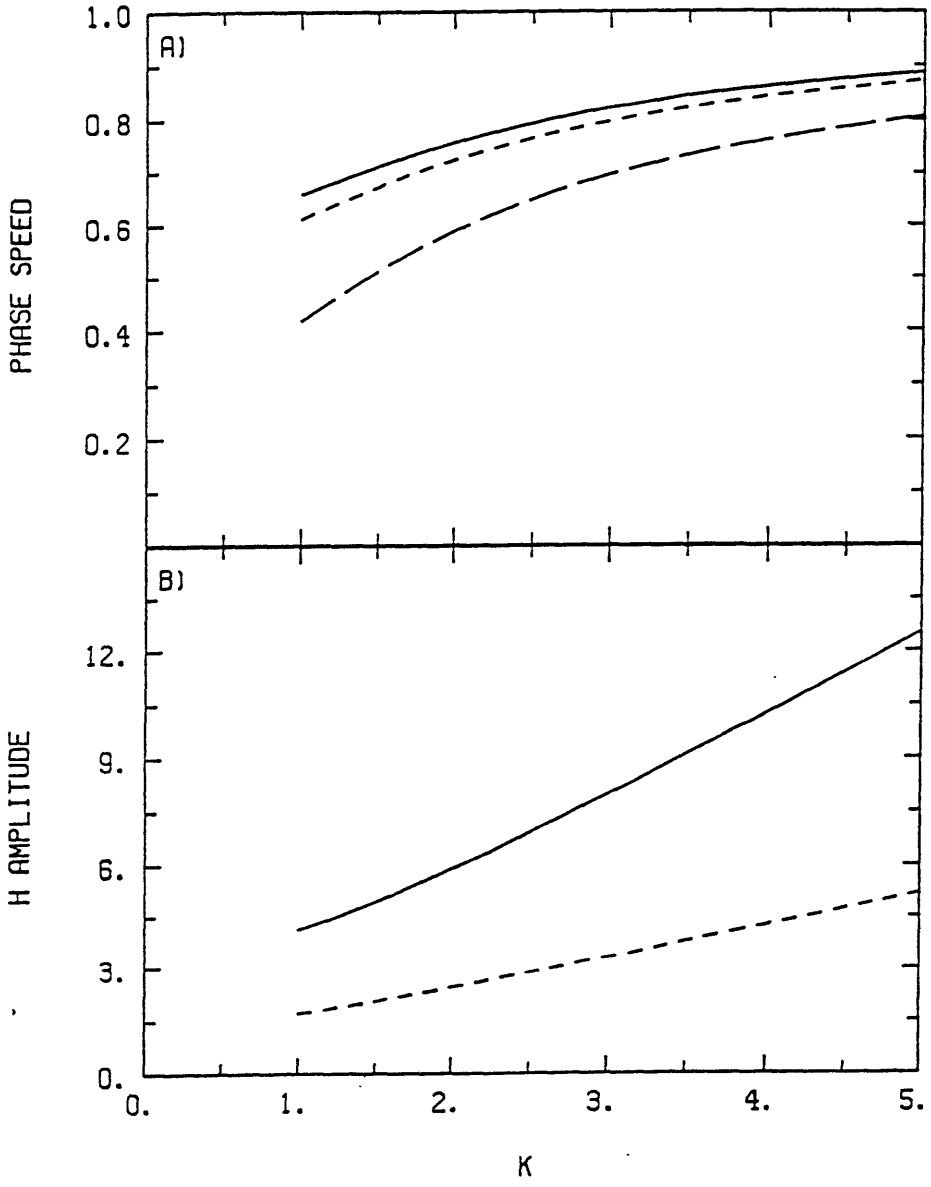

Figure 3.3: (a) Phase speed c and (b) tropopause motion amplitude $|\hat{h}|$ of the upper-level edge wave solutions as a function of k for different values of N_2^2 ($N_2^2 = 2$ (solid line), 4(short dash line), ∞ (long dash line)). The streamfunction amplitude is fixed to unity at the tropopause.

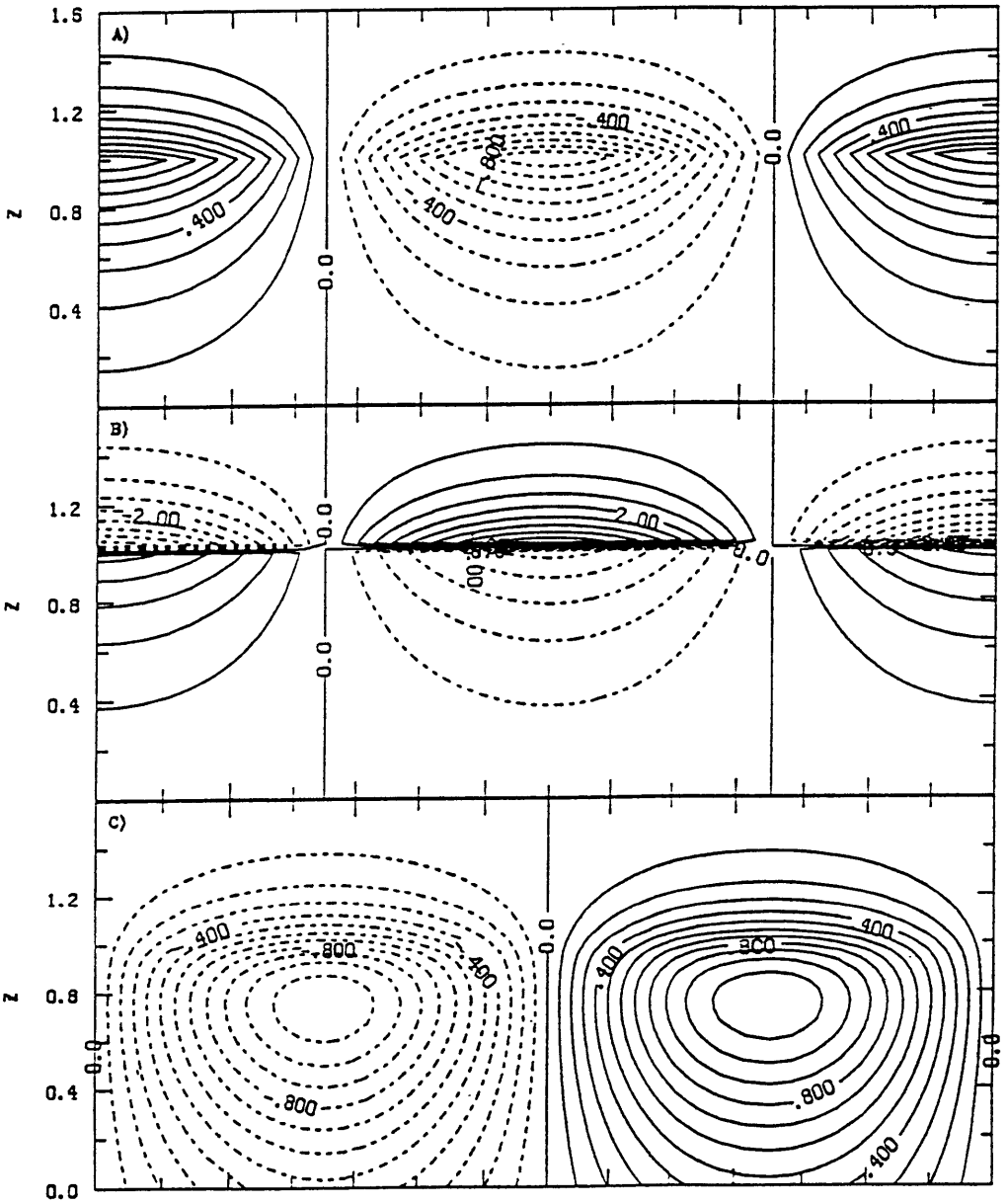

Figure 3.4: Midchannel $x - z$ cross section of the upper-level edge wave at $k = 2.3$ with $N_2^2 = 4$: (a) streamfunction, (b) potential temperature, and (c) vertical velocity. The contour interval is .1 in (a), .5 in (b), and .1 in (c), and the streamfunction amplitude at the tropopause is fixed to unity.

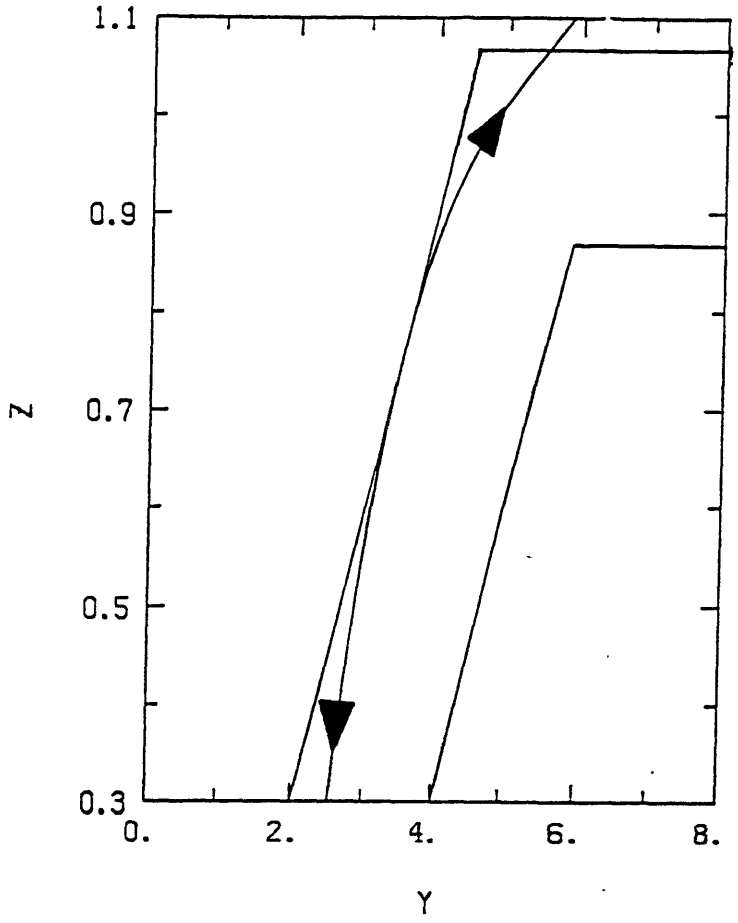

Figure 3.5: Particle trajectory of the upper–level edge wave and basic state isentropes in the $y-z$ plane at $k = 2.3$ with $N_2^2 = 4$. The line with the arrows represents the particle trajectory, while the two other lines are isentropes.

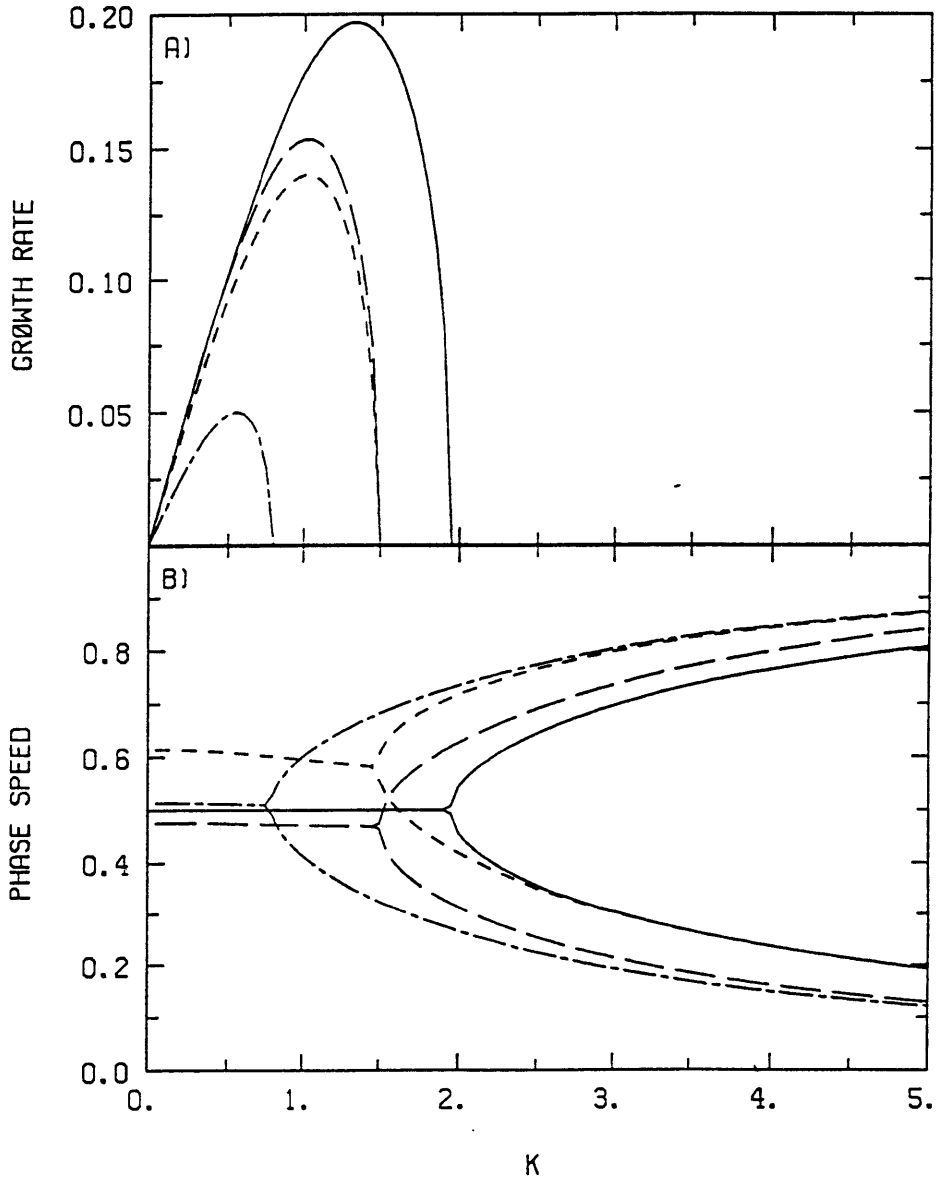

Figure 3.6: (a) Growth rate Ω and (b) phase speed c_r of inviscid solutions as a function of k for four different basic states [(S1,$a = 0$, $N_2^2 \to \infty$) (solid line), (S1,$a = 0$, $N_2^2 = 4$) (small dash line), (S1,$a = 1$, $N_2^2 = 4$) (long dash line), (S2,$b = 1$, $N_2^2 = 4$) (long dash - small dash line)]. The solid line corresponds to the Eady basic state; the small dash line to a Boussinesq basic state with uniform tropospheric shear and stability; the long dash line to a non–Boussinesq basic state with shear varying in the troposphere; and the long dash - short dash line to a non–Boussinesq basic state with the static stability varying in the troposphere.

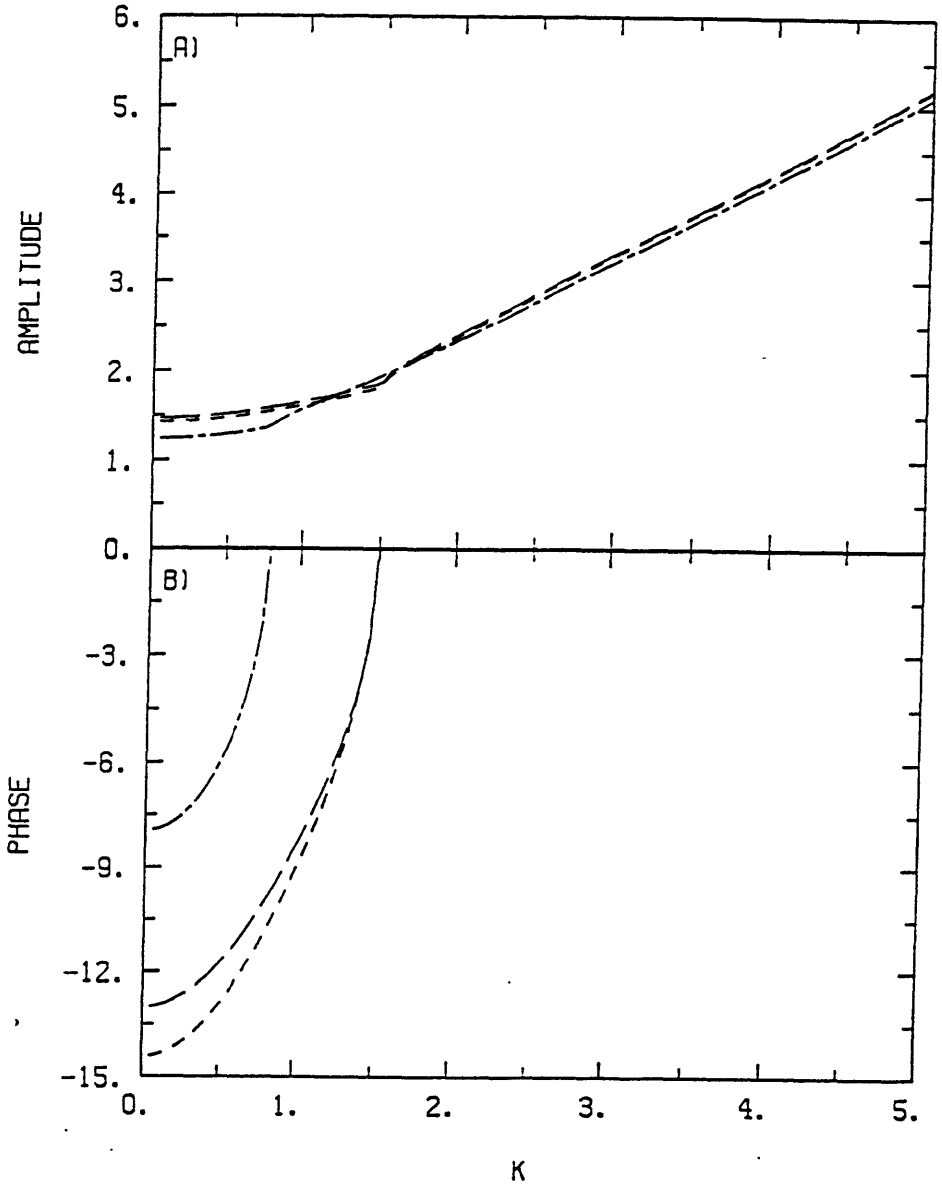

Figure 3.7: The tropopause deviation $\hat{h}$ (a) amplitude and (b) phase of inviscid solutions as a function of k for four basic states represented as in figure 3.6. The streamfunction amplitude at the tropopause is fixed to unity.

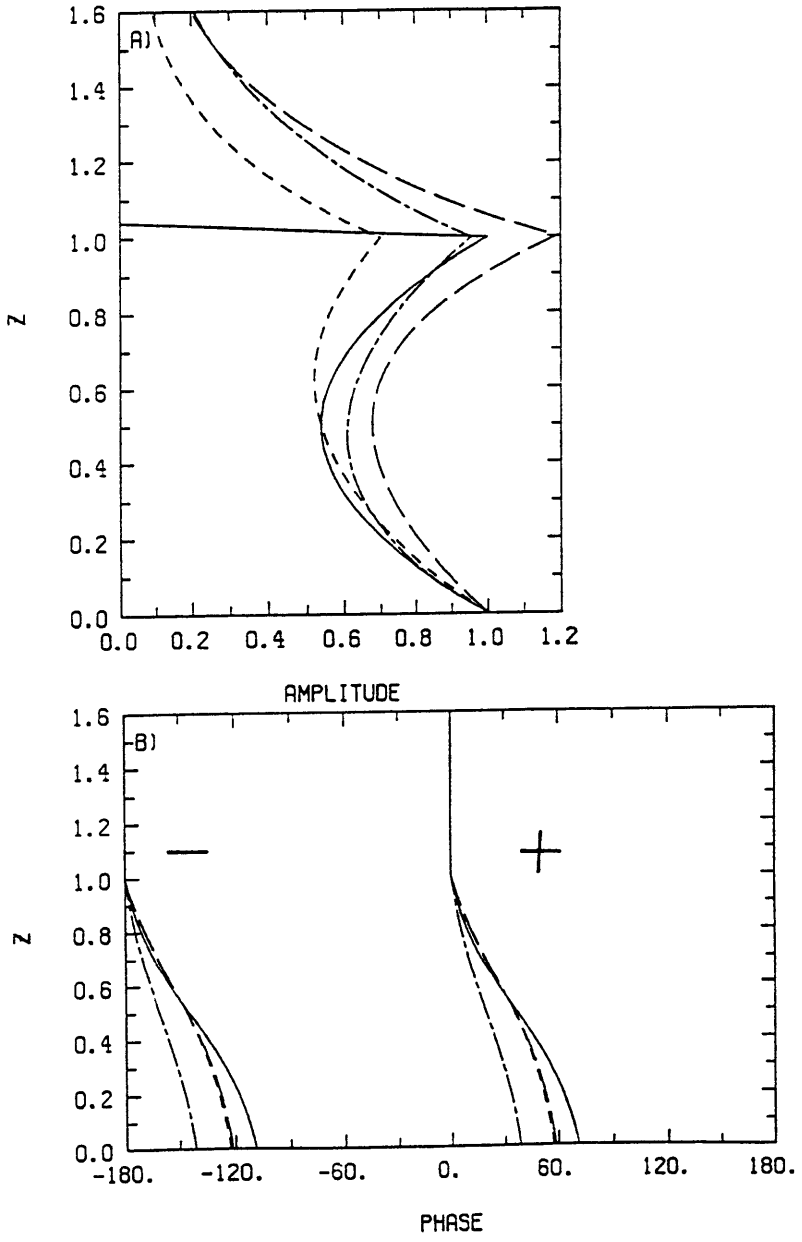

Figure 3.8: The vertical profiles of streamfunction $\hat{\psi}$ (a) amplitude and (b) phase of inviscid solutions most unstable modes for four basic states represented as in figure 3.6. The streamfunction amplitude at the ground is fixed to unity.

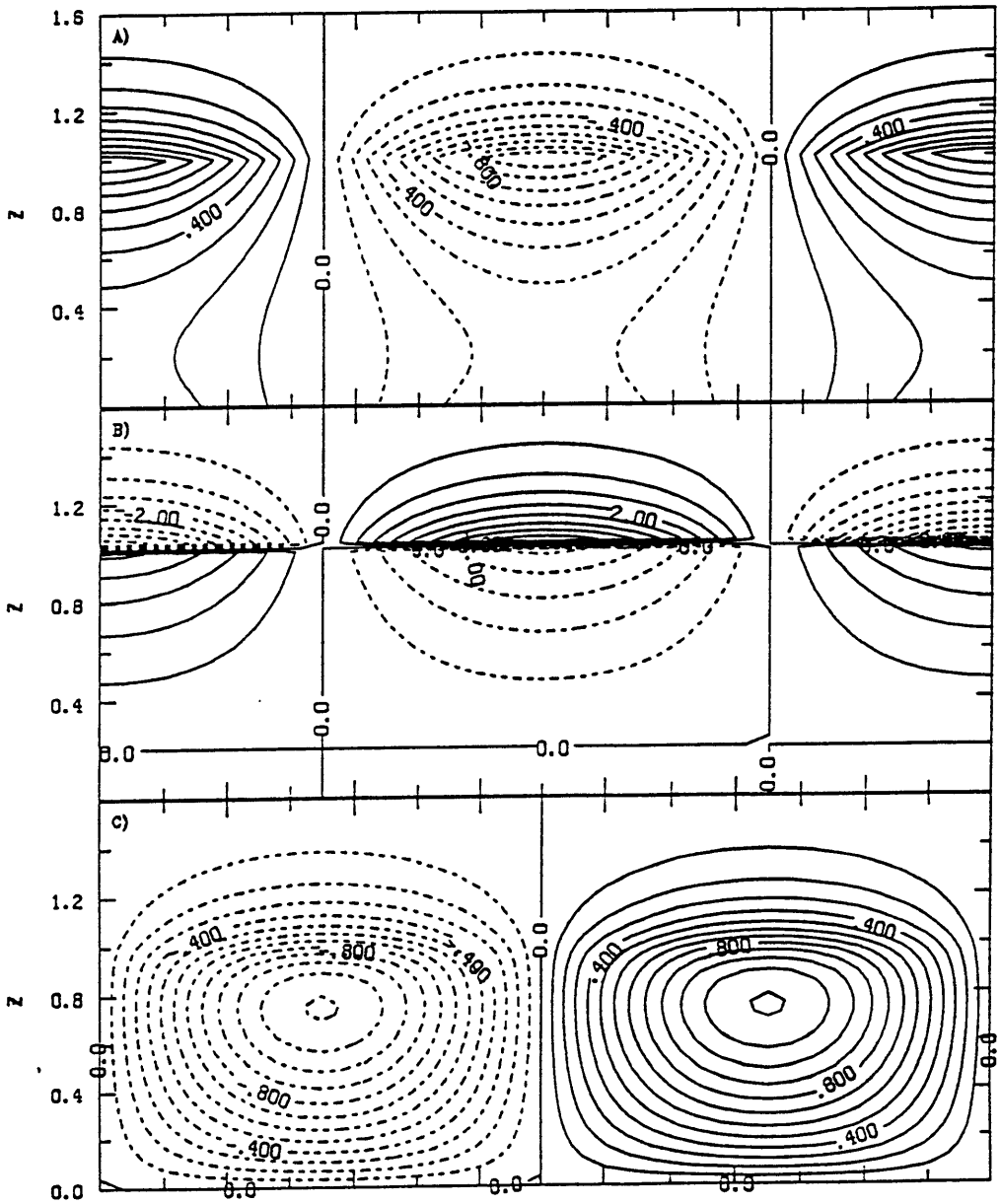

Figure 3.9: Midchannel $x - z$ cross section of the inviscid upper-level wave solution at $k = 2.3$ with $N_2^2 = 4$ for the Boussinesq basic state (S1,a = 0, $N_2^2 = 4$): (a) streamfunction, (b) potential temperature, and (c) vertical velocity. The contour interval is .1 in (a), .5 in (b), and .1 in (c), and the streamfunction amplitude is fixed to unity at the tropopause.

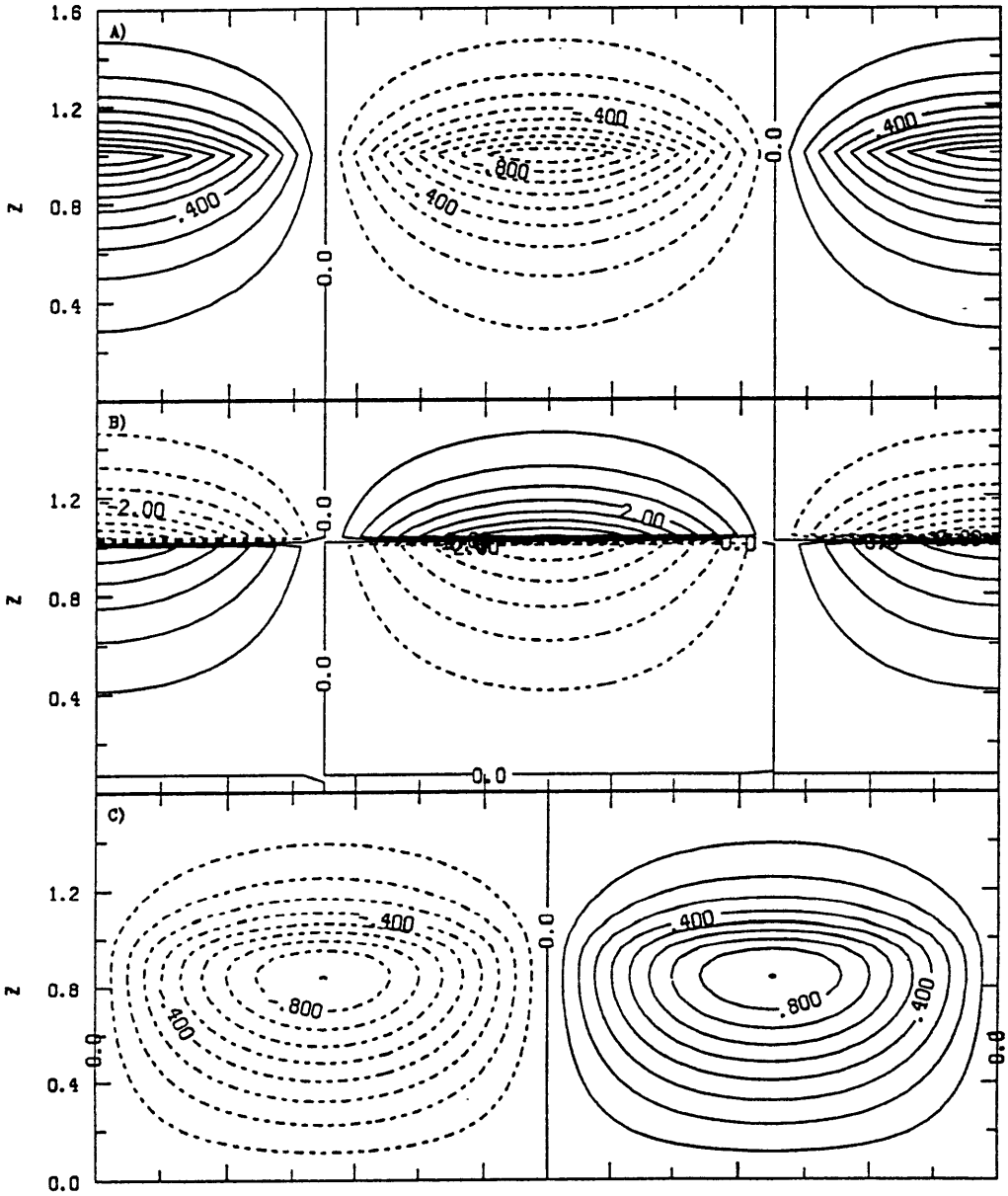

Figure 3.10: Midchannel $x - z$ cross section of the inviscid upper-level wave solution at $k = 2.3$ with $N_2^2 = 4$ for the non-Boussinesq basic state with tropospheric variation of static stability (S2,$b = 1$, $N_2^2 = 4$): (a) streamfunction, (b) potential temperature, and (c) vertical velocity. The contour interval is .1 in (a), .5 in (b), and .1 in (c), and the streamfunction amplitude is fixed to unity at the tropopause.

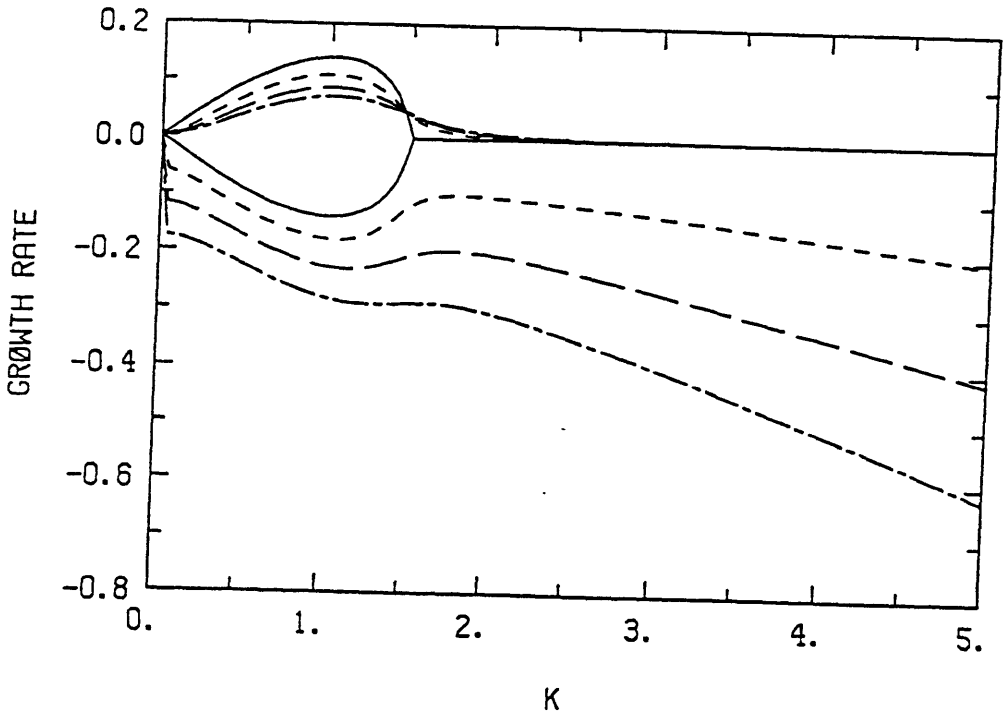

Figure 3.11: Growth and decay rate (kc_i) of viscid solutions as a function of k for the Boussinesq basic state (S1,$a = 0, N_2^2 = 4$) and for different values of η_l ($\eta_l = 0$ (solid line), $\eta_l = 0.04$ (small dash line), $\eta_l = 0.08$ (long dash line), $\eta_l = 0.12$ (small dash - long dash line)).

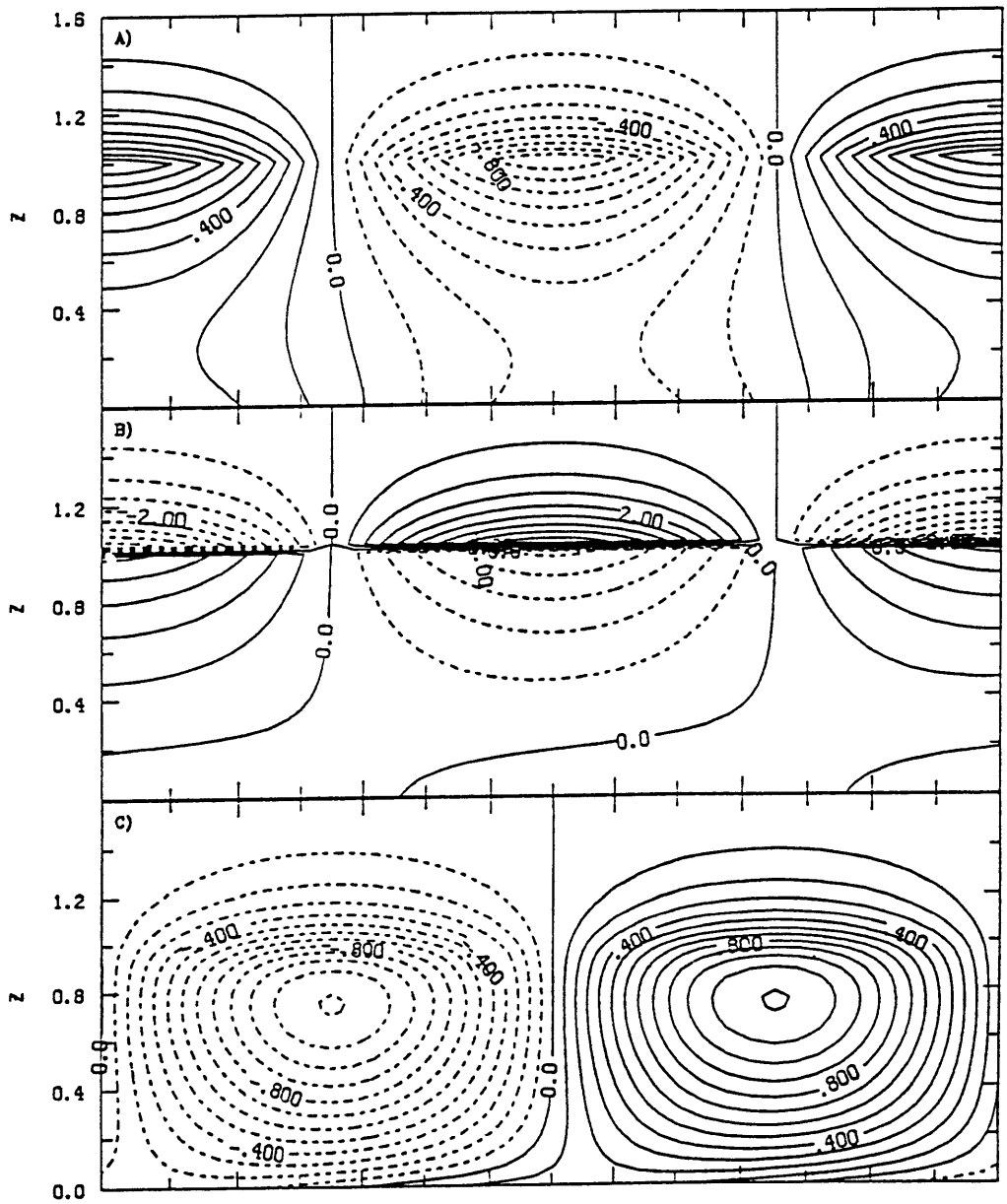

Figure 3.12: Midchannel $x - z$ cross section of the viscid upper-level wave solution at $k = 2.3$ with $N_2^2 = 4$ and $\eta_l = .12$ for the Boussinesq basic state (S1,$a = 0$): (a) streamfunction, (b) potential temperature, and (c) vertical velocity. The contour interval is .1 in (a), .5 in (b), and .1 in (c), and the streamfunction amplitude is fixed to unity at the tropopause.

Chapter 4

Waves on basic states with interior tropospheric potential vorticity gradients

4.1 Introduction

This chapter addresses a question that has been left unanswered in the history of dynamical meteorology. What happens to the upper–level Eady normal modes in the presence of positive basic state gradients of quasi–geostrophic pseudo–potential vorticity (QPV)? Green (1960) examined the effect of a positive meridional QPV gradient on the Eady normal modes, and stated without providing any explanation that the upper–level wave solutions no longer exist. It is the purpose of this chapter to show that the upper–level Eady normal modes have counterparts in models with QPV gradients.

To simplify things as much as possible we consider in this chapter a semi–

infinite domain representative of the troposphere bounded by a rigid lid that corresponds to an infinitely stable stratosphere. Non–Boussinesq effects are not included. We examine in an initial–value problem the evolution of upper–level edge wave solutions in basic state flows identical to the Eady one except that the meridional gradient of planetary vorticity, β, is nonzero. As noted in section 3.2 the temperature gradient at the rigid lid is equivalent to a thin sheet of infinite positive QPV gradient, Q_y. Then, the Q_y distribution is one–signed and positive throughout the domain when the contribution of the lid is included.

For the basic states examined here the Charney–Stern theorem excludes the possibility of unstable normal modes (see section 2.1.3). Furthermore an argument presented by Bretherton (1966) also rules out the existence of neutral normal modes. As stated in the paper neutral modes cannot be supported in monotonic basic state winds with a one–signed Q_y distribution. At the critical level, where the phase speed equals the basic state flow speed, there is then a meridional flux of perturbation QPV, q, that cannot be balanced.

Even in the absence of neutral and unstable normal modes, we show in this chapter that the basic states examined here supports quasi–modes. These quasi–modes consist of a superposition of singular neutral modes with a distribution sharply peaked in the phase speed domain [remember (2.34)]. The decay of the streamfunction does not proceed as $1/t$, as would be the case for a flat distribution (Case,1960). Instead, the streamfunction field, as well as other perturbation fields, display behaviors typical of slowly decaying normal

modes. In the limit $\beta \rightarrow 0$, the distribution becomes a delta of Kronecker and corresponds to a neutral normal mode solution. As β increases from 0, the distribution widens, and the streamfunction amplitude and total perturbation energy decay with time.

We examine in this chapter the parameter dependency of the exponential decay rate of quasi–modes, Λ. The following proportionality relationship holds, $\Lambda \, \alpha \, \beta k/(k^2+l^2)$. Meridionally elongated waves decay faster than zonally elongated waves. This result is consistent with the fact that the meridional QPV gradient, Q_y, is only dynamically active when advected by the meridional wind. The effect of decaying quasi–modes on the mean flow is also studied. In contrast with low–level Charney waves that tend to erase both meridional gradients of surface temperature and interior QPV in the middle of the channel, quasi–modes also act to erase interior QPV gradients, Q_y, but act to enhance temperature gradients at the upper boundary.

In section 4.2 we present the mathematical formulation and solution of the problems addressed in the chapter. Section 4.3 displays the results of a series of initial–value experiments. In section 4.4 the concept of quasi–modes is discussed in details. Section 4.5 presents the effect of quasi–modes on the mean flow, while we discuss in section 4.6 the overall significance of our results.

4.2 Formulation

4.2.1 Basic states

We consider in this chapter a Boussinesq fluid, $s = 0$ and $\rho = 1$, and basic states with linear shear, $U(z) = z$, and constant static stability, $N^2 = 1$. Then, from (2.10) the meridional QPV gradient reduces to the form: $Q_y = \beta$. We assume a semi–infinite domain bounded by an inviscid rigid lid at $z_u = 1$. Figure 4.1 displays the vertical profiles of basic state wind and meridional QPV gradient. Remember from sections 1.2.1 and 2.1.1 that $\beta = .5$ corresponds to an upper bound for midlatitude tropospheric QPV gradients.

4.2.2 Integral equations

Let us present some integral relationships that reveal important aspects of the dynamics studied here. See Pedlosky, 1979, chapter 7, pp.426–440, for details on their derivation. For the type of flows considered in this chapter the meridional eddy flux of QPV has to be balanced by the meridional eddy flux of heat at the boundary:

$$\left(\overline{v\theta}\right|^{z=1} = \int_{-\infty}^{1} dz\, \overline{vq}, \tag{4.1}$$

where the notation is the same as in section 2.1.2. This relation allowed Bretherton (1966) to develop his argument for the nonexistence of neutral modes. The left–hand side (LHS) of (4.1) can be rewritten as

$$\left(\overline{v\theta}\right|^{z=1} = \frac{\partial}{\partial t}\left(\overline{\zeta^2/2}\right|^{z=1}, \tag{4.2}$$

where ζ represents the meridional displacement, while in the case of neutral modes propagating with phase speed c, we can express the right–hand side (RHS) as

$$\begin{aligned}\int_{-\infty}^{1} dz\, \overline{vq} &= -\beta \int_{z_c-}^{z_c+} dz\, \frac{\partial}{\partial t}\left(\overline{\zeta^2/2}\right), \\ &= -\beta\pi k \left(\frac{\overline{\psi^2}}{U_z}\right|^{z=z_c}, \end{aligned} \tag{4.3}$$

where z_c is the height of the critical level, $U(z_c) = c$. To obtain (4.3) we took the physical limit of viscosity going to zero from positive values. Comparing (4.2) and (4.3) we understand that in the case of a neutral mode there is a QPV flux at the critical level that cannot be balanced because the temperature flux at the boundary vanishes.

In section 4.5 of this chapter we examine the effect of decaying quasi–modes on the mean flow, where the mean refers to the zonal average. We more specifically look at the temperature gradient at the upper boundary, $\overline{\Theta}_y(y, z = 1, t)$, and at the vertical profiles of meridional QPV gradient, $\overline{Q}_y(y, z, t)$. These two relations hold:

$$\frac{\partial \left(\overline{\Theta}_y\right|^{z=1}}{\partial t} = -l^2 RE \left[\left(\tilde{v}\tilde{\theta}^*\right|^{z=1}\right] \cos 2ly, \tag{4.4}$$

$$\frac{\partial \overline{Q}_y}{\partial t} = -l^2 RE \left[\tilde{v}\tilde{q}^*\right] \cos 2ly. \tag{4.5}$$

From (4.1) we must also have

$$\frac{\partial \left(\overline{\Theta}_y\right|^{z=1}}{\partial t} = \int_{-\infty}^{1} dz\, \frac{\partial \overline{Q}_y}{\partial t}.$$

When the wave transports heat southward at the upper boundary, $RE\left[\left(\tilde{v}\tilde{\theta}^*\right|^{z=1}\right] < 0$, the magnitude of the temperature gradient (that is nega-

tive) increases in the middle of the channel and decreases on its sides. When the wave transports QPV southward, $RE\,[\tilde{v}\tilde{q}^*] < 0$, the gradient $\overline{Q}_y$ is enhanced at the sides of the channel, but erased in its middle.

4.2.3 The decay rate in the normal mode limit

From (4.1), (4.2), and (4.3), we can calculate an approximate expression for the decay of upper–level edge waves in the normal mode limit where the QPV flux is nonzero at the critical level only. As noted in Tung (1983), the normal mode limit is never reached in an initial–value experiment with nonsingular initial conditions. However, it is interesting to compare this approximate normal mode limit with the decay rate associated with initial–value experiments.

Let us approximate the streamfunction field as

$$\tilde{\psi}(z,t) \cong \hat{\psi}_E(z) e^{-\Lambda_n t} e^{ikc_E t},$$

where Λ_n is the decay rate in the normal mode limit, and $\hat{\psi}_E(z)$ and c_E are respectively the streamfunction field and phase speed associated with the upper–level edge wave solution,

$$\hat{\psi}_E(z) = \exp[K(z-1)],\ c_E = 1 - 1/K, \tag{4.6}$$

(see section 3.3). Then, through (4.2), the LHS of (4.1) can be approximate as

$$\left(\overline{v\theta}\right|^{z=1} \cong -\frac{\Lambda_n}{2} \frac{\left(|\hat{\psi}_E|^2\right|^{z=1}}{(1-c_E)^2} \sin^2 ly = -\frac{\Lambda_n}{2(1-c_E)^2} \sin^2 ly,$$

since $\hat{\zeta} = \frac{\hat{\psi}}{(U-c)}$, while the RHS reduces to

$$\int_{-\infty}^{1} dz\, \overline{vq} \cong -\frac{\beta\pi k}{2e^2} \sin^2 ly.$$

These lead to a decay rate,

$$\Lambda_n = \frac{\beta\pi k}{e^2(k^2+l^2)} = .42\frac{\beta k}{k^2+l^2}. \tag{4.7}$$

4.2.4 Solution to the initial–value problem

In this chapter we solve the initial–value problem that consists of integrating in time (2.15), completed by (2.17), by an inviscid rigid lid boundary condition at $z_u = 1$, [$\eta_u = 0$ in (2.22)], and by an approximate boundary condition for trapped waves at $z = z_l$ [(B.12) in Appendix B]. We solve this problem numerically, and the details of the initial–value model are presented in section 2.2.3. It is fourth–order accurate in height and second–order in time. For most simulations the time step is fixed to $\Delta t = .05$ and the vertical resolution to $\Delta z = .025$, and the fictitious lower boundary is located at $z_l = 0$. We test the validity of the results by performing experiments with finer height and time resolutions, and with a fictitious lower boundary that we move to smaller height, $z_l < 0$.

The initial condition consists of the inviscid upper–level wave solution for $\beta = 0$. We did not use the analytical formula (4.6) to compute the initial condition at grid points. Instead, we computed the vertical structure of this eigenmode numerically with a technique presented in section 2.2.1, in which the vertical scheme is the same as the one used to solve the initial–value problem.

The advantage of this approach is that it produces an initial condition that is a numerical mode of the vertical scheme.

In the initial–value experiments we look at a number of diagnostics. We produce time series of scalar diagnostics that are computed at each time step. This is the case for the streamfunction amplitude at the lid, the total perturbation energy [remember (2.23)], and the phase speed at the lid, $|\tilde{\psi}|^{z=1}$, E_T, and $c|^{z=1}$. Also at specified times, we examine perturbation fields of streamfunction, QPV, temperature, and vertical velocity. We also compute changes in $\overline{\Theta}_y$ and $\overline{Q}_y$ induced by the wave. (4.4) and (4.5) are integrated in time during the simulation to produce a time series of $\Delta\left(\overline{\Theta}_y\right|^{z=1}(t)$, and also the vertical profiles of $\Delta\overline{Q}_y(z)$ at specified times. Details of computations of the diagnostics can be found in section 2.2.3.

4.2.5 Modal decomposition

In section 4.4 we calculate the singular modes [remember (2.32)] associated with the basic states examined here. The modes $|\psi_j>$ and $|\psi_j^a>$ are computed numerically with a technique described in section 2.2.2. The solution to the initial–value problem can then be expressed as in (2.34):

$$|\psi(t)> \;=\; \sum_{j=1}^{N} a_j|\psi_j> e^{-ikc_jt},$$

$$\text{where } a_j \;=\; \frac{<\psi_j^a|\psi_E>}{<\psi_j^a|\psi_j>},$$

and where $|\psi_E>$ represents the upper–level wave solution at a certain truncation. In this chapter we are interested specifically at the time evolution of

the streamfunction amplitude at the lid:

$$\begin{aligned} |\psi(1,t)> &= \sum_{j=1}^{N} F_j e^{-ikc_j t}, \\ \text{where } F_j &= a_j |\psi_j(1)> . \end{aligned} \tag{4.8}$$

In section 4.4 we examine idealized distributions F_j that lead to analytical solution to (4.8). We also look at distributions F_j for a number of initial–value experiments performed in section 4.3.

4.3 Initial–value experiments

We perform in this section a series of initial–value experiments with the initial condition consisting of the upper–level edge wave solution for $\beta = 0$. We vary the three free parameters, β, k, and l, in order to find the parameter dependency of the decay rate and propagation speed of quasi–modes.

4.3.1 Varying β

We vary β but keep k and l constant: $k = 2.3$, $l = 1.4$. Figure 4.2 displays the time series of $|\tilde{\psi}|^{z=1}$, $c|^{z=1}$, and E_T for five different experiments. When $\beta = 0$ (solid line), the streamfunction amplitude at the lid and the perturbation total energy remain constant, while the mode propagates at a fixed rate, $c = .6292$ (which is close to the analytical value $c = .6286$). As β increases, the streamfunction amplitude at the lid decays in time with an exponential behavior (notice the straight lines on log–linear plots). The total perturbation

energy evolves similarly but the decay proceeds at a faster rate. Small oscillations around that exponential behavior are visible especially at $\beta = 1$ (long dash - short dash - short dash line). The propagation speed at the lid lowers as β increases, and oscillates in time when β becomes large, i.e. at $\beta = .75$ and $\beta = 1$.

In figure 4.3 we show the time evolution of perturbation fields of streamfunction and QPV for $\beta = .5$. At the initial time, the eddy QPV is null in the interior, which is a characteristic of the upper–level edge wave solution. As time marches, the eddy QPV is both generated by the advection of β by the meridional wind and sheared by the basic state wind [remember (2.15)]. It maximizes in the critical region where the flow speed equals the "phase speed", i.e. around $z = .6$ $[c|^{z=1} \cong .58$ from figure 4.2(b)]. The streamfunction displays slight downstream tilt that becomes more and mode localized around the critical region as time progresses.

Figures 4.4 display perturbation fields $\tilde{\psi}$, $\tilde{q}$, $\tilde{\theta}$, and $\tilde{w}$, for $\beta = .5$ at time=10. It is interesting to compare this figure with figure 4.5 that exhibits the same perturbation fields with the same parameters, but for the lower–level Charney normal mode. The lower–level mode propagates at a phase speed, $c_r = .328$, and grows at a fixed rate, $\Omega = kc_i = .064$. It was calculated numerically using the technique presented in section 2.2.1. The streamfunction and vertical velocity fields display upstream tilt with height, which is indicative of a growing mode, while the QPV field shows large downstream tilt around the critical level where it sharply peaks. The perturbation fields of the initial–value experiment

are oppositely tilted, with the streamfunction and vertical velocity leaning downshear, but the QPV field still shows downshear tilt in the critical region where it maximizes.

Even if the perturbation fields of initial–value experiments, especially QPV and temperature, do not have fixed structure, decay rate, and phase speed, they show a lot of behaviors typical of modes. The streamfunction field keeps a distinct maximum at the lid, which propagate at a fairly steady rate for small β. As the Charney modes that become lower–level Eady modes in the limit of $s, \beta \rightarrow 0$, they can be thought of as quasi–modes that reduce to upper–level Eady modes. This concept will be clarified in section 4.4.

4.3.2 Varying k and l

We examine the evolution of the initial–value problem varying k, but keeping β and $(k^2 + l^2)$ constant : $\beta = .5$ and $(k^2 + l^2) = 7.25$. Figure 4.6 shows time series of $|\tilde{\psi}|^{z=1}$, E_T, and $c|^{z=1}$ for five different experiments. As k increases, both the streamfunction at the lid and the total perturbation energy decay at faster rates. However, changes in k do not affect the propagation speed at the lid.

We also study the initial–value problem, varying k and l, but keeping β and $\beta k/(k^2 + l^2)$ constant: $\beta = .5$ and $\beta k/(k^2 + l^2) = .159$. As shown in figures 4.7(a) and (c), the decay of the streamfunction at the lid and of the total perturbation energy proceeds at the same rate for the three experiments.

However the propagation speed at the lid decreases as $(k^2 + l^2)$ decreases.

The results presented so far suggest the parameter dependencies for the decay rate, $\Lambda = g(\beta k/(k^2 + l^2))$, and for the propagation speed change, $\Delta c|^{z=1} = f(\beta, (k^2 + l^2))$, where $\Delta c|^{z=1}$ is the propagation speed at the lid minus that of the original edge wave solution.

4.3.3 The decay rate and the propagation speed change

We present here approximate expressions for the decay rate and the propagation speed change that can be inferred from initial–value experiments. We are interested in the decay rate of the streamfunction amplitude at the lid and in the propagation speed at the lid. Since the amplitude of perturbation streamfunction maximizes at the lid, we think it is a proper way to characterize the quasi–modes.

Let us first evaluate the decay rate Λ,

$$|\tilde{\psi}|^{z=1} = |\tilde{\psi}|^{z=1,t=0} e^{-\Lambda t}.$$

In initial–value experiments we evaluate Λ from the decay that occurs between time=4 and 20:

$$\Lambda = -\frac{1}{16} \ln \left(\frac{|\tilde{\psi}|^{z=1,t=20}}{|\tilde{\psi}|^{z=1,t=4}} \right).$$

Figures 4.8 (a) and (b) show that the decay rate depends linearly with β and k. A linear regression on the five points of figure 4.8 (a) leads to the relation:

$$\Lambda = .45 \frac{\beta k}{(k^2 + l^2)}, \tag{4.9}$$

where the correlation coefficient is greater than .999. A regression on the five points of figure 4.8(b) leads to the same result within one percent. The relationship (4.9) holds for the parameter range explored in initial–value experiments: $0 < \beta < 1$, $0 < k < 2.5$, and $4.7 < (k^2 + l^2) < 7.3$. It is interesting to compare this rate with the approximate decay rate in the normal mode limit, Λ_n, evaluated in (4.7). The approximation derived in section 4.2.3 does very well: the parameter dependency is the same and the rate is slightly smaller than the rate of initial–value experiments. The initial–value experiments show that nothing singular happens at the critical level even if a maximum of $|\tilde{q}|$ is generated in the region. This small discrepancy is therefore not surprising.

Now we evaluate the change in propagation speed at the lid. It is obvious in the initial–value experiments that the propagation speed at the lid fluctuates with time, especially at large horizontal scales, i.e. small (k^2+l^2), and large β. We solve this problem by calculating average of $c|^{z=1}$ from time=4 to 20 for each experiment. We then compute $\triangle c|^{z=1}$ by subtracting from the average the numerical value of the phase speed of the edge wave solution, $c = .6292$. Figure 4.9 displays the dependency of $\triangle c|^{z=1}$ with respect to β. A linear regression using the five points of figure 4.9 yields the relation:

$$\triangle\, c|^{z=1} = -.105\beta. \tag{4.10}$$

where the correlation coefficient is greater than .999. The linear relation (4.10) is valid in the parameter range $0 < \beta < 1$, $0 < k < 2.5$, and $(k^2 + l^2) = 7.25$.

In the extratropical atmosphere a realistic upper bound for tropospheric Q_y corresponds to $\beta = .5$. For $k = 2.3$ and $l = 1.4$, which correspond to

a channel width of 2000 km and a zonal wavelength of 2500 km, the streamfunction amplitude at the lid decays by an exponential factor in $t_d = \Lambda^{-1}$, 14 time units (dimensionally 5.5 days), and the propagation speed is $c|^{z=1} = .58$ (dimensionally 15.6 m/s).

4.4 Propagating quasi–modes in shear

In this section we clarify the mathematical definition of quasi–modes. Neither neutral nor unstable modes are supported by the basic states studied in this chapter. However, they support decaying quasi–modes that consist of a superposition of singular modes sharply peaked in the phase speed domain.

Let us examine two distributions F_j that lead to analytical solutions to (4.8). First, we study a case with uniform F_j,

$$\begin{aligned} F_j &= 1 \text{ in the domain } [c_1, c_2], \\ &= 0 \text{ elsewhere.} \end{aligned}$$

Then, changing the summation for an integral in (4.8) yields

$$\begin{aligned} |\psi(1,t)> &= \int_{c_1}^{c_2} dc\, e^{-ikct}, \\ &= \frac{2}{kt} \exp\left[-ik\left(\frac{c_1+c_2}{2}\right)t\right] \sin k\left(\frac{c_2-c_1}{2}\right)t. \end{aligned}$$

The streamfunction decays as $1/t$, and this result is consistent with the more general results presented in Case (1960).

Let F_j take the following form,

$$F_j = \frac{\mathcal{K}}{(c_j - c_0)^2 + w^2}, \tag{4.11}$$

where c_0 is the location of the peak and w the half–width. After changing the summation to an integral in (4.8), and assuming that F_j has significant values only in the range of phase speeds supported by the basic state, we arrive at the expression,

$$|\psi(1,t)>= \int_{-\infty}^{\infty} dc \frac{\mathcal{K} e^{-ikct}}{(c - c_0)^2 + w^2}.$$

A change of variable, $c' = c - c_0$, yields

$$\begin{aligned} |\psi(1,t)> &= \mathcal{K} e^{-ikc_0 t} \int_{-\infty}^{\infty} dc' \frac{e^{-ikc't}}{c'^2 + w^2} \\ &= \frac{\mathcal{K}\pi}{w} e^{-ikc_0 t} e^{-wkt}. \end{aligned}$$

The streamfunction wave at the lid propagates with speed c_0 and decays exponentially at a rate, $\Lambda = wk$. The decay proceeds as the singular modes interfere with one another.

These two examples can help to clarify the concept of a quasi–mode, as a sharply peaked distribution of singular modes. When the distribution is sharply peaked, the decay of the streamfunction does not happen as $1/t$, thus depending only on the shear, but proceeds at a rate determined by the width of the peak. Quasi–modes behave essentially as slowly decaying modes.

Figure 4.10 displays the distribution F_j for an initial–value experiment with $\beta = .25$ (solid line), and F_j calculated from expression (4.11) (dash line). In (4.11) the parameters are fixed by the results of initial–value experiments

presented in section 4.3. From these the decay rate, Λ, and the propagation speed change, $\triangle c|^{z=1}$, are known. We can then compute c_0 by adding $\triangle c|^{z=1}$ to the phase speed of the original edge wave solution, .6292, and w with the expression $w = \Lambda/k$. The two distributions are remarkably similar. It is therefore not surprising that initial–value experiments display the exponential decay of the streamfunction at the lid (remember figure 4.2, the dash line corresponds to the case illustrated in figure 4.10).

Figure 4.11 displays the distributions F_j for different values of β. When $\beta = 0$, the distribution is simply a delta of Kronecker (solid line). As β increases, the distribution F_j widens, and its peak moves toward smaller phase speeds. Notice that it also becomes more asymmetrical with respect to the peak, with amplitudes larger on the side of larger phase speeds.

4.5 Wave–mean flow interaction

We examine in this section the effect of decaying quasi–modes on the mean flow. Figure 4.12 depicts changes in the midchannel mean temperature gradient at the lid induced by quasi–modes for initial–value experiments with parameters as in figure 4.2. Each curve represents a different value of β: $\beta = .25, .5, .75, 1.$, while k and l are fixed to 2.3 and 1.4. The magnitude of the midchannel mean temperature gradient at the lid increases as quasi–modes decay. This enhancement proceeds at a rate that increases as β increases. Remember that it is accompanied by a reduction of the gradient on the sides

of the channel [see (4.4)].

We show in figure 4.13 changes in the midchannel mean QPV gradient for initial–value experiments with $\beta = .5$ and $\beta = 1$. Each curve refers to a different time in the simulation. The large numbers present in the abscissae of figure 4.13 are due to the fact that in the initial–value experiments the initial streamfunction amplitude at the lid is fixed to unity (this is also the case in figure 4.12). For both cases, the quasi–mode acts to erase basic state QPV gradients that are positive. As time progresses, changes peak in the critical region. When $\beta = 1$, changes do not become as sharply peaked as when $\beta = .5$. The quasi–mode simultaneously induces an increase in the mean QPV gradient on the sides of the channel [remember (4.5)].

It is interesting to evaluate a time scale for the erasing of the interior QPV gradient by upper–level waves. Let us consider here realistic values for the parameters and for the perturbation amplitude. To calculate a time scale we consider an initial perturbation amplitude of $|\tilde{\psi}|^{z=1,t=0} = .2$, $\beta = .5$, $k = 2.3$ and $l = 1.4$. These numbers correspond to an initial perturbation of 5 dm and 12 m/s at the tropopause, with a zonal wavelength of 2500 km and a channel width of 2000 km. For these parameter values, from figure 4.13(a), the midchannel mean QPV gradients in the critical region are erased after 8 time units (dimensionally 3.1 days). This is accompanied by a doubling in the mean QPV gradient on the sides of the channel. Also, from figure 4.12 (the large dash line represents the case with $\beta = .5$), the mean temperature gradient at the lid is then increased by a fifth in the middle of the channel,

and decreased by a same amount on the sides.

4.6 Discussion

In this chapter we showed that the upper–level Eady normal modes have counterparts as decaying quasi–modes in models with interior tropospheric QPV gradients. The quasi–modes consist of a distribution of singular modes sharply peaked in the phase speed domain, and their decay proceeds as the singular modes present interfere with one another. The concept of quasi–modes is important since quasi–modes represent a manner by which perturbation energy can be maintained in shear flows, not for an infinite time like neutral normal modes, but for a considerable time. Stationary quasi–modes in shear flows have been discussed previously in Held et al. (1985). This chapter presented the first study on propagating quasi–modes.

For parameter values typical of synoptic–scale waves at midlatitudes and for a realistic upper bound of tropospheric QPV gradients, the quasi–modes were found to have marginal decay rates that correspond to exponential decay times of six days. Furthermore, our results showed that quasi–modes act to erase the critical region mean QPV gradients after three days, thus enhancing the mean temperature gradient at the lid. Their net effect is to create a mean flow that supports them. These results suggest that perturbation energy can indeed be maintained at the tropopause even in the presence of initial interior tropospheric QPV gradients. Sanders (1988) found that the life duration of

upper–level mobile troughs at midlatitudes is typically 12 days. Our decay time scale of 6 days seems too small to account for the observations, but remember that it is associated with an upper bound value for tropospheric Q_y, and that nonlinear eddy transports were found to erase Q_y in the middle of the channel.

In this chapter we examined simplified basic state flows in order to explain clearly the concept of quasi–modes. In the following chapter we study not only the maintenance of upper–level waves, but also their excitation from favorably oriented initial conditions, in less constrained basic state flows that contain a stratosphere.

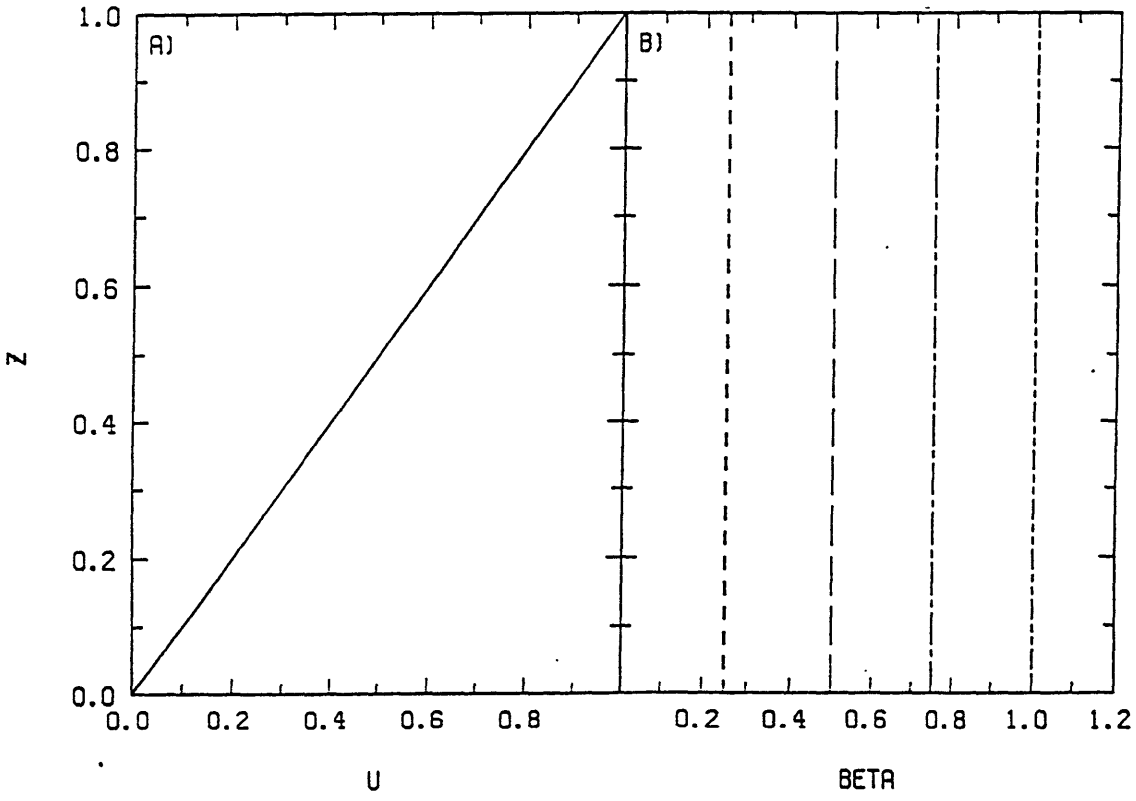

Figure 4.1: The vertical profiles of basic state (a) wind $U(z)$ and (b) QPV gradient $Q_y(z)$. In (b), $\beta = .25$ (short dash line), .5 (long dash line), .75 (long dash - short dash line), and 1 (long dash - short dash - short dash line).

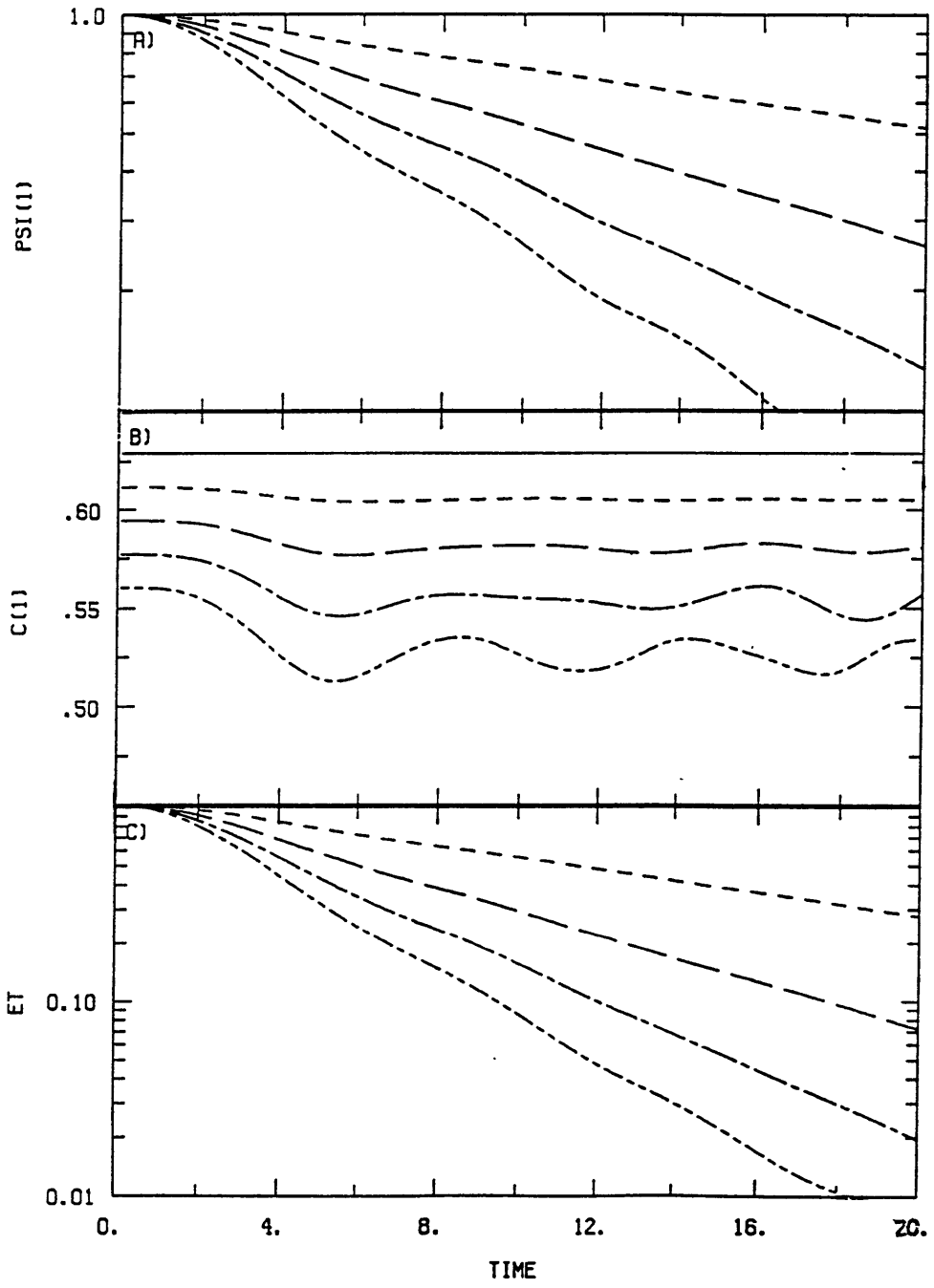

Figure 4.2: Time series of (a) $|\tilde{\psi}|^{z=1}$, (b) $c|^{z=1}$, and (c) E_T for initial–value experiments with $k = 2.3$, $l = 1.4$, and variable β. $\beta = 0$ (solid line), .25 (short dash line), .5 (long dash line), .75 (long dash - short dash line), and 1 (long dash - short dash - short dash line). Initial streamfunction amplitude is fixed to unity at the lid, and E_T is normalized by its initial value.

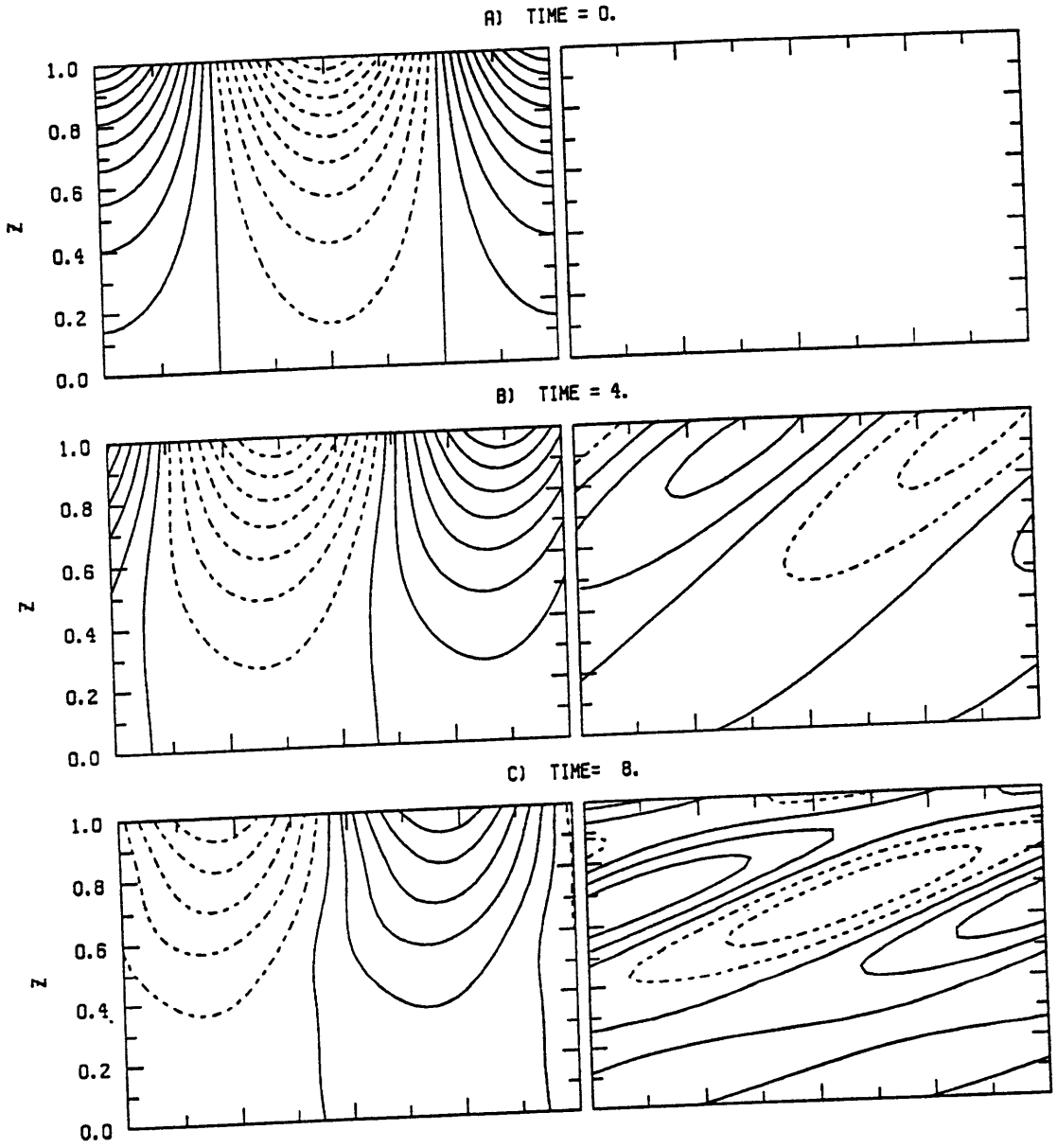

Figure 4.3: Time evolution of the midchannel perturbation streamfunction and QPV fields for the initial–value experiment with $k = 2.3$, $l = 1.4$, and $\beta = .5$. Time=0 (a), 4 (b), 8 (c), 12 (d), 16 (e), and 20 (f). The contour interval is .1 for the streamfunction, and 1 for the QPV. Negative values are dashed. A full zonal wavelength is represented.

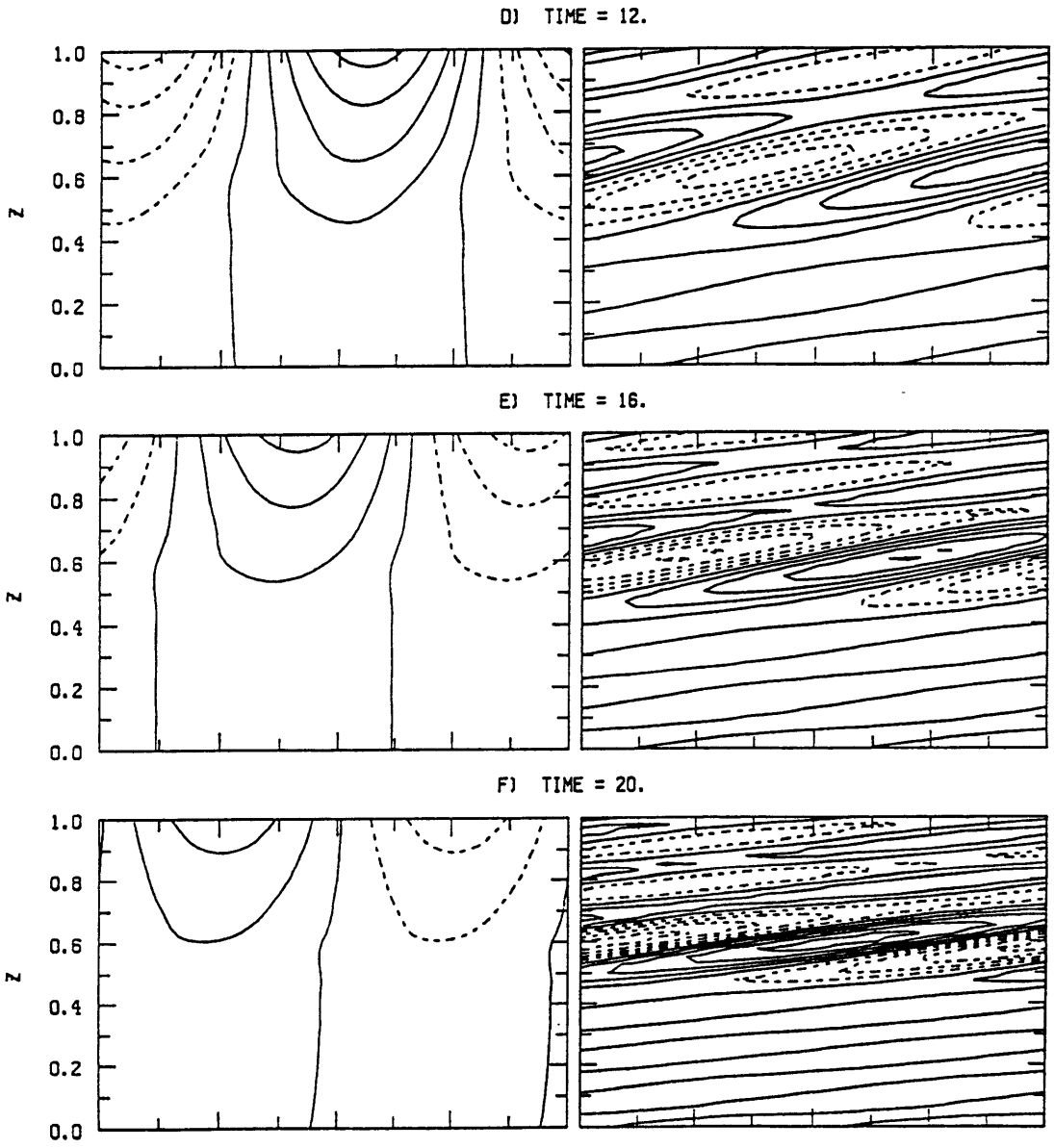
D) TIME = 12.
E) TIME = 16.
F) TIME = 20.
Z
1.0
0.8
0.6
0.4
0.2
0.0

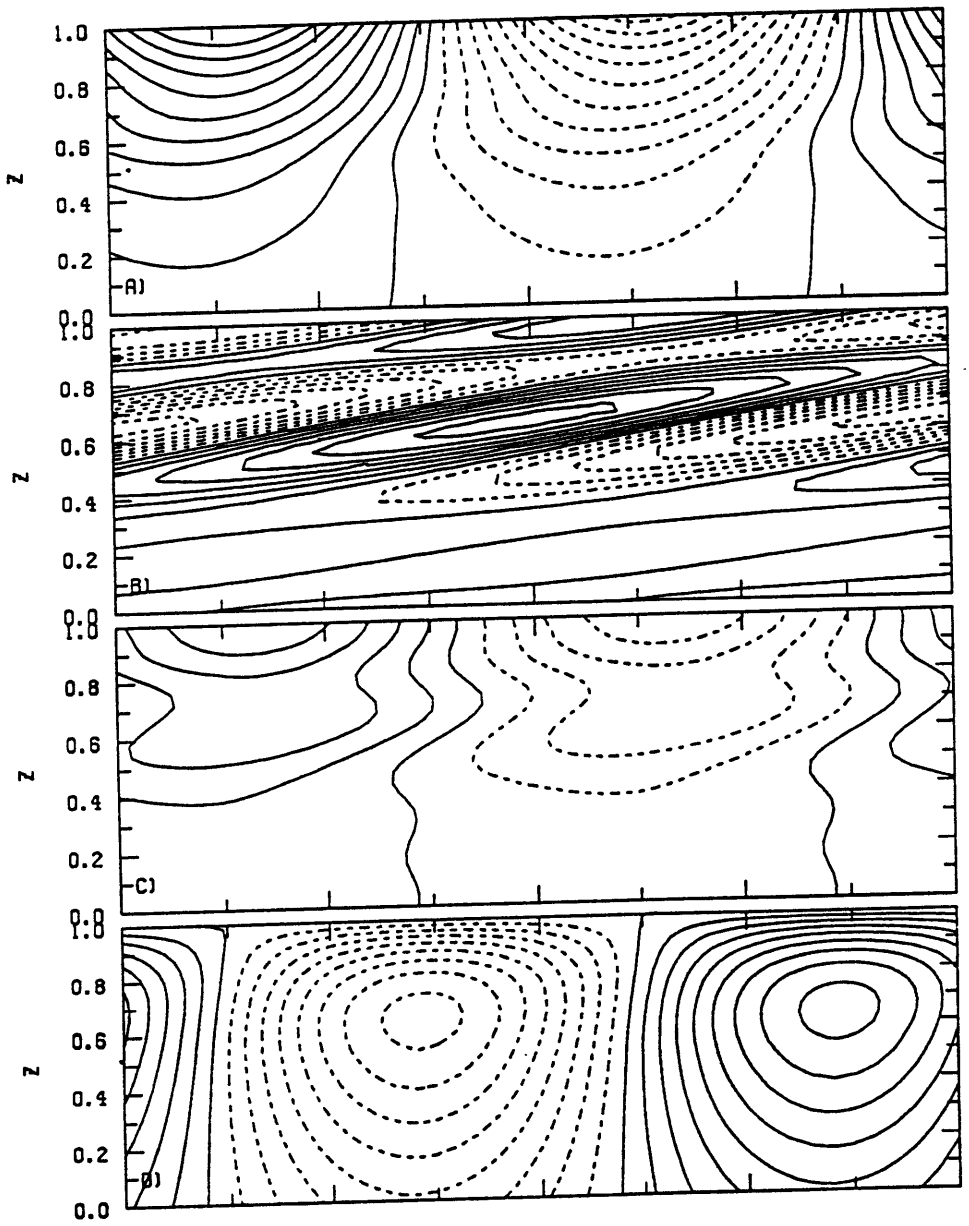

Figure 4.4: Midchannel $x-z$ cross section of perturbation fields for the initial-value experiment with $k = 2.3$, $l = 1.4$, and $\beta = .5$, at time =10. (a) Stream-function, (b) QPV, (c) potential temperature, and (d) vertical velocity. The contour interval is .05 in (a), .5 in (b), .25 in (c) and .05 in (d). Negative values are dashed. A full zonal wavelength is represented.

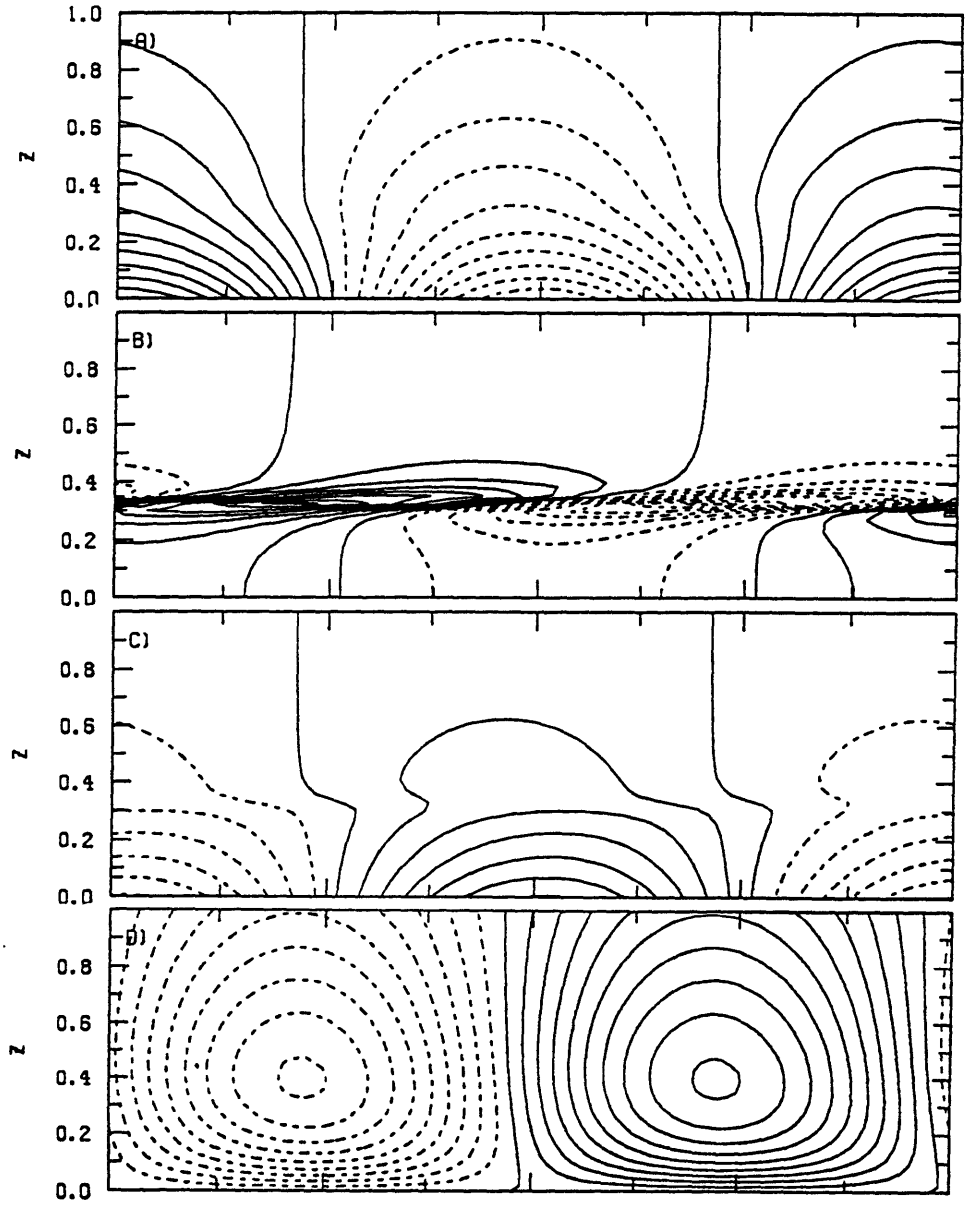

Figure 4.5: Midchannel $x-z$ cross section of perturbation fields for the lower–level Charney mode with $s = 0$, $k = 2.3$, $l = 1.4$, and $\beta = .5$. (a) Streamfunction, (b) QPV, (c) potential temperature, and (d) vertical velocity. Maximum streamfunction amplitude is fixed to unity. The contour interval is .1 in (a), 1 in (b), .5 in (c) and .1 in (d). Negative values are dashed. A full zonal wavelength is represented. Note that the ratios between the different contour intervals are the same than in figure 4.4, so that they can be compared.

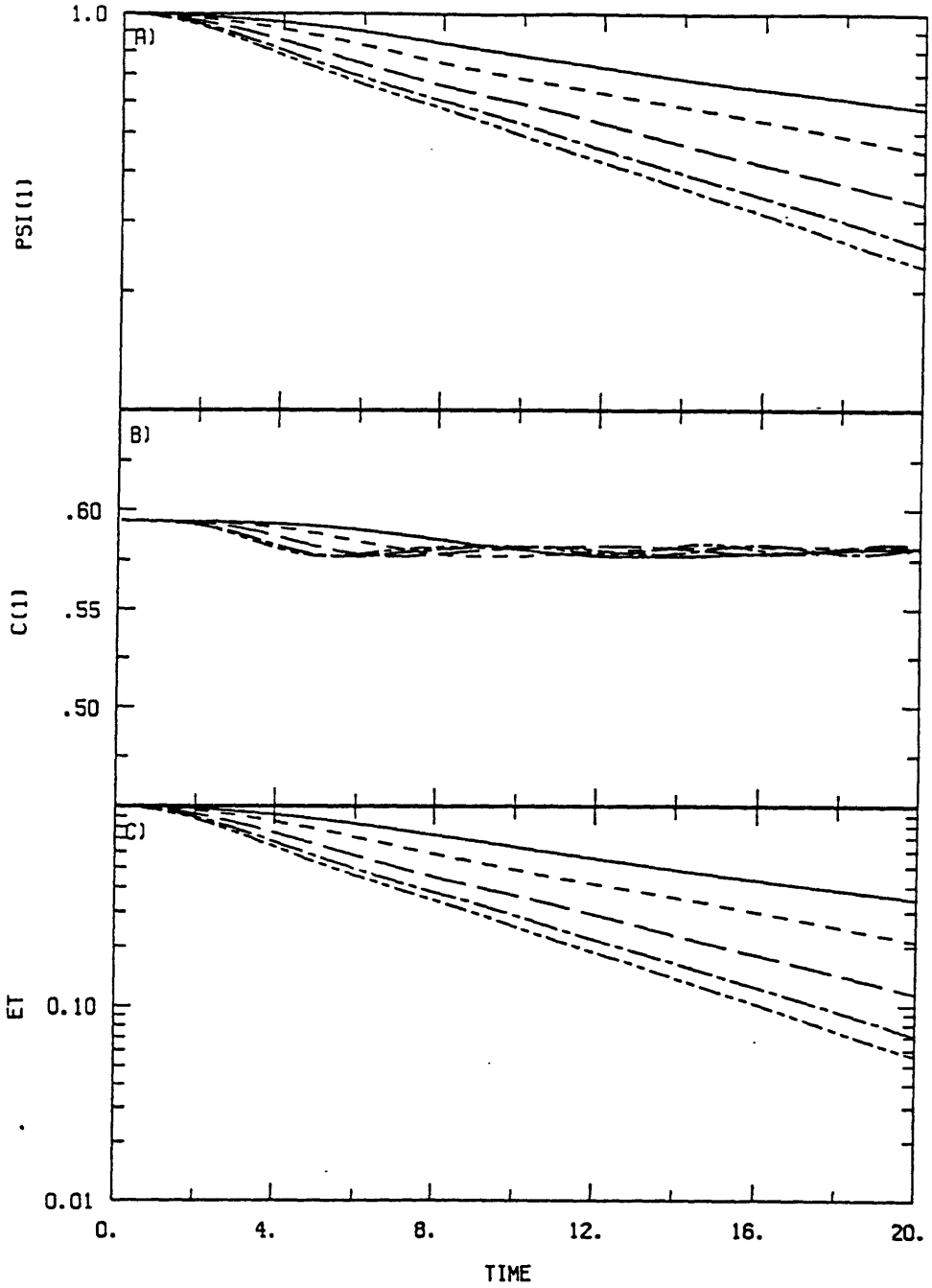

Figure 4.6: Time series of (a) $|\tilde{\psi}|^{z=1}$, (b) $c|^{z=1}$, and (c) E_T for initial–value experiments with $\beta = .5$, $K^2 = 7.25$, and variable k and l. $k = 1, l = 2.5$ (solid line), $k = 1.4, l = 2.3$ (short dash line), $k = 1.9, l = 1.9$ (long dash line), $k = 2.3, l = 1.4$ (long dash - short dash line), and $k = 2.5, l = 1$ (long dash - short dash - short dash line). Initial streamfunction amplitude is fixed to unity at the lid, and E_T is normalized by its initial value.

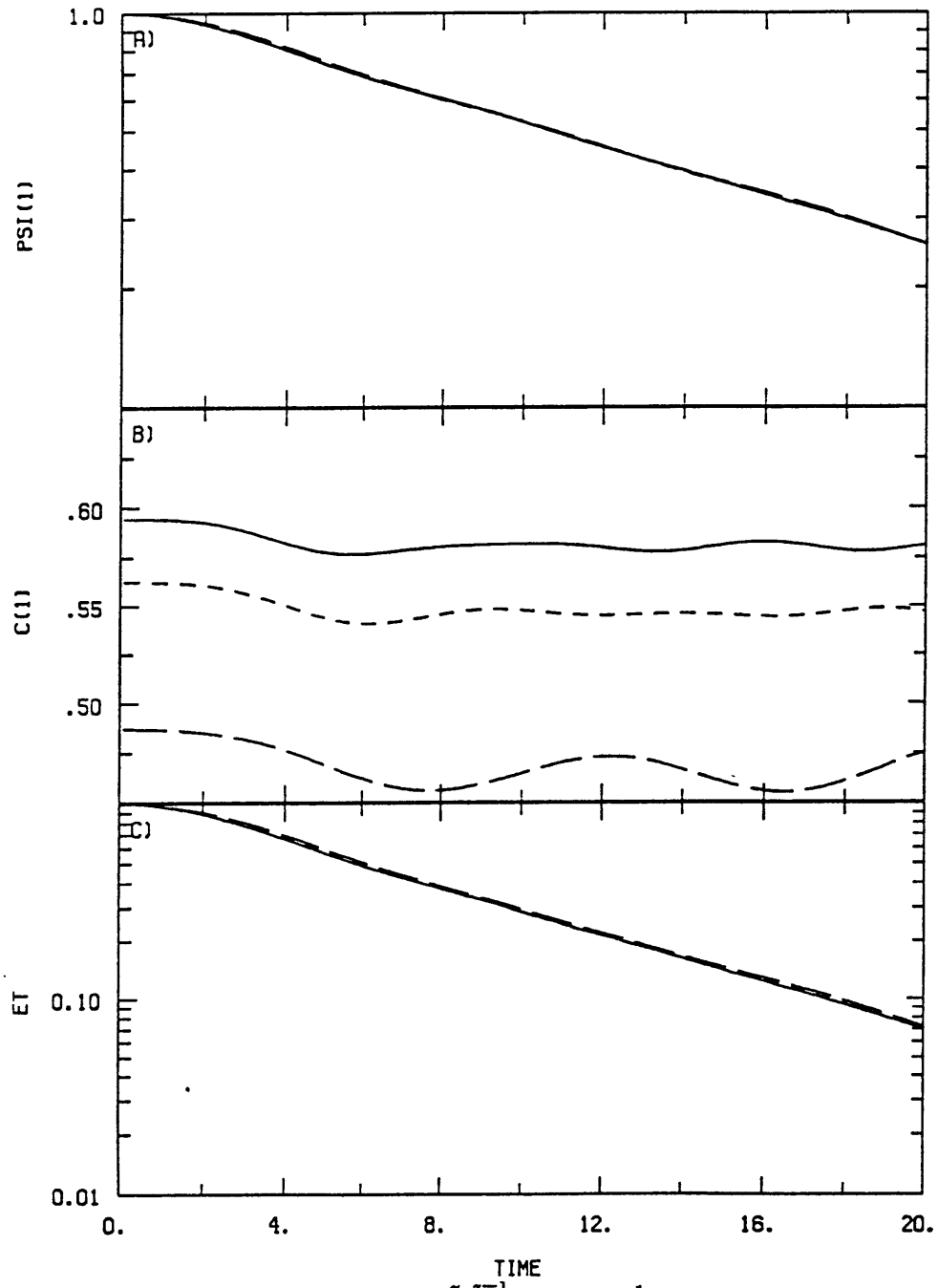

Figure 4.7: Time series of (a) $|\tilde{\psi}|^{z=1}$, (b) $c|^{z=1}$, and (c) E_T for initial–value experiments with $\beta = .5$, $\beta k/K^2 = .159$, and variable k and l. $k = 2.3, l = 1.4$ (solid line), $k = 2, l = 1.518$ (short dash line), and $k = 1.5, l = 1.574$ (long dash line). Initial streamfunction amplitude is fixed to unity at the lid, and E_T is normalized by its initial value.

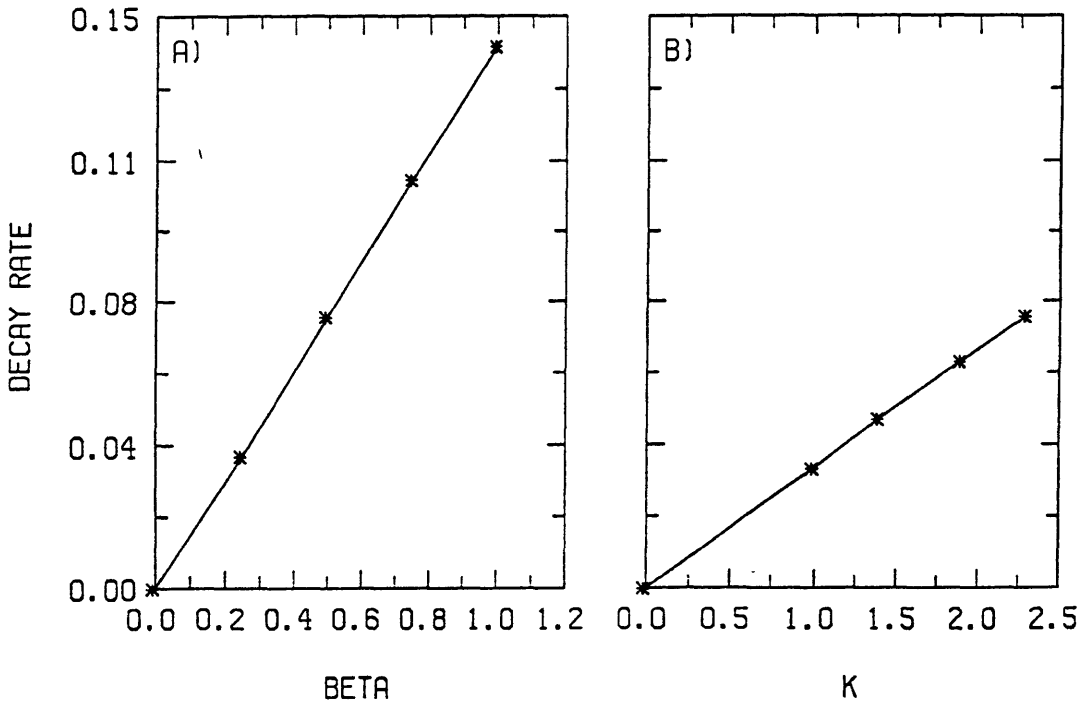

Figure 4.8: Dependencies of the decay rate, Λ, evaluated from initial–value experiments, with respect to (a) β and (b) k. Each star corresponds to a numerical experiment. In (a), results from initial–value experiments with $k = 2.3$ and $l = 1.4$ are displayed, whereas in (b), results from experiments with $\beta = .5$ and $K^2 = 7.25$ are shown.

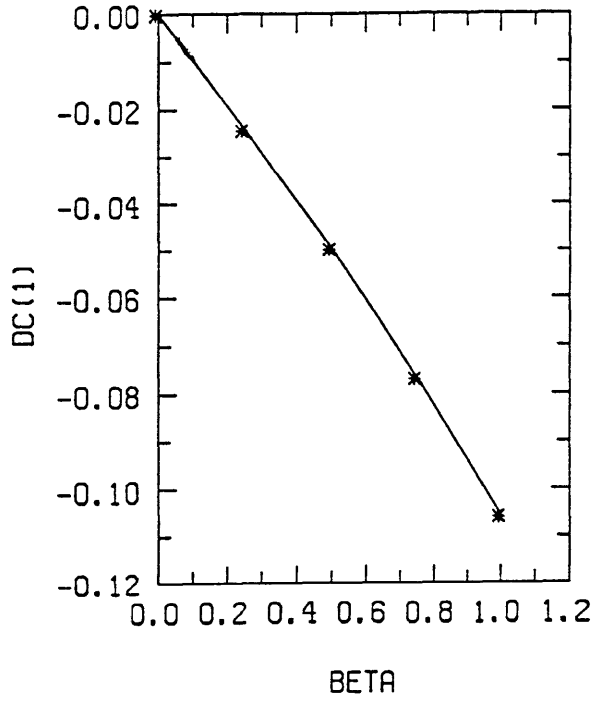

Figure 4.9: Dependency of the propagation speed change, $\Delta c|^{z=1}$, evaluated from initial–value experiments, with respect to β. Each star corresponds to a numerical experiment with $k = 2.3$ and $l = 1.4$.

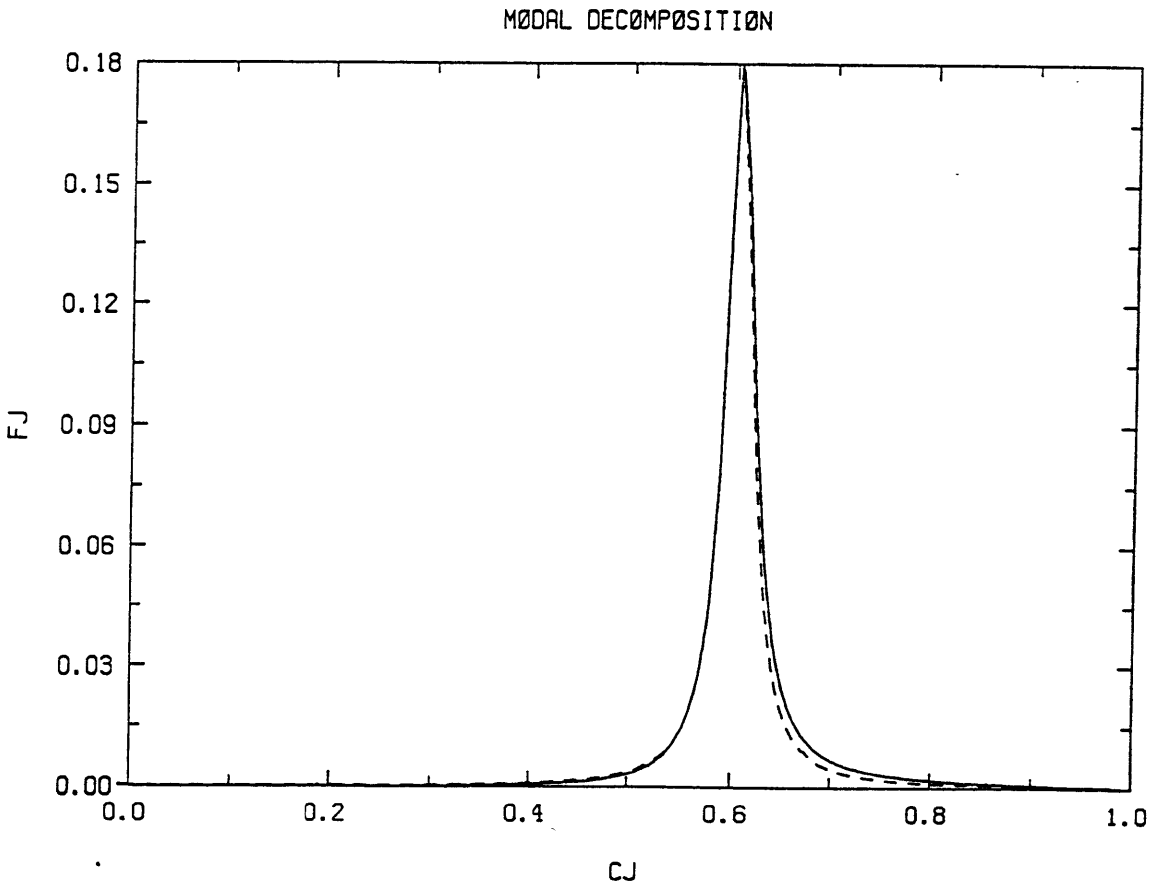

Figure 4.10: Distribution F_j as a function of c_j, for an initial–value experiment with $\beta = .25$, $k = 2.3$, and $l = 1.4$ (solid line), and for an idealized distribution of the form (4.11) with parameters specified in the text (dash line).

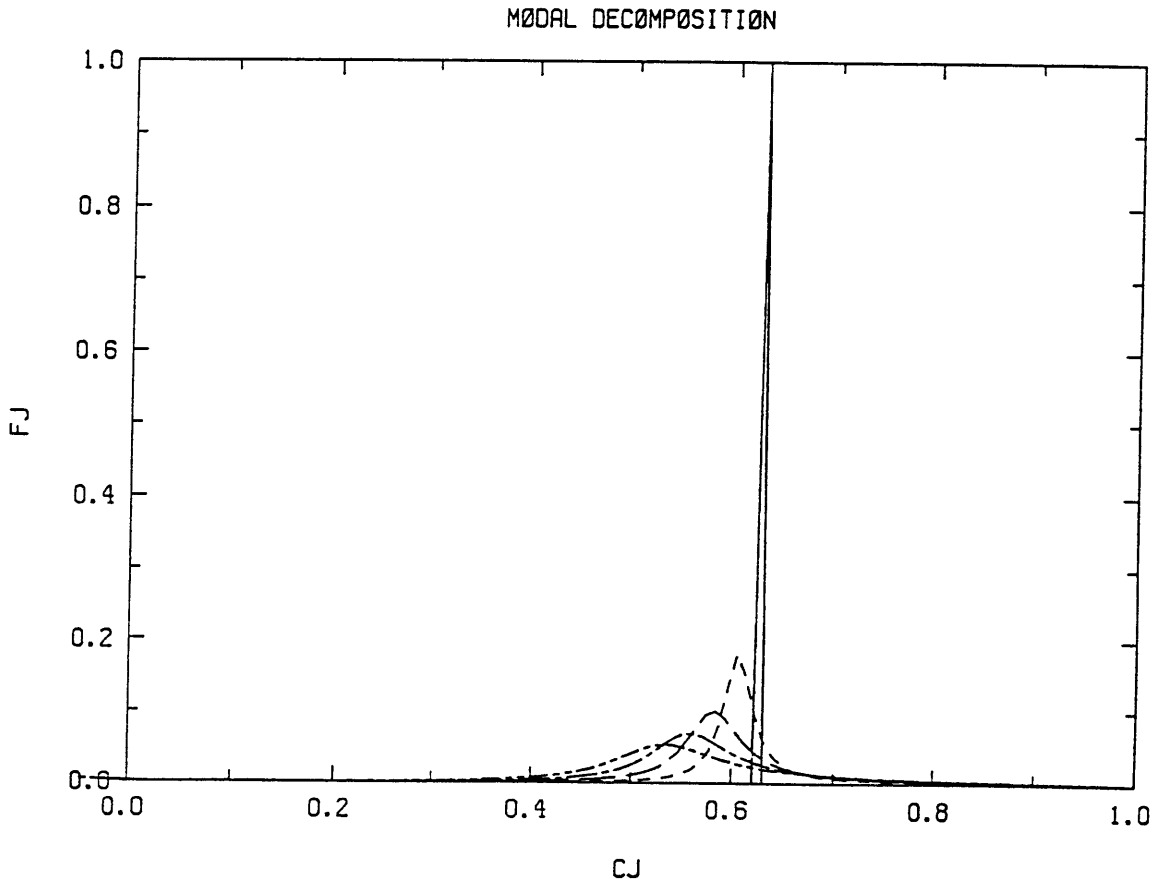

Figure 4.11: Distributions F_j as a function of c_j, for initial–value experiments with $k = 2.3$ and $l = 1.4$. $\beta = 0$ (solid line), .25 (short dash line), .5 (long dash line), .75 (long dash - short dash line), and 1 (long dash - short dash - short dash line).

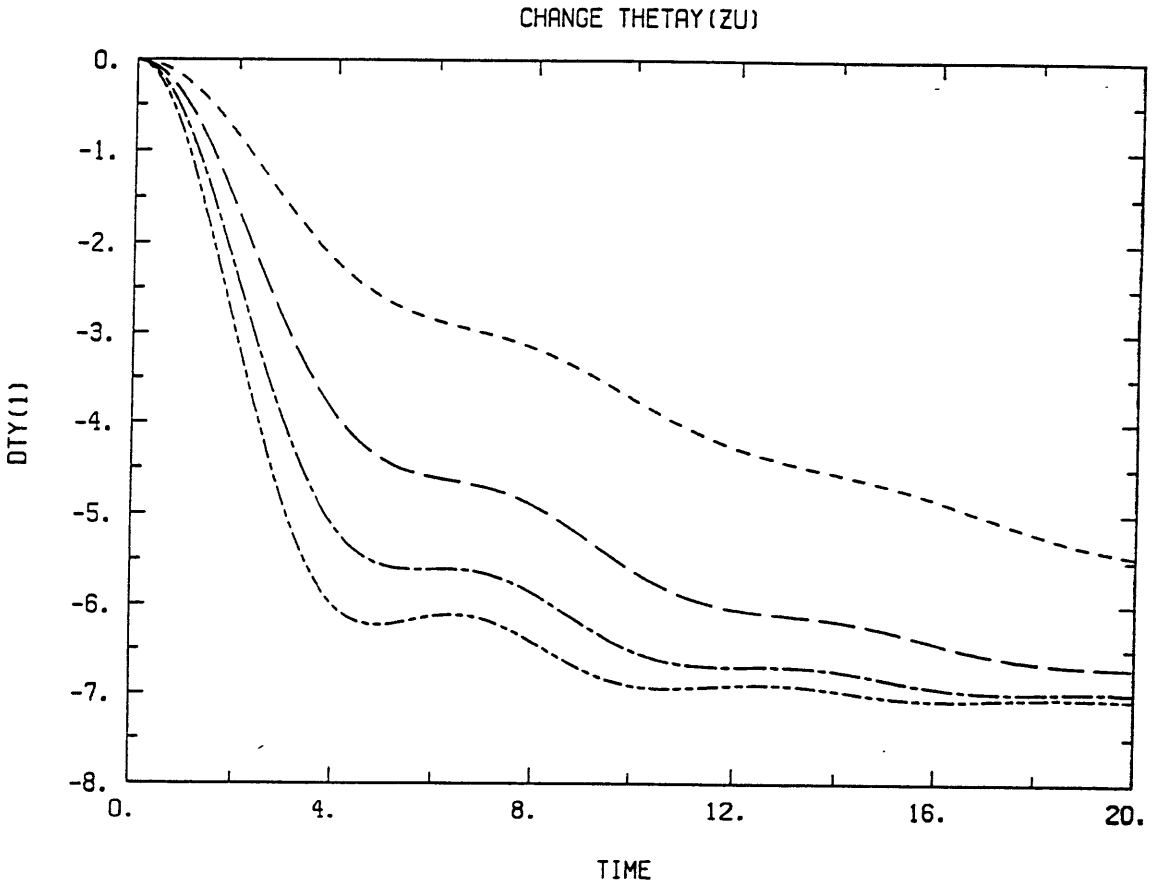

Figure 4.12: Time series of changes in the midchannel mean temperature gradient at the lid for initial–value experiments with $k = 2.3$ and $l = 1.4$. $\beta = .25$ (short dash line), .5 (long dash line), .75 (long dash - short dash line), and 1 (long dash - short dash - short dash line). The initial streamfunction amplitude at the lid is fixed to unity in each experiment.

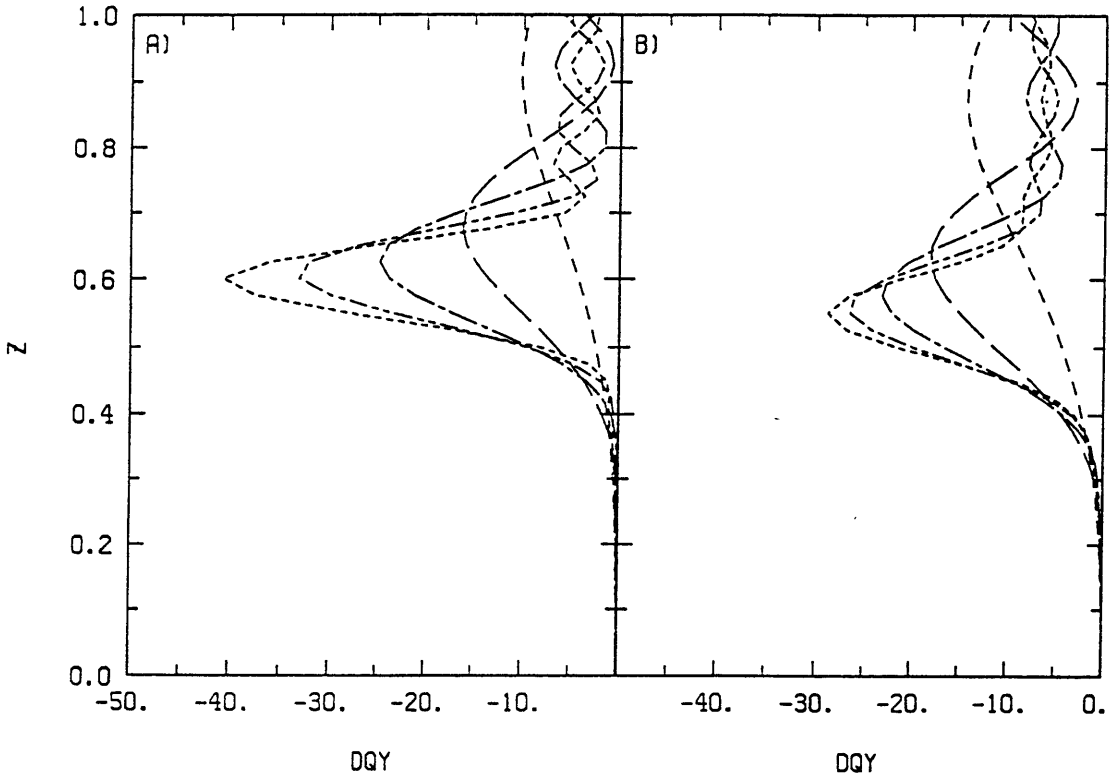

Figure 4.13: Time evolution of the vertical profiles of changes in the midchannel QPV gradient for initial-value experiments with $k = 2.3$ and $l = 1.4$.(a) $\beta = .5$ and (b) $\beta = 1$. Time=4 (small dash line), 8 (long dash line), 12 (long dash - small dash line), 16 (long dash - small dash - small dash line), and 20 (very small dash line). The initial streamfunction amplitude at the lid is fixed to unity in each experiment.

Chapter 5

Waves on basic states with interior tropospheric and stratospheric potential vorticity gradients

5.1 Introduction

In this chapter we examine upper–level waves in the presence of interior tropospheric and stratospheric potential vorticity gradients. Furthermore, whereas previous chapters only addressed the problem of the maintenance of upper–level waves, this chapter also addresses their excitation and identifies favorable initial conditions from which upper–level waves can emerge.

We consider here a semi–infinite atmosphere with a lower rigid boundary. The basic states are similar to those associated with S2 solutions in chapter 3. As was presented in section 3.2.4, S2 basic states have a density profile

that decays exponentially with height, a static stability that decreases with height in the troposphere and jumps to a typical stratospheric value at the tropopause, and a wind with constant shear in the troposphere and no shear above the tropopause. In the basic states considered here the density decays exponentially with height and unlike the S2 profiles, the profiles of wind shear and static stability remain continuous with height. Furthermore, the planetary gradient of potential vorticity, β, is included. For such basic states, the meridional gradient of quasi–geostrophic pseudo–potential vorticity, Q_y, has strong positive values in the neighborhood of the tropopause and reduces to β in the tropospheric and stratospheric interiors.

When β vanishes, the basic state supports at the synoptic scale neutral upper–level wave solutions that share much of the characteristics of the solutions presented in chapter 3. When β is nonzero, the basic states support slowly decaying quasi–modes with characteristics comparable to those found in chapter 4. The presence of stratospheric Q_y and of a rigid lower boundary does not modify the overall characteristics of the results presented in chapter 4.

Farrell (1989) found that the adjoint of a given mode is the optimal perturbation to excite that mode in the total perturbation energy (E_T) norm. Following a procedure like that of Montgomery and Farrell (1990), we calculate near optimal initial conditions for the upper–level wave solution when β is zero. These initial conditions have a streamfunction and QPV fields that are concentrated in the upper troposphere and that lean against the shear.

The amount by which perturbation fields lean against the shear determines the time scale and magnification associated with the excitation. For excitation with time scales of 4 days, E_T grows by a factor of 70 and the streamfunction amplitude by 10.

When β is nonzero, the basic states no longer support neutral upper–level wave modes but slowly decaying quasi–modes. However, the excitation of quasi–modes proceeds in a manner similar to that of neutral modes, and for a reasonable β, magnification of the same order of magnitude is observed. At $\beta = .5$, which corresponds to an upper bound for the tropospheric Q_y, E_T grows by a factor of 30 and the streamfunction amplitude by a factor of 10 for an excitation time of 4 days. Following the excitation, there is an interval of growth after which the quasi–mode decays slowly with time.

In section 5.2, we present characteristics of the basic states, and the methods of solution to the mathematical problems encountered in this chapter. Section 5.3 discusses the upper–level wave solutions and section 5.4 their excitation from favorable initial conditions. A discussion of the results is found in section 5.5.

5.2 Formulation

5.2.1 Basic states

We assume in this chapter a semi–infinite atmosphere with a rigid lower boundary at $z = 0$. The density decays exponentially with height at a constant rate, $s = 1$. The basic state wind takes the following form,

$$\begin{aligned} z < z_t - \delta_u,\ U(z) &= z, \\ z > z_t - \delta_u,\ U(z) &= (z_t - \delta_u) + \delta_u \tanh\left(\frac{z - (z_t - \delta_u)}{\delta_u}\right). \end{aligned}$$

We set the tropopause height to unity, $z_t = 1$, and $\delta_u = .15$. The static stability profile is

$$N^2(z) = \left(\frac{N_1^2 + N_2^2}{2}\right)\left[1 + \tanh\left(\frac{z - z_t}{\delta_N}\right)\right] + N_1^2\left(e^{-s(z-z_t)} - 1\right).$$

We fix the tropospheric and stratospheric static stability: $N_1^2 = 1$ and $N_2^2 = 4.5$, and $\delta_N = .05$. For these profiles of wind and static stability, all basic state quantities that enter the equations to be solved are continuous, because N^2 and all its derivatives are continuous, and U and its first and second derivatives are also continuous. Figure 5.1 displays the vertical profiles of U and N^2. Note the increased stability close to the ground that is characteristic of the extratropical atmosphere where lapse rates at lower levels are generally smaller than at upper levels.

The vertical profiles of Q_y for different values of β are shown in figure 5.2. It strongly peaks at the tropopause and reduces to β in the troposphere and

stratosphere. The temperature gradient at the lower boundary is equivalent to a thin sheet of infinite negative Q_y (Bretherton, 1966). The necessary condition for normal mode instability of the Charney–Stern theorem is then satisfied (remember section 2.1.3). In this chapter we consider fixed zonal and meridional wavenumbers, $k = 2.3$ and $l = 1.4$, which correspond to a zonal wavelength of 2500 km and to a channel width of 2000 km. At that horizontal scale the basic state with $\beta = 0$ does not support any normal mode instability; when $0 < \beta < 1$ however, there exist low–level modes of marginal instability.

5.2.2 Solutions to the eigenvalue and initial–value problems

In this chapter we solve numerically a number of eigenvalue and initial–value problems. We consider a lower inviscid rigid boundary condition, [$\eta_l = 0$ in (2.21)], at $z_l = 0$, and an approximate boundary condition for trapped waves, (B.10), at a fictitious upper boundary located at $z_u = 1.6$.

In section 4.3 we calculate numerically the upper–level normal mode associated with the basic state that has zero β. Because the vertical structure of the mode has a strong maximum in the middle of the domain, we could not calculate it with the shooting method presented in section 2.2.1. Instead we computed the total spectrum of modes with a method presented in section 2.2.2. The vertical resolution was fixed to $\triangle z = .02$, and a test of the convergence was done with $\triangle z = .016$.

In section 4.3 we also calculate numerically the lower–level unstable modes

for basic states with nonzero β. Since the modes decay monotonically with height, it was possible to compute them with the technique described in section 2.2.1. We used the same vertical resolution as for the calculation of the upper–level mode.

In sections 4.3 and 4.4 we present solutions to initial–value problems. Numerical details on the method of solution and the calculation of diagnostics can be found in section 2.2.3. The time step is set to $\Delta t = .05$, and the vertical resolution to $\Delta z = .02$. Experiments are also run with $\Delta t = .025$ and $\Delta z = .016$ to test the convergence of the results.

In section 4.3 the initial condition consists of the upper–level modal solution for basic state with zero β that is computed numerically. In section 4.4 the initial conditions are near optimal perturbations given by

$$\tilde{\psi}_{no} = \frac{\hat{\psi}_{UL}}{U(z) - (c_{UL} - i\epsilon)}, \tag{5.1}$$

as in Montgomery and Farrell (1990). $\hat{\psi}_{UL}$ and c_{UL} are the streamfunction field and the phase speed associated with the upper–level mode for basic state with zero β. ϵ is an arbitrary factor that controls the amount by which the perturbation fields lean against the shear. When $\epsilon = 0$, $\tilde{\psi}_{no}$ is simply the adjoint of the mode and would be the optimal perturbation in the E_T norm for basic states with constant stability and density (Farrell, 1989). The fact that c_{UL} is real for strictly neutral modes causes these adjoint modes to be singular. For that reason, we consider here resolvable near optimal excitations with $\epsilon = .1$, .15, and .3.

5.3 The upper–level wave solutions

Figure 5.3 displays the character of the neutral upper–level wave solution for the basic state with $\beta = 0$; perturbation streamfunction, QPV, potential temperature, and vertical velocity fields are shown. It is interesting to compare this figure with figure 3.10 that represents the fields associated with the neutral upper–level wave solution for a basic state that has concentrated Q_y at the tropopause. The perturbation fields of streamfunction, potential temperature, and vertical velocity are remarkably similar in the two cases, qualitatively and quantitatively. The perturbation QPV field in figure 5.3 is sharply peaked at the tropopause rather than being concentrated in a thin sheet of infinite magnitude. The upper–level wave solution displayed in figure 5.3 propagates at a phase speed, $c = .73$, which is slightly less than that associated with the upper–level normal mode for the S2 basic state.

In a series of initial–value experiments that resemble those performed in chapter 4, we examine what happens to the neutral upper–level wave solution in the presence of stratospheric and tropospheric Q_y. Figure 5.4 displays the time series of $|\psi|^{z=1}$, $c|^{z=1}$, and E_T for experiments with $\beta = 0$, .25, .5, and .75. When β is nonzero, the streamfunction amplitude at $z = 1$ and the total perturbation energy decay with time, and the decay rate increases as β increases. The propagation rate at the tropopause decreases as β increases. At $\beta = .5$, the exponential decay rate for the streamfunction amplitude at $z = 1$ is .064 which corresponds to a time scale of 16 units (dimensionally 6.1 days). This decay time scale compares well with that of 5.5 days found in chapter

4 at $\beta = .5$ for the same horizontal scale.

Figure 5.5 displays the time evolution of $\tilde{\psi}$ and $\tilde{q}$, for $\beta = .5$. At the initial time the streamfunction field corresponds to the neutral upper–level wave solution. The phase lines are vertical. At later time, eddy QPV is generated in the stratosphere and the troposphere, and the streamfunction field acquires a downshear tilt in the troposphere. The magnitude of the QPV and streamfunction extrema at the tropopause decreases, and another extremum in the QPV field is generated in the critical region below the tropopause, around $z = .7$. This time evolution is very similar to that represented in figure 4.3 which depicts the case with a rigid tropopause and no lower boundary. The results of chapter 4 are robust, and hold in the presence of the ground and the stratosphere. Figure 5.6 depicts the change in QPV gradient, $\triangle Q_y(z)$, induced by the wave transport. In the middle of the channel the wave acts to erase the gradients in the critical region around $z = .7$, and to enhance the gradients above around $z = .9$.

In the initial–value experiments with $\beta > 0$ presented in this section, we do not observe a rapid development of lower–level waves. The presence of enhanced stability at the ground causes the lower–level waves to be only marginally unstable. For instance at $\beta = .5$, their growth rate is .027, which corresponds to an exponential time scale of 15.9 time units (dimensionally, 6.2 days).

Table 5.1: Magnifications for a basic state with $\beta = 0$

ϵ	$\lvert\tilde{\psi}\rvert^{z=1,\max}/\lvert\tilde{\psi}\rvert^{z=1,t=0}$	$E_T^{\max}/E_T^{t=0}$
.1	35.8	205.3
.15	14.5	74.1
.3	3.7	10.3

5.4 The excitation of upper–level waves

Figure 5.7 displays the character of the near optimal initial condition for an intermediate value of ϵ, $\epsilon = .15$; perturbation streamfunction, QPV, temperature, and vertical velocity fields are shown. All fields possess a pronounced maximum amplitude just below the tropopause and a marked upshear tilt with height. From table 2.1, a height perturbation of 1 dm would have associated temperature and vertical velocity perturbations of 2° K and .4 cm/s.

When ϵ is smaller, the disturbances possess a larger amount of upshear tilt and are more concentrated around the critical level of the upper–level neutral normal mode [remember (5.1)]. At equal amplitudes in the streamfunction and vertical velocity fields, they also have stronger amplitudes in the QPV and temperature fields. Since the excitation of the upper–level mode takes place as the shear acts on the initial condition, near optimal conditions with smaller ϵ and larger amount of upshear tilt lead to longer excitation times and larger growths, and the opposite is true when ϵ is larger. For values of ϵ considered here, .1, .15, and .3, the excitation time scales are approximatively of 15, 10, and 5 time units (dimensionally, 6, 4, and 2 days).

Table 5.2: Magnifications for a basic state with $\beta = .5$

ϵ	$\|\tilde{\psi}\|^{z=1,\max}/\|\tilde{\psi}\|^{z=1,t=0}$	$E_T^{\max}/E_T^{t=0}$
.1	22.4	81.1
.15	9.4	31.2
.3	2.9	6.1

Let us now examine the excitation on a basic state with $\beta = 0$ and which supports an upper–level normal mode. Figure 5.8 shows the time evolution of $|\psi|^{z=1}$, $c|^{z=1}$, and E_T for near optimal initial conditions with different values of ϵ. The streamfunction amplitude at $z = 1$ and the total perturbation energy first increase with time and then remain constant. When ϵ is smaller, the growth is larger and takes longer to occur. Table 5.1 contains the magnifications in $|\psi|^{z=1}$ and E_T for the different experiments. At $\epsilon = .15$ the amplitude is magnified by a factor of 15 and the energy by 74. Figure 5.9 displays the time evolution of the streamfunction and QPV fields for $\epsilon = .15$. The shear acts on the initially tilted disturbance and excites the upper–level normal mode.

Now we look at the same excitation, but on a basic state with $\beta = .5$ and which does not support an upper–level normal mode but a quasi–mode. Figure 5.10 shows the time evolution of the same diagnostics as in figure 5.8 for such a basic state. As in figure 5.8, the streamfunction amplitude and the energy first increase with time, but the excitation is followed by a slow decay. Table 5.2 contains the magnifications for the basic state wtih $\beta = .5$. At $\epsilon = .15$, the amplitude grows by a factor of 9 and the energy by 31. These magnifications

are of the same order of magnitude as those for the basic state with zero β. Figure 5.10 shows the time evolution of $\tilde{\psi}$ and $\tilde{q}$ for $\epsilon = .15$. Even in the absence of an upper–level normal mode, the excitation of the upper–level wave takes place.

5.5 Discussion

The first series of results presented in this chapter confirms the robustness of upper–level wave solutions at the synoptic scale. We first showed that the overall characteristics of the neutral upper–level wave solution presented in chapter 3 also extend for basic states with a smooth tropopause. Note that the neutral upper–level wave solution for basic state with $\beta = 0$ studied in this chapter is a nonlinear solution of the quasi–geostrophic equations. When β is nonzero, we demonstrated that the slow decay of the upper–level wave proceeds as in chapter 4 even in the presence of a lower boundary and the stratosphere.

The second series of results concerns the excitation of upper–level wave solutions. We identified disturbances concentrated in the upper troposphere with strong upshear tilt as near optimal conditions for the emergence of upper–level waves. We further showed that the excitation takes place in a similar manner on basic states with zero and nonzero β. This result is new and important since it signifies that quasi–modes that consist of a superposition of singular modes are as likely to emerge from an initial condition as strict

normal modes.

It is interesting to compare the development scenario proposed in this chapter with the observational work of Sanders (1988). In his paper he shows composite maps of perturbation fields of geopotential and temperature, for the day before initiation of upper–level mobile troughs. There is no clear correspondence between these and the near optimal initial conditions described in the present chapter. However, the near optimal initial conditions represent a powerful mechanism for the excitation of upper–level waves. More observational studies are needed to assess its importance in the midlatitude flow.

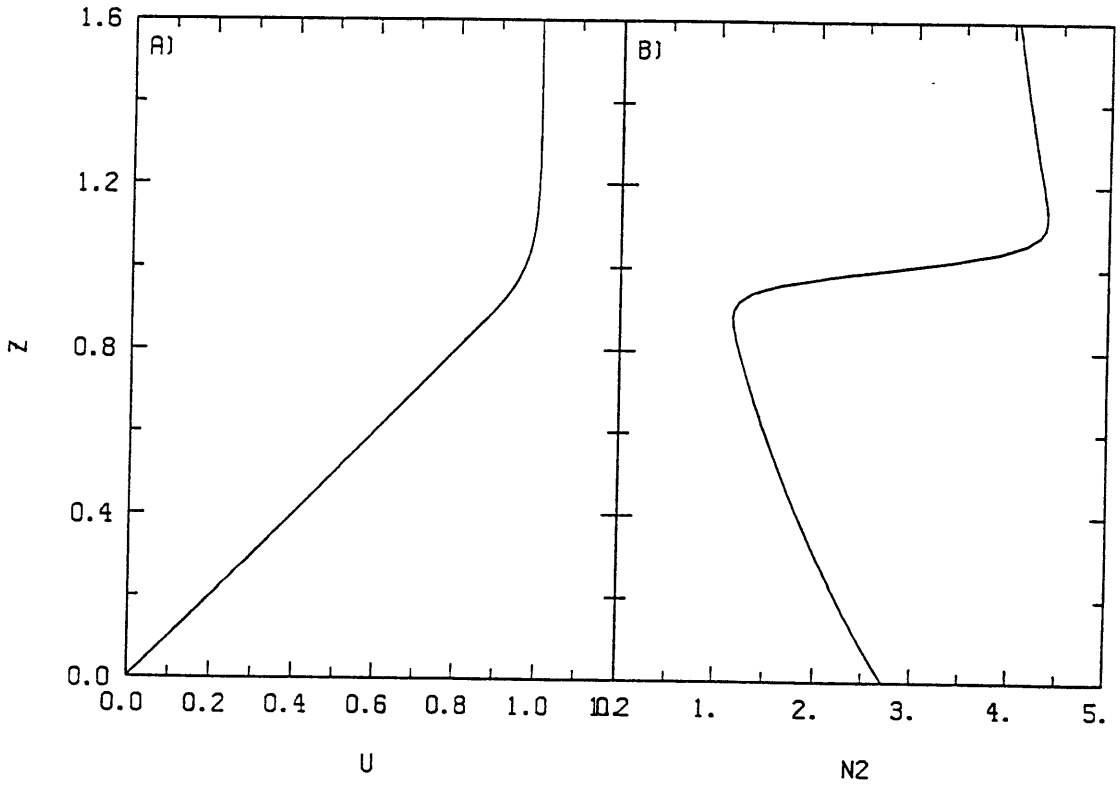

Figure 5.1: The vertical profiles of basic state (a) wind $U(z)$ and (b) stability $N^2(z)$.

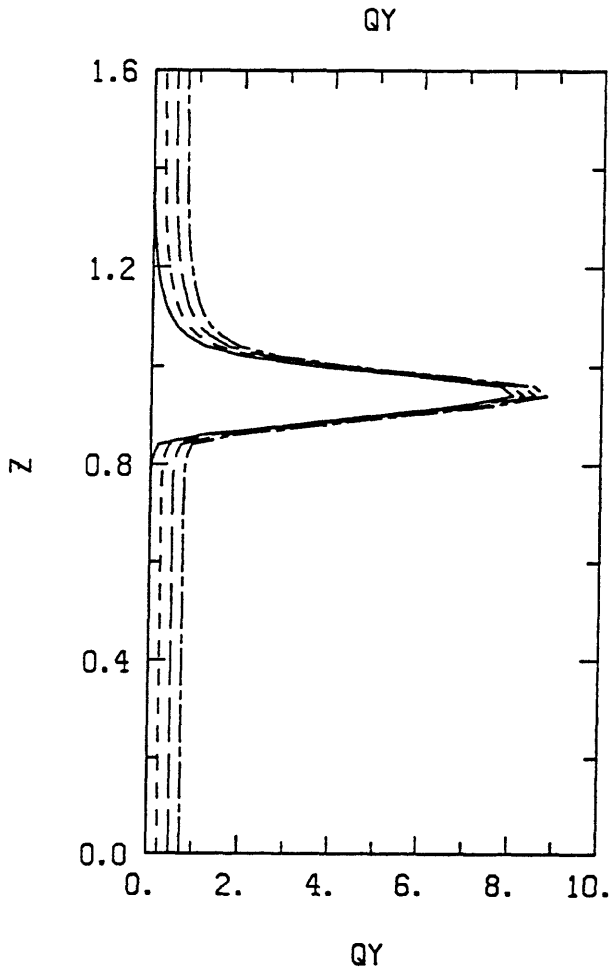

Figure 5.2: The vertical profiles of basic state QPV gradient, Q_y. $\beta = 0$ (solid line), .25 (short dash line), .5 (long dash line), and .75 (long dash - short dash line).

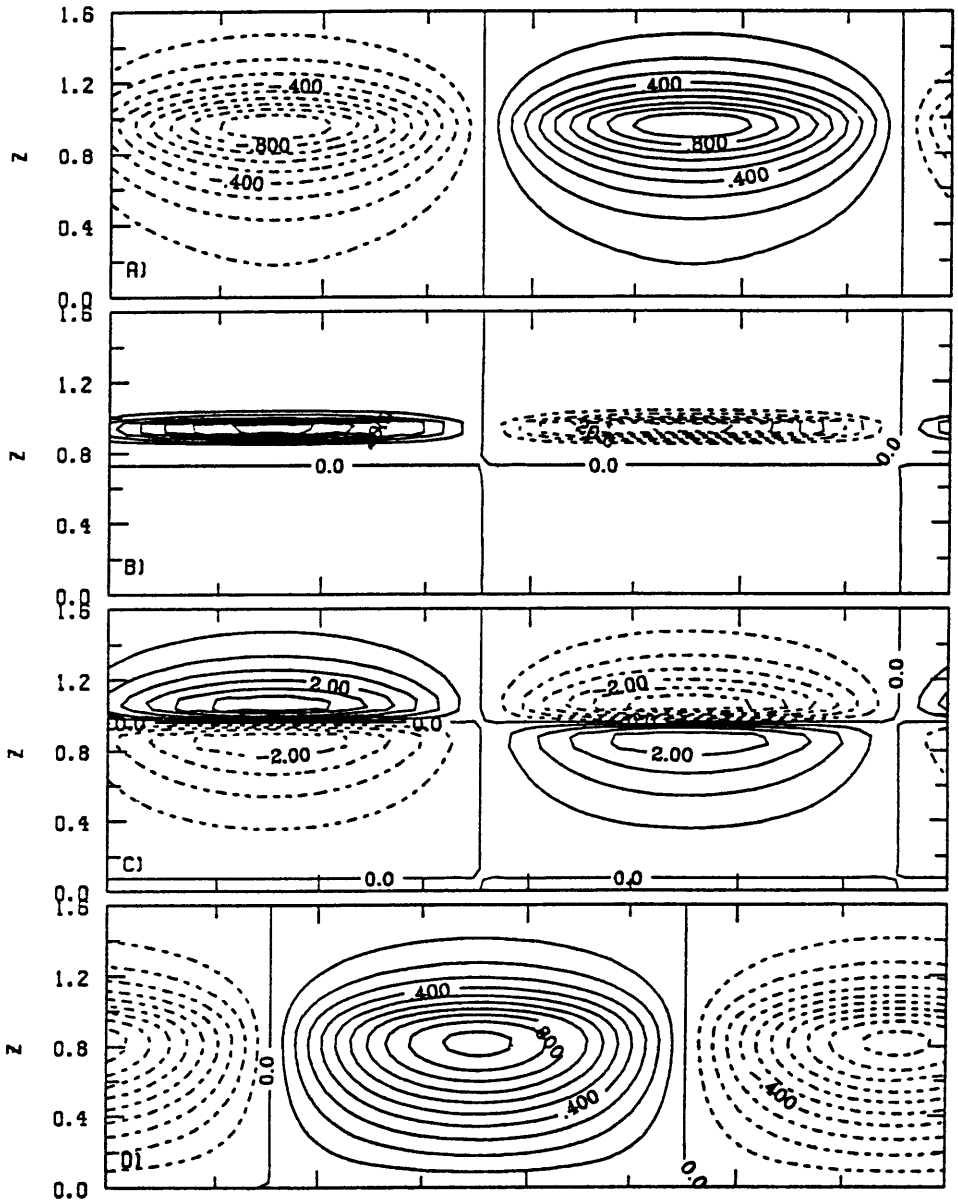

Figure 5.3: Midchannel $x-z$ cross section of perturbation fields for the upper-level normal mode at $k = 2.3$, $l = 1.4$, and $\beta = .0$. (a) Streamfunction, (b) QPV, (c) potential temperature, and (d) vertical velocity. The contour interval is .1 in (a), 5 in (b), .5 in (c) and .1 in (d). Negative values are dashed. A full zonal wavelength is represented.

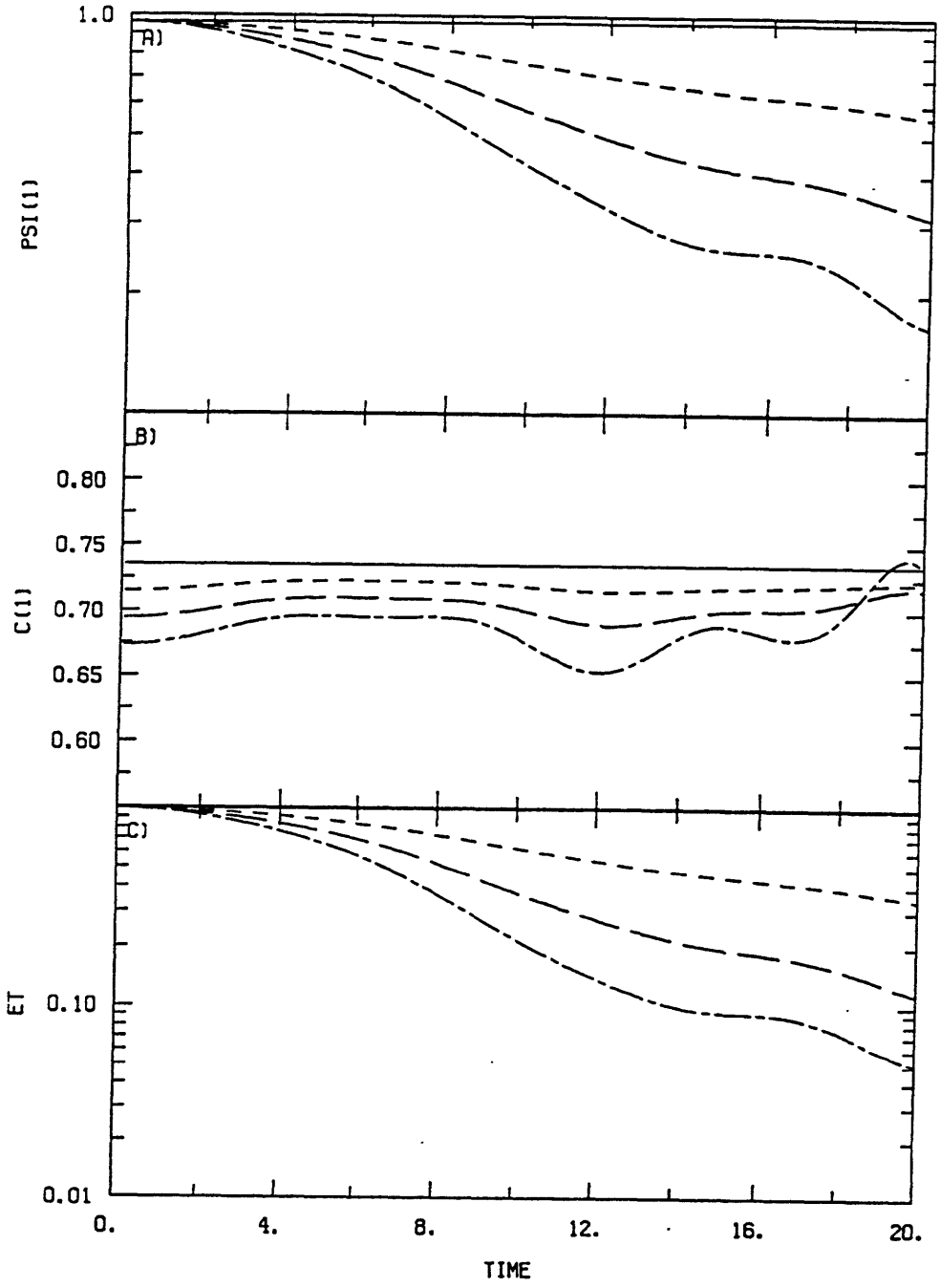

Figure 5.4: Time series of (a) $|\tilde{\psi}|^{z=1}$, (b) $c|^{z=1}$, and (c) E_T for initial–value experiments with $k = 2.3$, $l = 1.4$, and variable β. $\beta = 0$ (solid line), .25 (short dash line), .5 (long dash line), and .75 (long dash - short dash line). The initial condition consists of the upper–level normal mode for the basic state with zero β. Initial streamfunction amplitude is fixed to unity at the tropopause, and E_T is normalized by its initial value.

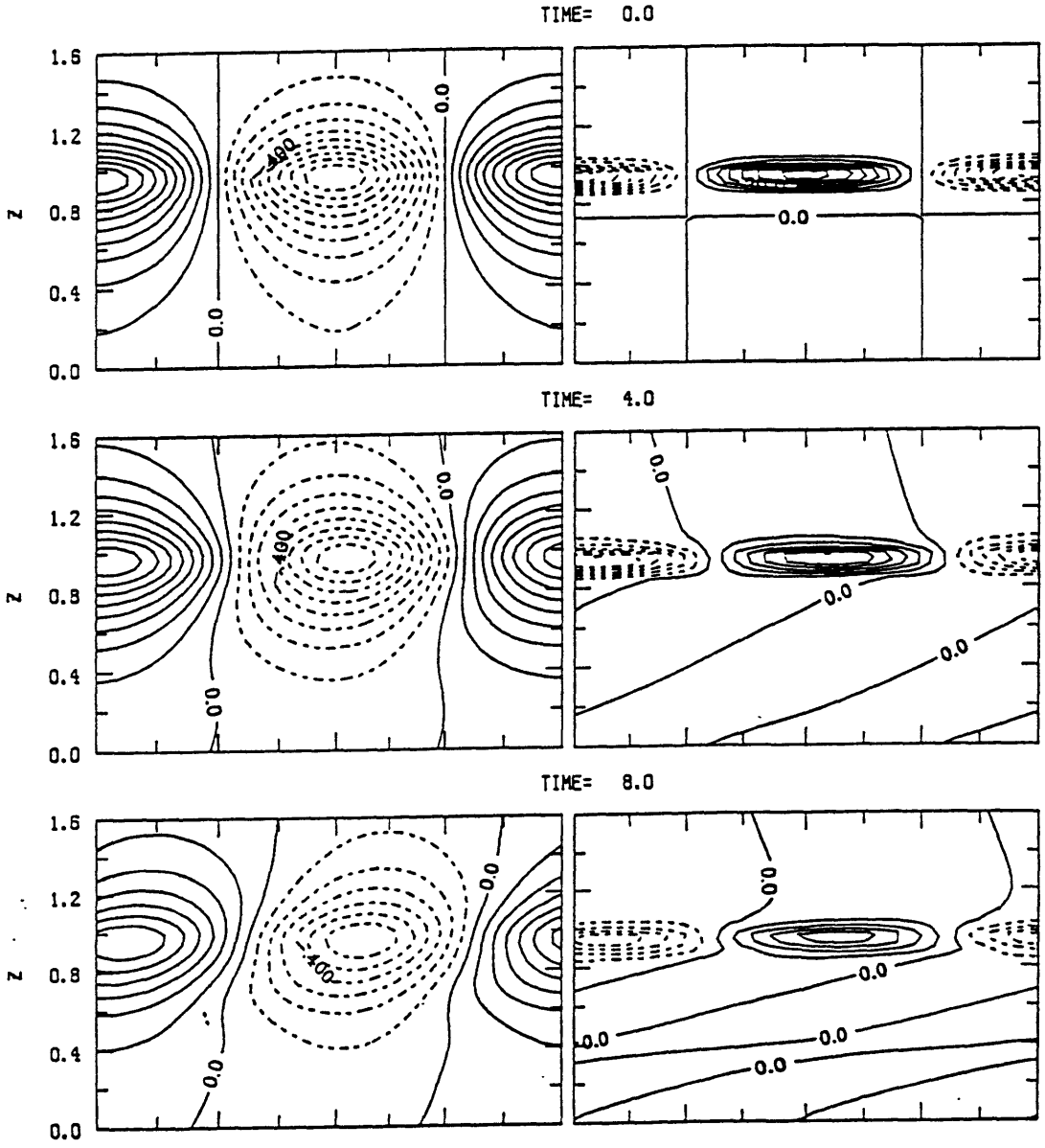

Figure 5.5: Time evolution of the midchannel perturbation streamfunction and QPV fields for the initial-value experiment with $k = 2.3$, $l = 1.4$, and $\beta = .5$. Time=0 (a), 4 (b), 8 (c), 12 (d), 16 (e), and 20 (f). The initial condition consists of the upper-level normal mode for the basic state with zero β. The contour interval is .1 for the streamfunction, and 5 for the QPV. Negative values are dashed. A full zonal wavelength is represented.

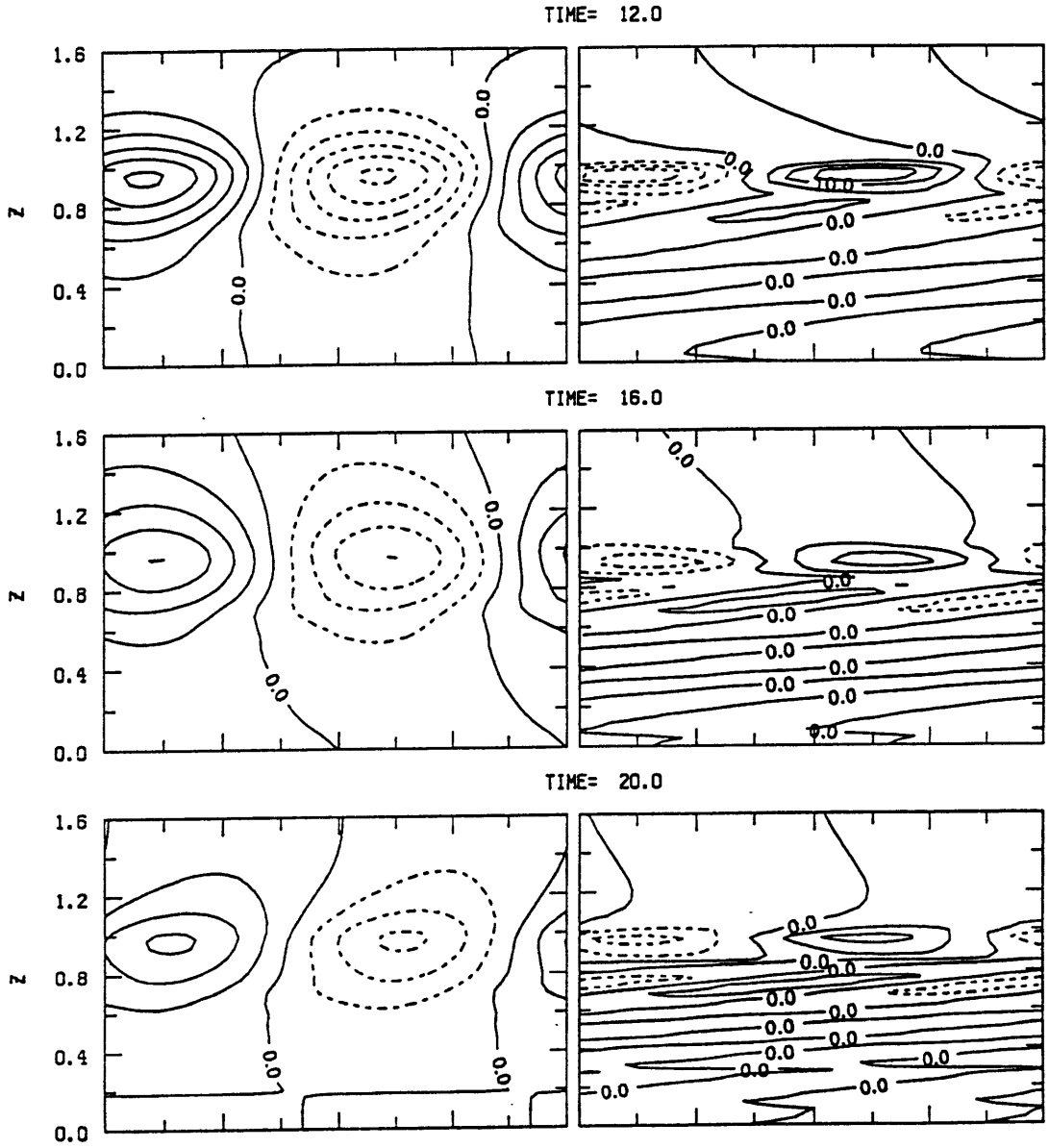
TIME= 12.0
TIME= 16.0
TIME= 20.0
Z
1.6
1.2
0.8
0.4
0.0
0.0

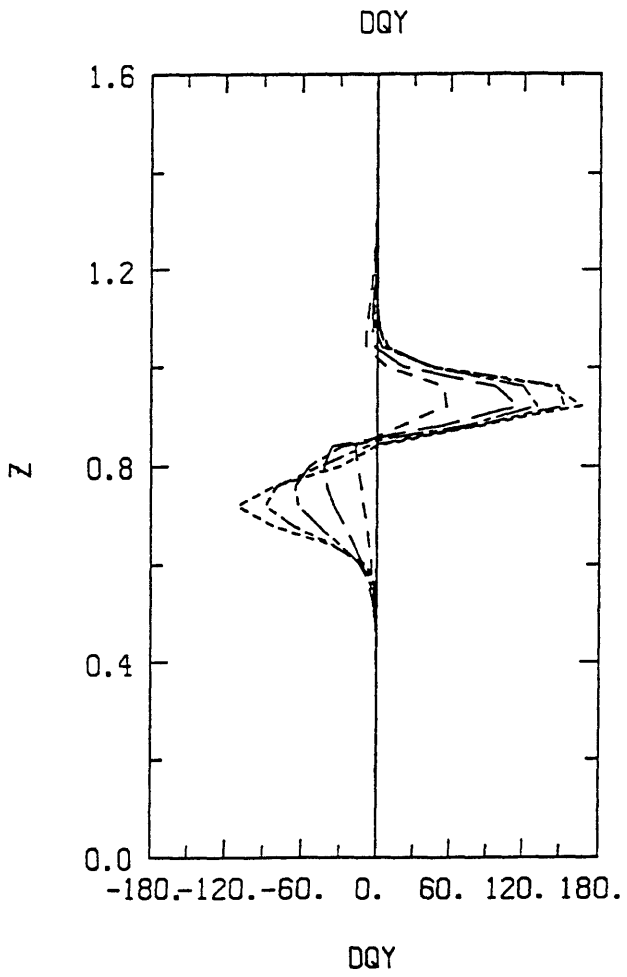

Figure 5.6: Time evolution of the vertical profiles of changes in the midchannel QPV gradient for the initial-value experiment with $k = 2.3$, $l = 1.4$, and $\beta = .5$.Time=4 (small dash line), 8 (long dash line), 12 (long dash - small dash line), 16 (long dash - small dash - small dash line), and 20 (very small dash line). The initial condition consists of the upper-level normal mode for the basic state with zero β. The initial streamfunction amplitude at the tropopause is fixed to unity.

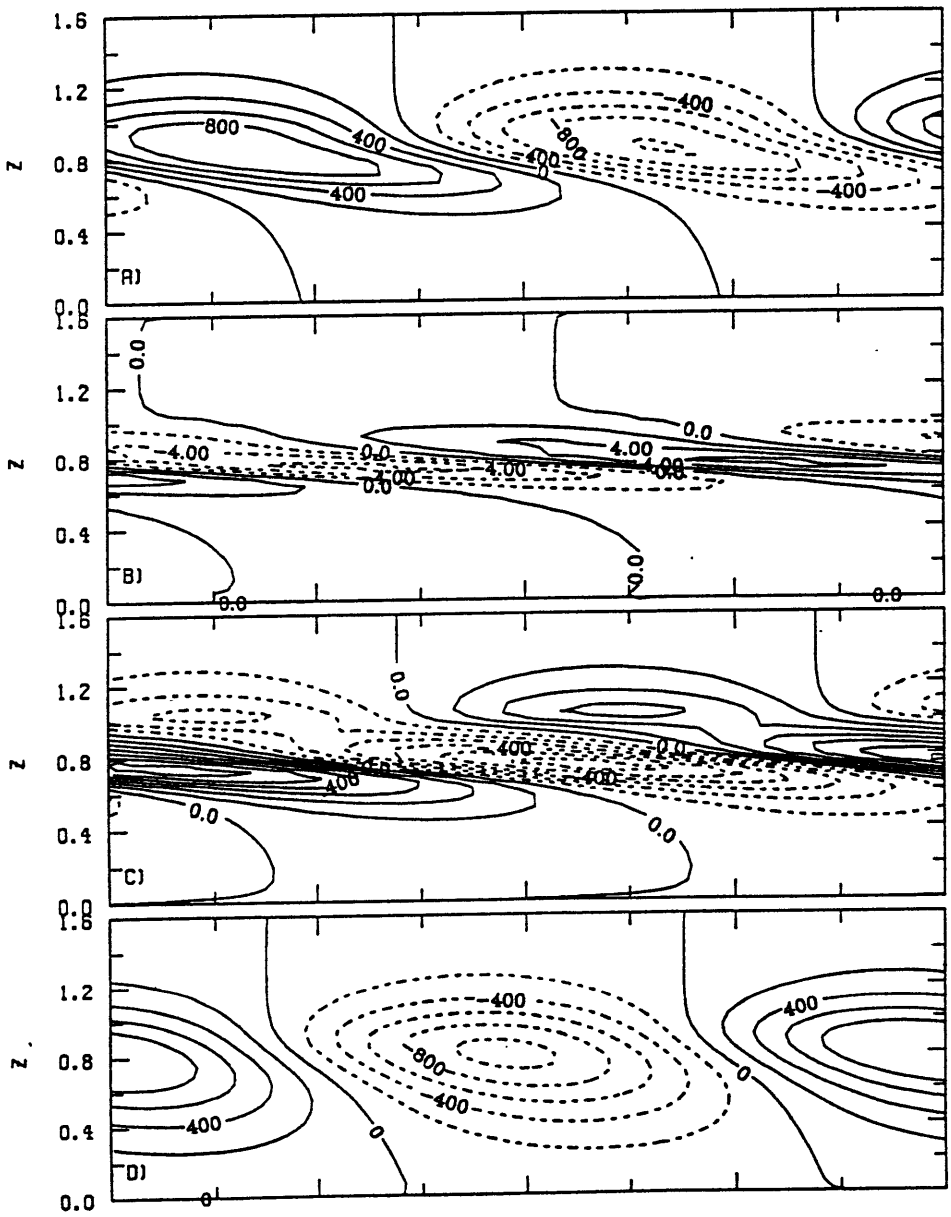

Figure 5.7: Midchannel $x - z$ cross section of the perturbation fields for the near optimal initial condition at $k = 2.3$, $l = 1.4$, and $\beta = 0.$, for $\epsilon = .15$. (a) Streamfunction, (b) QPV, (c) potential temperature, and (d) vertical velocity. The contour interval is .02 in (a), 2 in (b), .1 in (c) and .02 in (d). Negative values are dashed. A full zonal wavelength is represented.

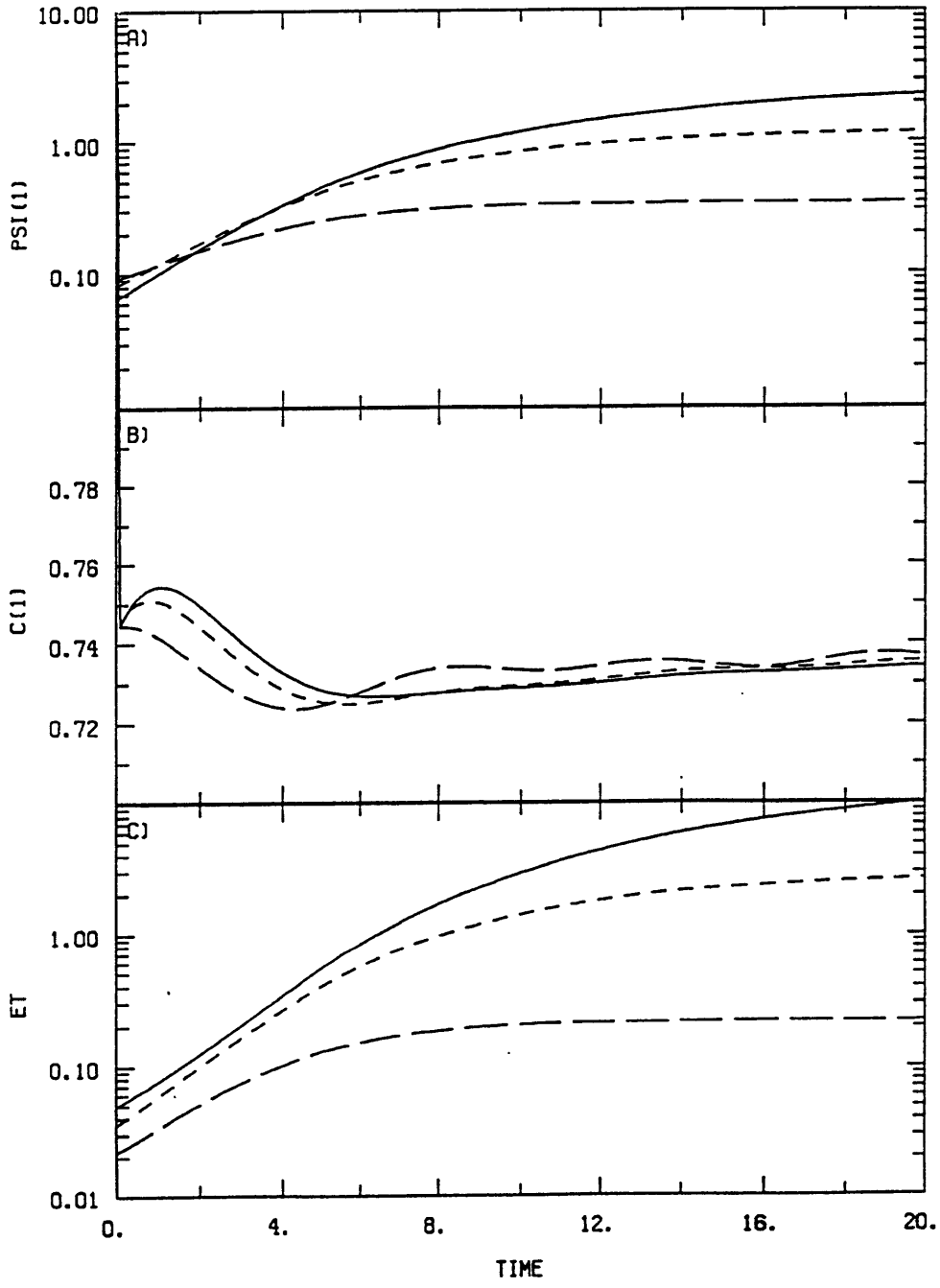

Figure 5.8: Time series of (a) $|\tilde{\psi}|^{z=1}$, (b) $c|^{z=1}$, and (c) E_T for initial-value experiments with $k = 2.3$, $l = 1.4$, $\beta = 0$, and variable ϵ. $\epsilon = .1$ (solid line), .15 (short dash line), and .3 (long dash line). The initial conditions consist of the near optimal disturbances for the basic state with zero β.

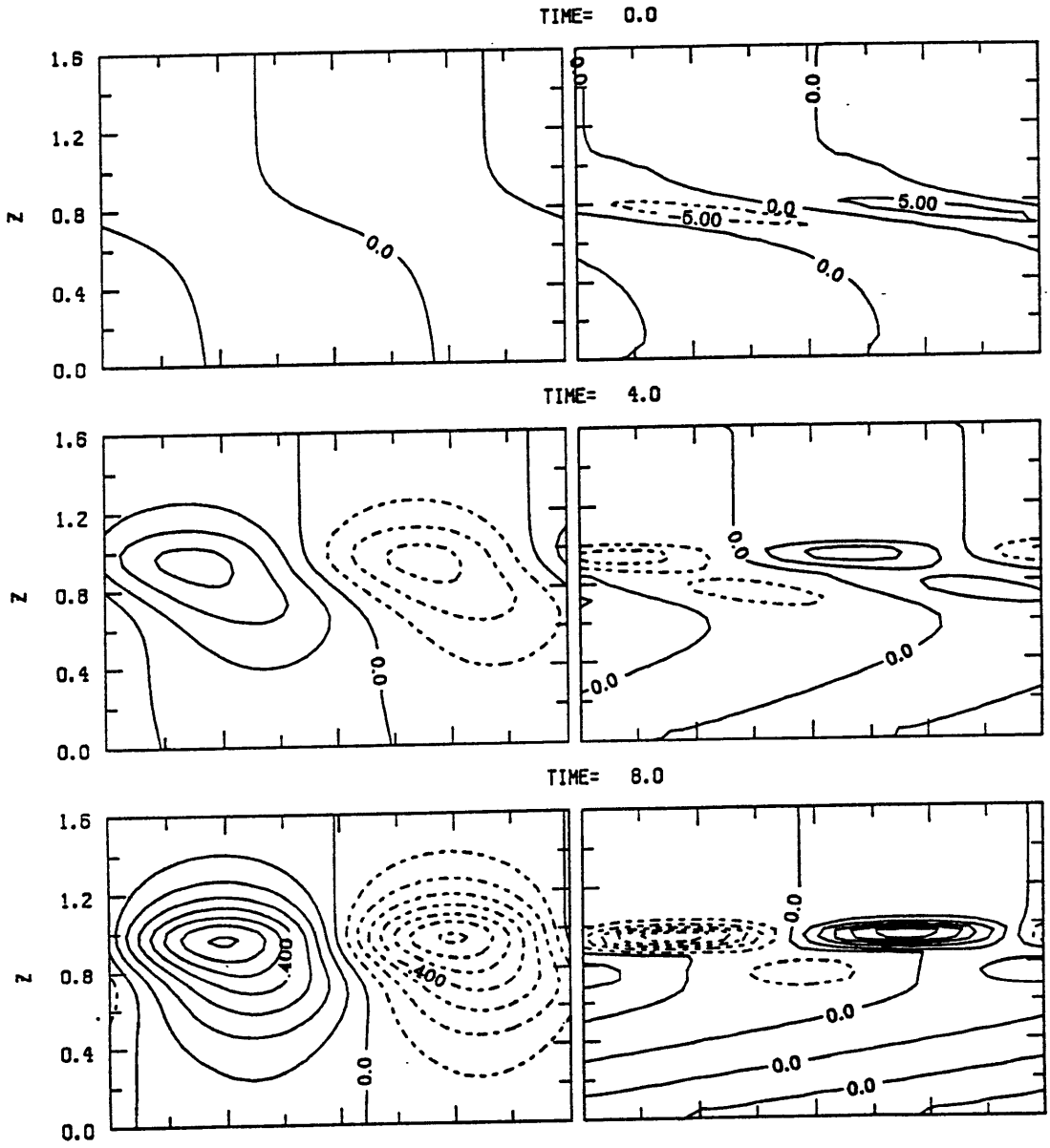

Figure 5.9: Time evolution of the midchannel perturbation streamfunction and QPV fields for the initial–value experiment with $k = 2.3$, $l = 1.4$, $\beta = 0.$, and $\epsilon = .15$. Time=0 (a), 4 (b), 8 (c), 12 (d), 16 (e), and 20 (f). The initial condition consists of the near optimal disturbance for the basic state with zero β. The contour interval is .1 for the streamfunction, and 5 for the QPV. Negative values are dashed. A full zonal wavelength is represented.

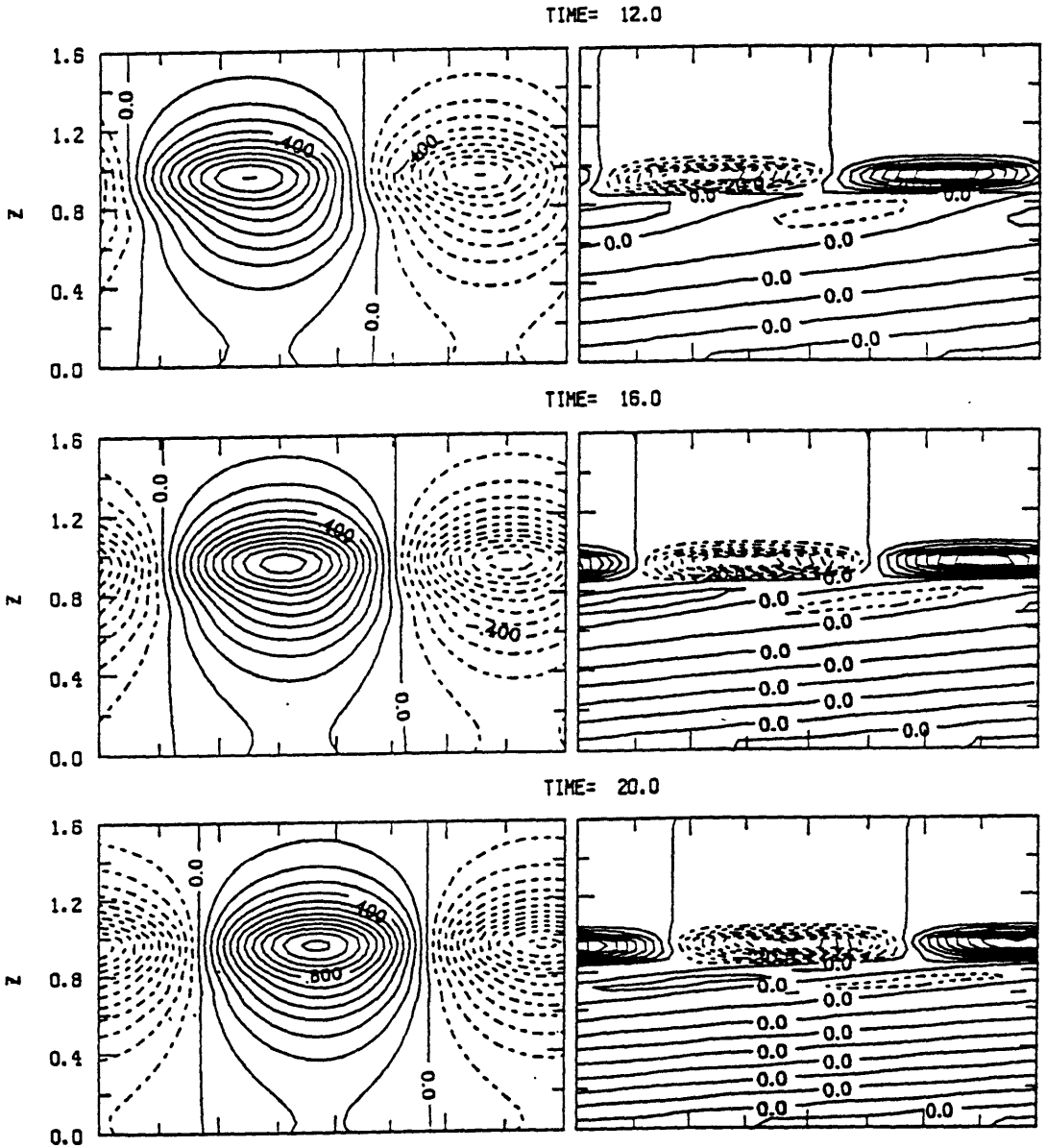
TIME= 12.0
TIME= 16.0
TIME= 20.0
Z
1.6
1.2
0.8
0.4
0.0
0.0
-.400
-.800

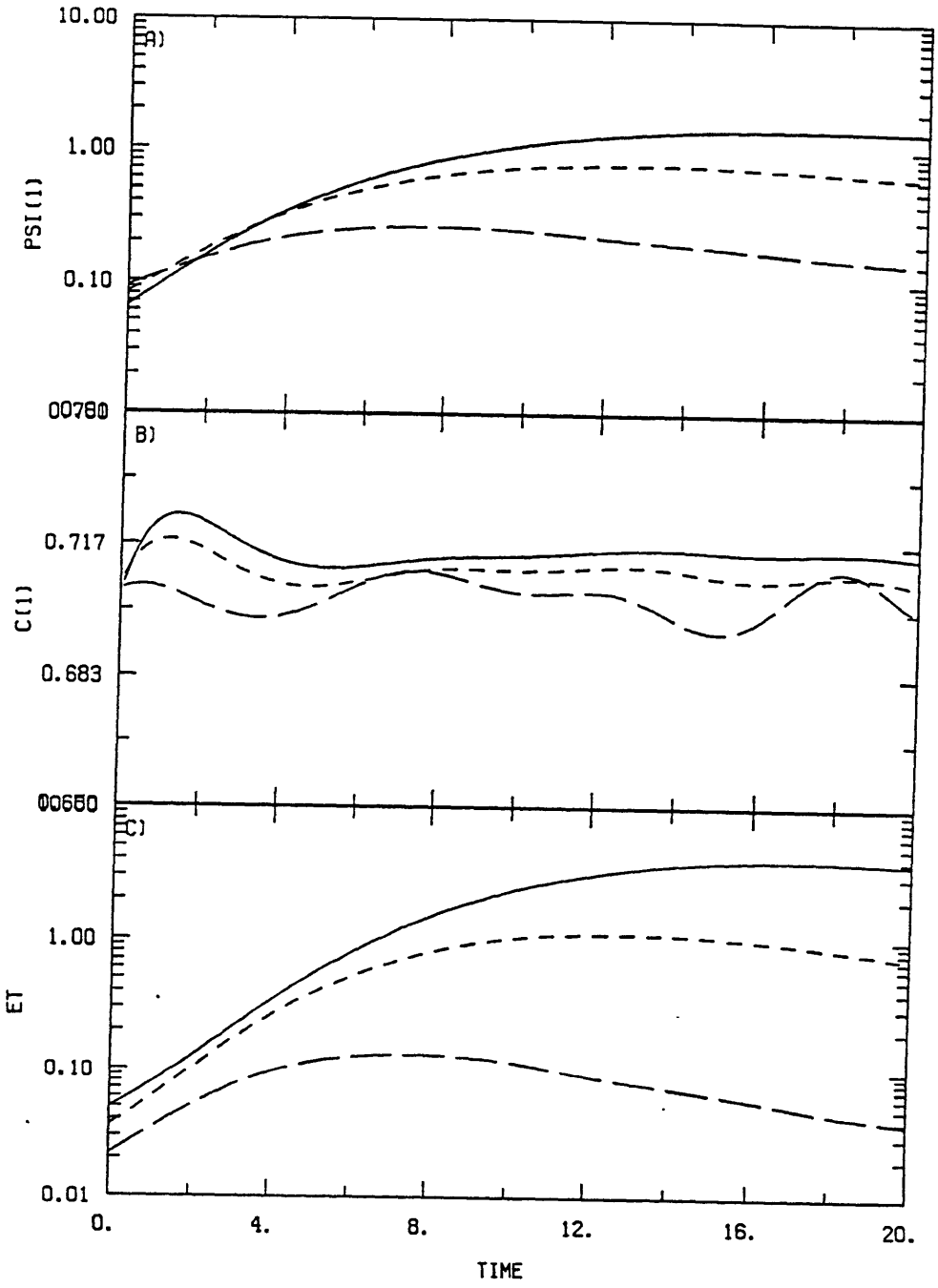

Figure 5.10: Time series of (a) $|\tilde{\psi}|^{z=1}$, (b) $c|^{z=1}$, and (c) E_T for initial–value experiments with $k = 2.3$, $l = 1.4$, $\beta = .5$, and variable ϵ. $\epsilon = .1$ (solid line), .15 (short dash line), and .3 (long dash line). The initial conditions consist of near optimal disturbances for the basic state with zero β.

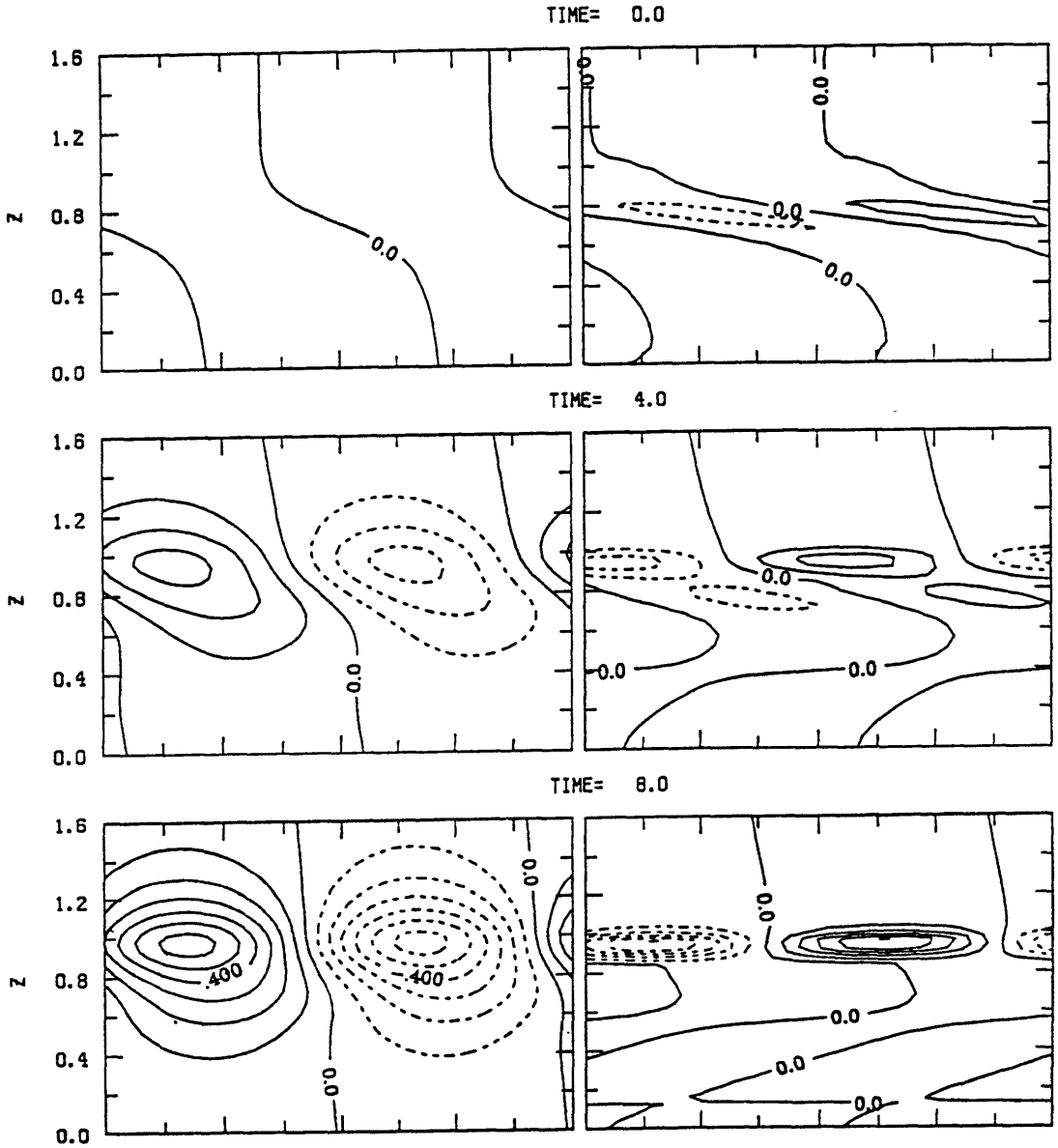

Figure 5.11: Time evolution of the midchannel perturbation streamfunction and QPV fields for the initial-value experiment with $k = 2.3$, $l = 1.4$, $\beta = .5$, and $\epsilon = .15$. Time=0 (a), 4 (b), 8 (c), 12 (d), 16 (e), and 20 (f). The initial condition consists of the near optimal disturbance for the basic state with zero β. The contour interval is .1 for the streamfunction, and 5 for the QPV. Negative values are dashed. A full zonal wavelength is represented.

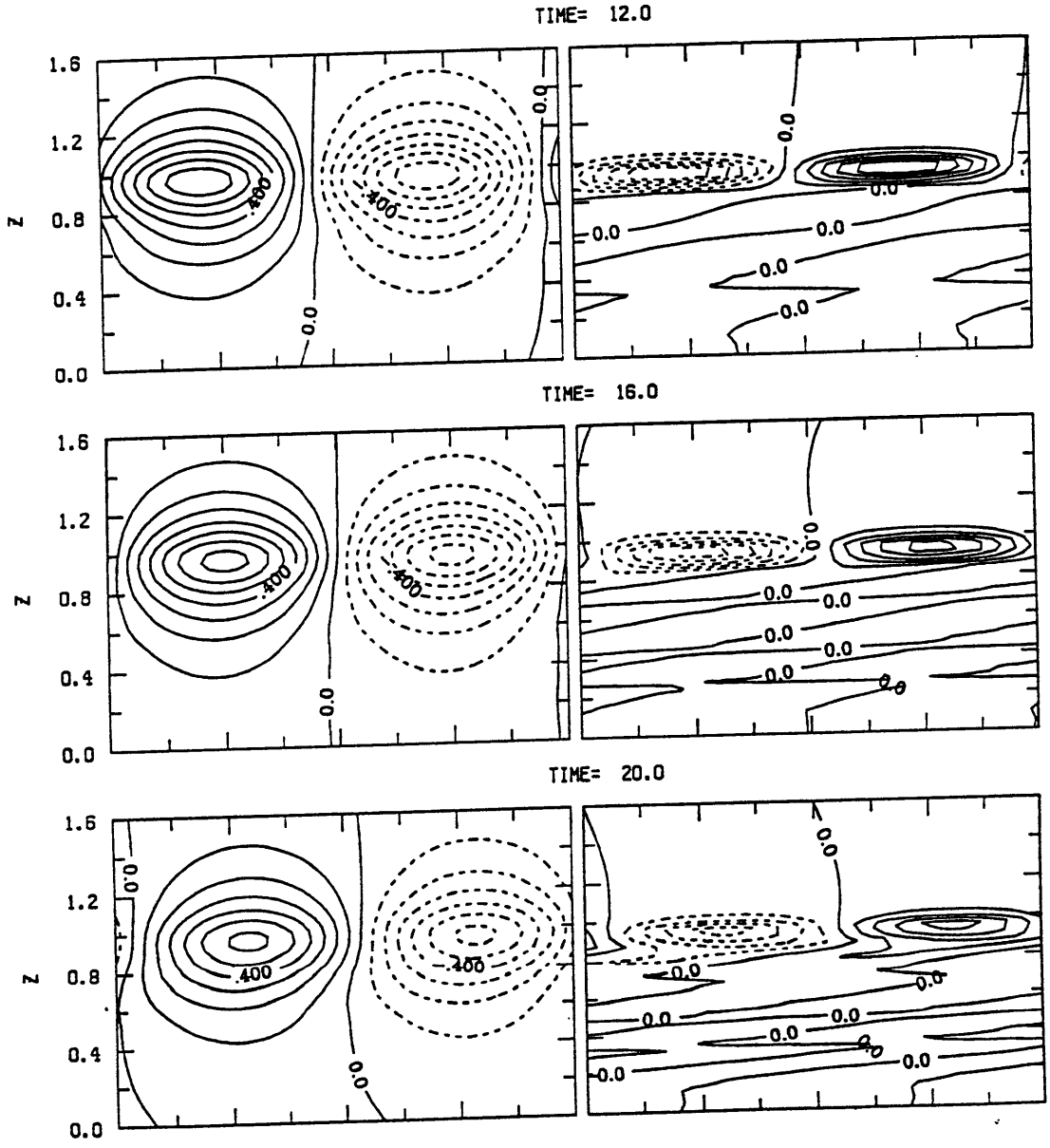
TIME= 12.0
TIME= 16.0
TIME= 20.0
Z
1.6
1.2
0.8
0.4
0.0
.400
0.0

Chapter 6

Conclusions

In this thesis we proposed simple dynamical models for the maintenance and excitation of midlatitude upper–level synoptic–scale waves. We developed an analytical model of waves on generalized Eady basic states with realistic tropopause and stratosphere. We showed that the Eady normal mode characteristics hold in the presence of these generalizations. In particular, the basic states support at the synoptic scale upper–level neutral normal modes, which are also nonlinear solutions of the governing equations. These modes share many characteristics with midlatitude upper–level synoptic–scale waves and provide a simple model for their dynamics, as waves supported by the large latitudinal gradient of potential vorticity at the tropopause in the jet region.

Moreover, we demonstrated that contrary to the general belief (Green, 1960), these modes have counterparts as slowly decaying quasi–modes in basic states with positive potential vorticity gradients. Mathematically the quasi–modes consist of a superposition of singular modes sharply peaked in the phase

speed domain; their decay proceeds as modes interfere with one another. With parameter values corresponding to a realistic upper bound for tropospheric potential vorticity gradients, upper–level waves are maintained for time scales consistent with observations.

We also studied the excitation of upper–level waves. Upper–tropospheric disturbances that lean against the shear were found to strongly excite upper–level waves even in the presence of tropospheric and stratospheric potential vorticity gradients, a circumstance precluding the existence of upper–level normal modes. This result is important mathematically because it demonstrates that quasi–modes are as likely to emerge from favorably configured initial conditions as real normal modes. We believe that more observational work is needed to assess the importance of this excitation mechanism for upper–level waves.

A limitation of this study is that we did not consider the effects of barotropic shear and of along–stream variations in the basic state flow. Thorncroft and Hoskins (1990) showed that the location of upper–level disturbances with respect to the barotropic shear is a factor determining their subsequent evolution. The importance of confluence and diffluence in the basic state flow has long been recognized as a factor in the development or decay of synoptic–scale perturbations (Bjerknes, 1954; Farrell, 1989). We believe that both the barotropic shear and the along–stream variations in the flow may influence the evolution of upper–level synoptic–scale waves, and propose inclusion of these effects in future studies of their dynamics.

Appendix A

The effect of friction at the lower boundary

We discuss in this appendix the evaluation of the boundary parameter η_l for the extratropical atmosphere [remember (2.20)]. To evaluate η_l a standard approach is to use an Ekman layer formulation:

$$\eta_l = \frac{N_0}{U_0}\sqrt{\frac{\nu}{2f_0}}, \tag{A.1}$$

where ν is the eddy viscosity of the air in the boundary layer (cf. Pedlosky, 1979, pp 338–340). From model simulations of boundary layers, Lin and Pierrehumbert (1988) found that appropriate values for ν range from 1 m^2/s for oceanic boundary layers to 5 and 20 m^2/s for flat and mountainous landmass boundary layers respectively. For these values of ν η_l varies from .03 and .06 to .12. In the atmosphere ν depends also on the stability profiles, with ν decreasing as the stability increases.

Another approach introduced by Emanuel (private communication) is to directly integrate the Reynolds equations from the top of the surface layer to that of the boundary layer (see Pedlosky, 1979, pp 170–174). After assuming

the presence of vertical shear forces only, and a balance between Coriolis, pressure gradient, and Reynolds stress forces, we get an expression for w' at the top of the boundary layer, $z' = z'_l$. Dimensionally,

$$w'_l = \frac{\vec{k}}{\rho_0 f_0} \cdot \left(\vec{\nabla}' \times \vec{\tau_s} \right),$$

where $\vec{\tau_s}$ is the total stress at the top of the surface layer, $\vec{\tau_s} = (\tau_s^x \vec{i} + \tau_s^y \vec{j})$, $\vec{\nabla}'$ is the gradient operator, $\vec{i}$, $\vec{j}$, and $\vec{k}$ the unit horizontal and vertical vectors, and where $\times$ represents the vector product. We then pose as an upper bound for $\vec{\tau_s}$,

$$\vec{\tau_s} = \rho_0 c_G U_s \left(\vec{U}' + \vec{u'} \right),$$

where U_s is a scale for the horizontal velocity at the top of the boundary layer, and c_G the geostrophic drag coefficient.

This yields an expression for the equivalent eddy viscosity, ν_E,

$$\nu_E = \frac{2 c_G^2 U_s^2}{f_0}, \tag{A.2}$$

and for w'_l,

$$w'_l = \frac{c_G U_0}{f_0} \nabla_H^2{}' (\Psi' + \psi').$$

After proper nondimensionalization we have:

$$\eta_l = \frac{c_G N_0 U_s}{f_0 U_0}. \tag{A.3}$$

From Garratt(1977) reasonable values for c_G are 10^{-3} for oceanic boundary layers, $2 \cdot 10^{-3}$ and $3 \cdot 10^{-3}$ for flat and mountainous landmass boundary layers. Using $U_s = 10\,\mathrm{m/s}$, the resulting values for η_l are then .04, .07 and .11, which correspond to equivalent eddy viscosities of 2,8, and $18\,\mathrm{m^2/s}$ from (A.2). The

two approaches give similar parameter ranges for the boundary layer parameter η_l. However, the evaluation of a realistic lower bound for the midlatitude boundary layer parameter still represents a matter of debate.

Appendix B

Approximate boundary conditions for semi–infinite domains

We consider in this thesis vertical domains of semi–infinite extent. For instance in chapter 4 the vertical domain consists of a semi–infinite troposphere bounded by a rigid lid, whereas in chapter 5 it consists of a semi–infinite atmosphere. We then need boundary conditions both at the upper and lower boundaries. We present here the development of boundary conditions at the upper boundary, and the conditions at the lower boundary follow easily.

Standard methods to deal with semi–infinite domains in a numerical model include setting the vertical velocity to zero at a large enough height, or introducing a sponge layer above the domain of interest. Both methods introduce a computational burden because of the added grid points, and the first method also creates spurious downward reflections. We present here exact radiation and boundedness conditions that apply in eigenvalue models. Furthermore, we show that exact conditions in initial–value models are Fourier transforms of conditions in eigenvalue models. We then develop approximate boundary

conditions for initial–value models. See for references Rasch (1986) and Béland and Warn (1975).

Eigenvalue models

Figure B.1 displays the geometry of the computational domain and of the dummy domain where basic state fields are assumed to be constant. In the dummy domain the quasi–geostrophic equation takes the form from (2.26):

$$\frac{d^2\hat{\psi}}{dz^2} - s_N \frac{d\hat{\psi}}{dz} - N_u^2 \left[K^2 + \frac{\beta}{U_u - c} \right] \hat{\psi} = 0, \text{ for } z > z_u.$$

A change of variable, $\hat{\psi} = \sqrt{N^2}\, e^{s_N z/2}\, \hat{\phi}$, yields:

$$\frac{d^2\hat{\phi}}{dz^2} - \left[\chi_u^2 \frac{c_{Ru} - c}{U_u - c} \right] \hat{\phi} = 0, \tag{B.1}$$

$$\text{where } c_{Ru} = U_u - \frac{\beta}{K^2 + s^2/(4N_u^2)}, \text{ and } \chi_u^2 = N_u^2 K^2 + s^2/4.$$

c_{Ru} represents the phase speed of free barotropic Rossby waves in the dummy domain. (B.1) implies that in the range $c < c_{Ru}$ or $c > U_u$, the solution is exponential–like, and in the range $c_{Ru} < c < U_u$ it is wavelike.

In the range $c < c_{Ru}$ or $c > U_u$, the proper boundary condition consists in keeping the bounded solution i.e. the exponential decaying with height. We then have as upper boundary condition:

$$\frac{d\hat{\phi}}{dz} + \mu_u \hat{\phi} = 0, \text{ or } \frac{d\hat{\psi}}{dz} - (s/2 - \mu_u)\, \hat{\psi} = 0, \tag{B.2}$$

$$\text{where } \mu_u^2 = \chi_u^2 \frac{c_{Ru} - c}{U_u - c}.$$

In the range $c_{Ru} < c < U_u$, the solution is wavelike and we keep the wave with energy that propagates outside the computational domain. From Pedlosky, 1979, p.433, the vertical group velocity, c_{gz}, obeys the following relation: $c_{gz} \alpha \overline{\hat{\phi}\hat{w}}$, where the overbar refers to an average over a zonal wavelength. After rewriting $\hat{\phi}$ as

$$\hat{\phi} = e^{imz} e^{i(kx-ct)},$$

we find that $c_{gz} \alpha m$, being positive for positive m. This implies that the proper radiation boundary condition is:

$$\frac{d\hat{\phi}}{dz} - im_u\hat{\phi} = 0, \text{ or } \frac{d\hat{\psi}}{dz} - (s/2 + im_u)\hat{\psi} = 0, \tag{B.3}$$

where $m_u^2 = -\mu_u^2$.

The suitable radiation and boundedness conditions at the lower boundary easily follow:

$$\frac{d\hat{\phi}}{dz} - \mu_l\hat{\phi} = 0, \text{ or } \frac{d\hat{\psi}}{dz} - (s/2 + \mu_l)\hat{\psi} = 0, \text{ for } c < c_{Rl} \text{ or } c > U_l, \tag{B.4}$$

$$\frac{d\hat{\phi}}{dz} + im_l\hat{\phi} = 0, \text{ or } \frac{d\hat{\psi}}{dz} - (s/2 - im_l)\hat{\psi} = 0, \text{ for } c_{Rl} < c < U_l, \tag{B.5}$$

$$\text{where } \mu_l^2 = \chi_l^2 \frac{c_{Rl} - c}{U_l - c},$$
$$m_l^2 = -\mu_l^2,$$

$$\chi_l^2 = N_l^2K^2 + s^2/4, \quad c_{Rl} = U_l - \frac{\beta}{K^2 + s^2/(4N_l^2)},$$

and U_l, N_l^2 are the values at the lower boundary. The boundary conditions (B.2), (B.3), (B.4), and (B.5) are easily implemented in eigenvalue models.

Initial–value models

In initial–value models we only look at approximate boundedness boundary conditions, because for the range of parameters explored in this thesis, the solution is mostly exponential–like at the boundaries. For example, let us calculate the range of c for wavelike solutions for typical parameter values: $k = 2.3$, $l = 1.4$, $\beta = 1$, $s = 0$, $U_u = 1$, and $U_l = 0$. Then at the lower and upper boundaries we have the following range of c for wavelike solutions, $c \epsilon [c_R, U]$: at $z = z_u$, $c \epsilon [.86, 1]$, and at $z = z_l$, $c \epsilon [-.14, 0]$. In initial–value simulations we usually have phase speeds in the range $c \epsilon [.3, .8]$, i.e. outside these propagating ranges.

The solution to the initial–value problem can be expressed in terms of $\tilde{\phi}(z,t)$ (remember section 2.1.2). Taking the Fourier transform in time, we rewrite $\tilde{\phi}(z,t)$ as

$$\tilde{\phi}(z,t) = (2\pi)^{-1/2} \int_{-\infty}^{\infty} dw\, \tilde{\phi}_w(z,w)\, e^{iwt}. \tag{B.6}$$

Replacing c by $-w/k$ in (B.2) yields a boundedness condition for $\tilde{\phi}_w$:

$$\frac{\partial \tilde{\phi}_w}{\partial z} + \chi_u \left[\frac{k c_{Ru} + w}{k U_u + w} \right]^{1/2} \tilde{\phi}_w = 0. \tag{B.7}$$

An exact boundedness condition for $\tilde{\phi}(z,t)$ can be obtained by taking the Fourier transform (B.6). However, this approach leads to an expression that involves a convolution in time, which is inconvenient because the values of the fields at previous times have to be stored. We prefer to find an approximate form for (B.7) that leads to a condition for $\tilde{\phi}(z,t)$ not involving a convolution in time.

Let us make the following approximation in (B.7):

$$\left[\frac{kc_{Ru}+w}{kU_u+w}\right]^{1/2} = \left[1-\frac{U_u-c_{Ru}}{U_u+w/k}\right]^{1/2} \cong 1-\frac{U_u-c_{Ru}}{2(U_u+w/k)}.$$

This approximation is good when $|U_u - c_{Ru}| \ll |U_u - c|$. (B.7) then becomes:

$$\frac{\partial\tilde{\phi}_w}{\partial z}+\mu_u^a\tilde{\phi}_w=0, \tag{B.8}$$

$$\text{where } \mu_a=\chi_u\left(1-\frac{U_u-c_{Ru}}{2(U_u+w/k)}\right).$$

After taking the Fourier transform (B.6), we get this expression for $\tilde{\phi}(z,t)$ at $z=z_u$:

$$\frac{\partial}{\partial t}\left(\frac{\partial\tilde{\phi}}{\partial z}+\chi_u\tilde{\phi}\right)=-ikU_u\left(\frac{\partial\tilde{\phi}}{\partial z}+\chi_u\tilde{\phi}\right)+\frac{ik\beta N_u^2}{2\chi_u}\tilde{\phi}; \tag{B.9}$$

and for $\tilde{\psi}(z,t)$:

$$\frac{\partial}{\partial t}\left[\frac{\partial\tilde{\psi}}{\partial z}-(s/2-\chi_u)\tilde{\psi}\right]=-ikU_u\left[\frac{\partial\tilde{\psi}}{\partial z}-(s/2-\chi_u)\tilde{\psi}\right]+\frac{ik\beta N_u^2}{2\chi_u}\tilde{\psi}. \tag{B.10}$$

These represent approximate boundedness boundary conditions for the transient problem.

Following a similar procedure, we get the approximate boundary conditions at the lower boundary, $z=z_l$:

$$\frac{\partial}{\partial t}\left(\frac{\partial\tilde{\phi}}{\partial z}-\chi_l\tilde{\phi}\right)=-ikU_l\left(\frac{\partial\tilde{\phi}}{\partial z}-\chi_l\tilde{\phi}\right)-\frac{ik\beta N_l^2}{2\chi_l}\tilde{\phi}, \tag{B.11}$$

$$\frac{\partial}{\partial t}\left[\frac{\partial\tilde{\psi}}{\partial z}-(s/2+\chi_l)\tilde{\psi}\right]=-ikU_l\left[\frac{\partial\tilde{\psi}}{\partial z}-(s/2-\chi_l)\tilde{\psi}\right]-\frac{ik\beta N_l^2}{2\chi_l}\tilde{\psi}. \tag{B.12}$$

It is interesting to look at the properties of these approximate boundary conditions, and compare them with the properties of rigid boundary conditions. To do so we assume constant N^2 and U in the computational domain

as well. In the range of wave solution we compute a reflection coefficient r, which is the ratio of the outgoing to the incoming wave streamfunction, and in the range of exponential solution a transmission coefficient c_t, which is the ratio of the unbounded to the bounded solution.

Let us first calculate c_t and r for the approximate boundary condition at the upper lid. From (B.8) the solution in the dummy domain can be expressed as

$$\hat{\psi} = A_D e^{sz/2} e^{-\mu_u^a z}.$$

For exponential–like solution ($c < c_{Ru}$ or $c > U_u$) the solution in the computational domain is from (B.2):

$$\hat{\psi} = A_C e^{sz/2} \left[e^{-\mu_u z} + c_t e^{\mu_u z} \right].$$

The two solutions are matched by equating the impedance at $z = z_u$ (Gill, 1982, p.147), which leads to the following expression for c_t:

$$c_t = \frac{\mu_u - \mu_u^a}{\mu_u + \mu_u^a}. \tag{B.13}$$

In the case of the exact boundedness conditions μ_u^a is simply μ_u and c_t is zero. For wavelike solution ($c_{Ru} < c < U_u$), the solution in the dummy domain is from (B.3)

$$\hat{\psi} = A_C e^{sz/2} \left[e^{im_u z} + r e^{-im_u z} \right]. \tag{B.14}$$

Matching solutions at $z = z_u$ leads to the following expression for r,

$$r = \frac{-\mu_u^a + im_u}{\mu_u^a - im_u}. \tag{B.15}$$

The coefficients c_t and r of the approximate conditions at the lower boundaries have the same parameter dependencies as those at the upper lid, except that μ_l^a, μ_l, and m_l replace μ_u^a, μ_u, and m_u in (B.13) and (B.15).

In the case of the rigid boundary condition, $r = 1$ at both the lower and upper boundaries in the range of wavelike solution. In the range of exponential behavior at the lower boundary,

$$c_t = \frac{\mu_l + s/2}{\mu_l - s/2}, \tag{B.16}$$

and at the upper boundary,

$$c_t = \frac{\mu_l - s/2}{\mu_l + s/2}. \tag{B.17}$$

Figure B.2 displays the logarithm of the magnitude of c_t and r for approximate boundary conditions at the upper and lower boundaries for typical parameter values. In the propagating ranges the magnitude of r is unity as can be seen in (B.15). Notice the sharp decrease in the magnitude of c_t around the propagating range. For the same parameter values as in figure B.2, the magnitude of r and c_t for the rigid condition at both boundaries is simply unity since $s = 0$ [remember (B.16) and (B.17)]. The approximate boundary conditions represent a definite advantage over the rigid conditions outside the propagating ranges. For example, at $k = 2.3$ and $c = .6$,which are typical values for upper–level waves, $c_t \cong 10^{-3}$ at the lower boundary, and $c_t \cong 10^{-2}$ at the upper boundary. Using approximate boundary conditions allows us to consider vertical domains of smaller vertical extent than would be possible using rigid boundary conditions.

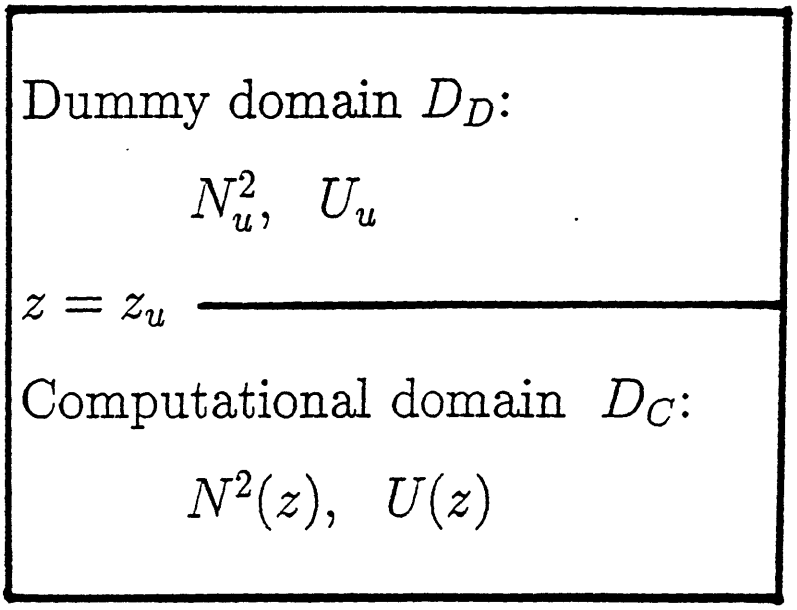

Figure B.1: Geometry of the dummy domain (D_D) and the computational domain (D_C) at the upper boundary.

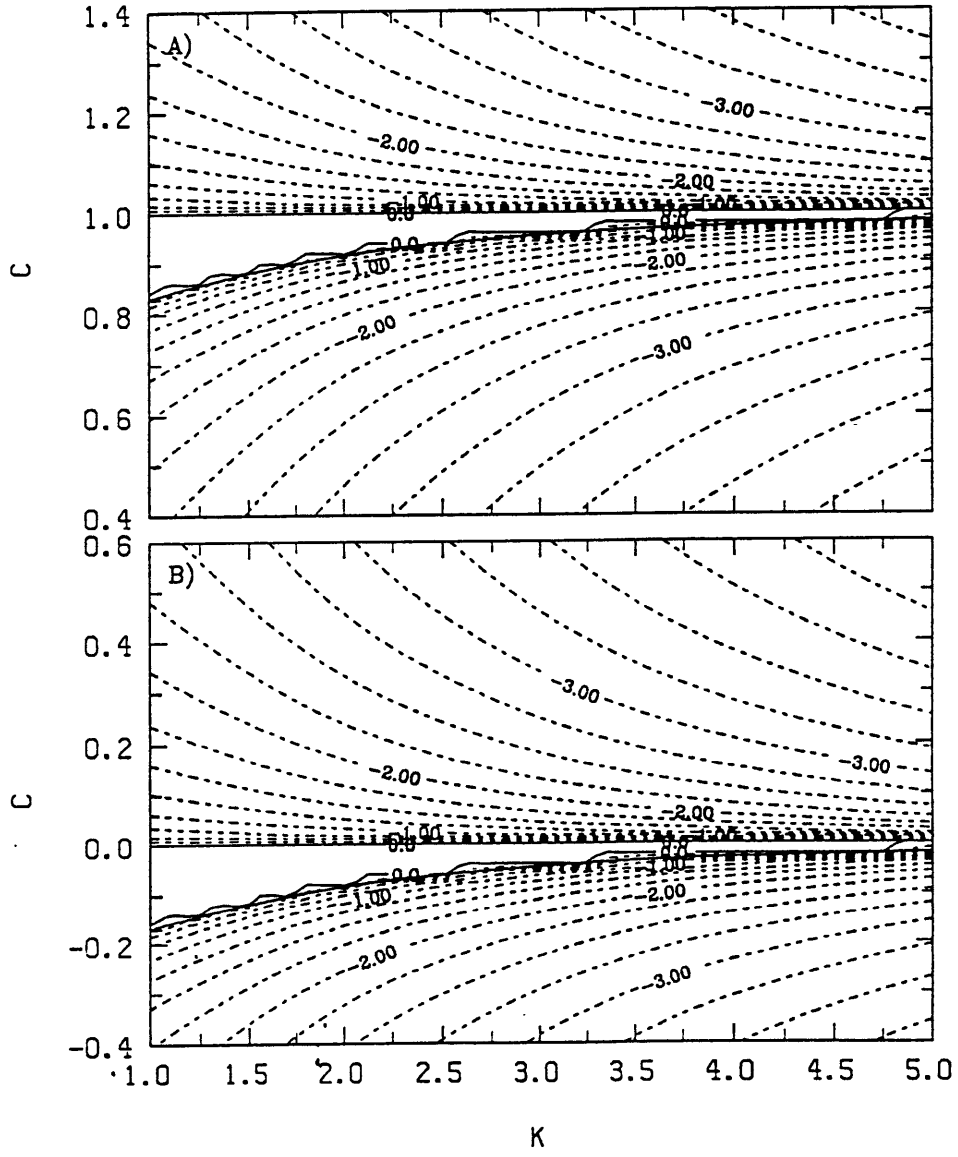

Figure B.2: Logarithm of the magnitude of the reflection coefficient, r, and of the transmission coefficient, c_t, of approximate boundedness boundary conditions as a function of the zonal wavenumber, k, and the phase speed, c; (a) at the upper lid, and (b) at the lower lid. ($s = 0$, $\beta = .5$, $l = 1.4$, $U_u = 1$, $N_u^2 = 4$, $U_l = 0$, and $N_l^2 = 1$).

Appendix C

A fourth–order vertical discretization

In this appendix we present a fourth–order discretization of the following set of equations and boundary conditions:

$$\begin{aligned} \frac{d^2\phi}{dz^2} + L(z)\phi &= R(z), \\ \frac{d\phi}{dz} + L_l\phi &= R_l, \text{ at } z = z_l, \\ \frac{d\phi}{dz} + L_u\phi &= R_u, \text{ at } z = z_u. \end{aligned} \tag{C.1}$$

It is possible to derive a fourth–order scheme with a near Galerkin method (cf. Staniforth and Mitchell, 1977). Let us define the Chapeau functions,

$$\begin{aligned} e^k(z) &= \frac{z - z_{k-1}}{\triangle z} \text{ for } z_{k-1} < z < z_k, \\ &= \frac{z_{k+1} - z}{\triangle z} \text{ for } z_k < z < z_{k+1}, \end{aligned}$$

where $0 < k < N$, and $\triangle z = \frac{z_u - z_l}{N-1}$. Multiplying (C.1) by $e^k(z)$ and integrating over the domain yields:

$$\int_{z_l}^{z_u} dz \left[e^k R - e^k L\phi + e^k_z \frac{d\phi}{dz} \right] - \delta_{kN} \left(R_u - L_u\phi \right) + \delta_{k1} \left(R_l - L_l\phi \right) = 0.$$

Following a strict Galerkin method involves expanding ϕ in terms of Chapeau functions, and it would lead to a second–order scheme. The approach taken here is to use second–order polynomials for the quadrature of integrals, and this gives rise to a fourth–order scheme.

In the interior the scheme is:

$$\begin{aligned}\frac{1}{12}\left(R_{k-1}+10R_k+R_{k+1}\right) \;=\; & \\ & \phi_{k-1}\left[\frac{1}{\triangle z^2}+\frac{7}{120}L_{k-1}+\frac{L_k}{20}-\frac{L_{k+1}}{40}\right]+ \\ & \phi_k\;\left[\frac{-2}{\triangle z^2}+\frac{L_{k-1}}{20}+\frac{11}{15}L_k-\frac{L_{k+1}}{20}\right]+ \\ & \phi_{k+1}\left[\frac{1}{\triangle z^2}-\frac{L_{k-1}}{40}+\frac{L_k}{20}+\frac{7}{120}L_{k+1}\right].\end{aligned}$$

At the lower boundary:

$$\begin{aligned}\left(\frac{7}{24}R_1+\frac{R_2}{4}-\frac{R_3}{24}\right)\triangle z \;+\; R_l = & \\ & \phi_1\left[\left(\frac{49}{240}L_1+\frac{13}{120}L_2-\frac{L_3}{48}\right)\triangle z-\frac{1}{\triangle z}+L_l\right]+ \\ & \phi_2\left[\left(\frac{13}{120}L_1+\frac{L_2}{6}-\frac{L_3}{40}\right)\triangle z+\frac{1}{\triangle z}\right]+ \\ & \phi_3\left[\left(\frac{-L_1}{48}-\frac{L_2}{40}-\frac{L_3}{240}\right)\triangle z\right].\end{aligned}$$

At the upper boundary:

$$\begin{aligned}\left(\frac{-7}{24}R_N-\frac{R_{N-1}}{4} \;+\; \frac{R_{N-2}}{24}\right)\triangle z+R_u = & \\ & \phi_{N-2}\left[\left(\frac{L_N}{48}+\frac{L_{N-1}}{40}-\frac{L_{N-2}}{240}\right)\triangle z\right]+ \\ & \phi_{N-1}\left[\left(\frac{-13}{120}L_N-\frac{L_{N-1}}{6}+\frac{L_{N-2}}{40}\right)\triangle z-\frac{1}{\triangle z}\right]+ \\ & \phi_N\;\left[\left(\frac{-49}{240}L_N-\frac{13}{120}L_{N-1}+\frac{L_{N-2}}{48}\right)\triangle z+\frac{1}{\triangle z}+L_u\right].\end{aligned}$$

With this scheme the discretized problem can be expressed as a matrix equation,

$$[L]|\phi>=|R>,$$

where $[L]$ is an $N \times N$ matrix, $|\phi>$ the vector at the truncation N, and $|R>$ the right–hand side. The advantage of this discretization is that it reaches fourth–order accuracy with only a tridiagonal matrix.

References

Béland, M. and T.Warn, 1975: The radiation condition for transient Rossby waves. *J. Atmos. Sci.*, **32**, 1873–1880.

Bjerknes, J., 1937: Theorie der aussertropischen Zyklonenbildung. *Meteorol. Z.*, **54**, 462–466.

Bjerknes, J. and J.Holmboe, 1944: On the theory of cyclones. *J.Meteorol.*, **1**, 1–22.

Bjerknes, J., 1954: The diffluent upper trough. *Meteor., Geophys., Bio.*, **A7**, 41–46.

Bleck, R. and C.Mattocks, 1984: A preliminary analysis of the role of potential vorticity in Alpine lee cyclogenesis. *Beitr. Phys. Atmos.*, **57**, 357–368.

Bretherton, F.P., 1966: Critical layer instability in baroclinic flows. *Quart. J. Roy. Meteor. Soc.*, **92**, 325–334.

Brunt, D., 1930: Some problems of modern meteorology:I. The present position of theories on the origin of cyclonic depressions. *Quart. J. Roy. Meteor. Soc.*, **56**, 345–350.

Case, K.M., 1960: Stability of inviscid plane Couette flow. *Phys. Fluids*, bf 3, 143–148.

Charney, J.G., 1947: The dynamics of long waves in a baroclinic westerly current. *J.Meteor.*, **4**, 135–162.

Charney, J.G. and M.E.Stern, 1962: On the stability of internal baroclinic jets

in a rotating atmosphere. *J. Atmos. Sci.*, **19**, 159–172.

Charney, J.G., 1973: Planetary fluid dynamics. in "Dynamic Meteorology" edited by P.Morel. D.Reidel, Boston, 97–352.

Cohen-Tannoudji, C., B.Diu, and F.Laloe, 1977: "Mécanique quantique Tome 1". Hermann, Paris, 891pp.

Davis, C.A., 1990: Cyclogenesis diagnosed with potential vorticity. Ph.D. Thesis, Center for Meteorology and Physical Oceanography, MIT, Cambridge, MA. 194pp.

Drazin, P.G. and W.H.Reid, 1981: "Hydrodynamic stability". Cambridge University Press, Cambridge, 527 pp.

Eady, E.T., 1949: Long waves and cyclone waves. *Tellus*, **1**, 33–52.

Emanuel, K.A., M.Fantini, and A.J.Thorpe, 1987: Baroclinic instability in an environment of small stability to slantwise moist convection. Part I: Two-dimensional models. *J. Atmos. Sci.*, **44**, 1559–1573.

Farrell, B., 1982: The initial growth of disturbances in a baroclinic flow. *J. Atmos. Sci.*, **39**, 1663–1686.

Farrell, B., 1984: Modal and non-modal baroclinic waves. *J. Atmos. Sci.*, **41**, 668–673.

Farrell, B., 1985: Transient growth of damped baroclinic waves. *J. Atmos. Sci.*, **42**, 2718–2727.

Farrell, B., 1989: On the optimal excitation of baroclinic waves. *J. Atmos. Sci.*, **46**, 668–673.

Farrell, B.F., 1989: Transient development in confluent and diffluent flow. *J. Atmos. Sci.*, **46**, 3279–3288.

Fullmer, J.W.A., 1982a: Calculations of the quasi-geostrophic potential vorticity gradient from clima al data. *J. Atmos. Sci.*, **39**, 1873–1877.

Fullmer, J.W.A., 1982b: The baroclinic instability of highly structured one-

dimensional basic states. *J. Atmos. Sci.*, **39**, 2371–2387.

Garratt, J.R., 1977: Review of drag coefficients over oceans and continents. *Mon. Wea. Rev.*, **105**, 915–929.

Gill, A.E., 1982: "Atmosphere-Ocean Dynamics". Academic Press, New York, 662pp.

Green, J.S.A., 1960: A problem in baroclinic stability. *Quart. J. Roy. Meteor. Soc.*, **86**, 237–251.

Haltiner, G.J. and R.T.Williams, 1980: "Numerical Prediction and Dynamic Meteorology". John Wiley & Sons, New York, 477pp.

Held, I.M., 1985: Pseudomomentum and the orthogonality of modes in shear flows. *J. Atmos. Sci.*, **42**, 2280–2288.

Held, I.M., R.L.Panetta, and R.T.Pierrehumbert, 1985: Stationary Rossby waves in vertical shear. *J. Atmos. Sci.*, bf 42, 865–883.

Hoskins, B.J., M.E.McIntyre, and A.W.Robertson, 1985: On the use and significance of isentropic potential vorticity maps. *Quart. J. Roy. Meteor. Soc.*, **111**, 877–946.

Ince, E.L., 1926: "Ordinary differential equations". reprinted 1956 by Dover, New York, 558pp.

Ioannou, P. and R.S.Lindzen, 1986: Baroclinic instability in the presence of barotropic jets. *J. Atmos. Sci.*, **43**, 2999–3014.

Kuo, H.L., 1979: Baroclinic instability of linear and jet profiles in the atmosphere. *J. Atmos. Sci.*, **36**, 2360–2378.

Lin, S.J. and R.T.Pierrehumbert, 1988: Does Ekman friction suppress baroclinic instability? *J. Atmos. Sci.*, **45**, 2920–2933.

Lindzen, R.S., B.Farrell, and D.Jacqmin, 1982: Vacillation due to wave interference: applications to the atmosphere and to the annulus experiments. *J. Atmos. Sci.*, **39**, 14–23.

Maslowe, S.A., 1981: Shear flow instabilities and transition. In "Hydrodynamic Instabilities and the Transition to Turbulence", ed. H.L.Swinney, J.P.Gollub. Springer–Verlag, Berlin, pp. 181-228.

Montgomery, M.T. and B.F.Farrell, 1990: Surface cyclogenesis as an initial value problem. Accepted for publication in *J. Atmos. Sci.*.

Neilley, P.P., 1990: Interactions between synoptic–scale eddies and the large–scale flow during the life cycles of persistent flow anomalies. Ph.D. Thesis, Center for Meteorology and Physical Oceanography, MIT, Cambridge, MA. 272pp.

Palmen, E. and C.W.Newton, 1969: "Atmospheric circulation systems". Academic Press, New York, 603pp.

Pedlosky, J., 1964: An initial value problem in the theory of baroclinic instability. *Tellus*, **16**, 12–17.

Pedlosky, J., 1979: "Geophysical fluid dynamics". Springer-Verlag, New York, 624pp.

Peterssen, S., 1956: "Weather Analysis and Forecasting. Vol. 1, Motion and Motion Systems". McGraw Hill, New York, 428pp.

Peterssen, S. and S.J.Smebye, 1971: On the development of extratropical cyclones. *Quart. J. Roy. Meteor. Soc.*, **97**, 457–482.

Rasch, P.J., 1986: Toward atmospheres without tops: Absorbing upper boundary conditions for numerical models. *Quart. J. Roy. Meteor. Soc.*, **112**, 1195–1218.

Rossby, C.G., 1939: Relation between variations in the intensity of zonal circulation of the atmosphere and the displacements of the semi- permanent centers of action. *J. Marine Research*, **2**, 38–55.

Rotunno, R. and M.Fantini, 1989: Peterssen's type B cyclogenesis in terms of discrete, neutral Eady modes. *J. Atmos. Sci.*, **46**, 3599–3604.

Sanders, F., 1988: Life history of mobile troughs in the upper westerlies. *Mon. Wea. Rev.*, **118**, 2629–2648.

Simmons, A.J. and B.J.Hoskins, 1976: Baroclinic instability on the sphere: Normal modes of the primitive and quasi-geostrophic equations. *J. Atmos. Sci.*, **33**, 1454–1477.

Simmons, A.J. and B.J.Hoskins, 1977: Baroclinic instability on the sphere: Solutions with a more realistic tropopause. *J. Atmos. Sci.*, **34**, 581–588.

Simmons, A.J. and B.J.Hoskins, 1978: The life cycles of some nonlinear baroclinic waves. *J. Atmos. Sci.*, **35**, 414–432.

Snyder, C. and R.S.Lindzen, 1988: Upper level baroclinic instability. *J. Atmos. Sci.*, **45**, 2445–2459.

Staniforth, A.N. and H.L. Mitchell, 1977: A semi-implicit finite-element barotropic model. *Mon. Wea. Rev.*, **105**, 154–169.

Thorncroft, C.D. and B.J.Hoskins, 1990: Frontal cyclogenesis. Submitted for publication.

Tung, K.K., 1983: Initial–value problems for Rossby waves in a shear flow with critical level. *J. Fluid Mech.*, **133**, 443–469.

Uccellini, L.W., D.Keyser, K.F.Brill, and C.H.Wash, 1985: The Presidents' Day cyclone of 18–19 February 1979: Influence of upstream tropopause folding on rapid cyclogenesis. *Mon. Wea. Rev.*, **113**, 962–980.

Valdes, P.J. and B.J.Hoskins, 1988: Baroclinic instability of the zonally averaged flow with boundary layer damping. *J. Atmos. Sci.*, **45**, 1584–1593.

Whitaker, J.S. and A.Barcilon, 1989: Genesis of mobile troughs in the upper Westerlies. Submitted for publication.

Williams, G.P., 1974 : Generalized Eady waves. *J. Fluid Mech.*, **62**, 643–655.

Williams, G.P. and J.B.Robinson, 1974: Generalized Eady waves with Ekman pumping. *J. Atmos. Sci.*, **31**, 1768–1776.

Young, J.A., 1968: Comparative properties of some time differencing schemes for linear and nonlinear oscillations. *Mon. Wea. Rev.*, **96**, 357-364.